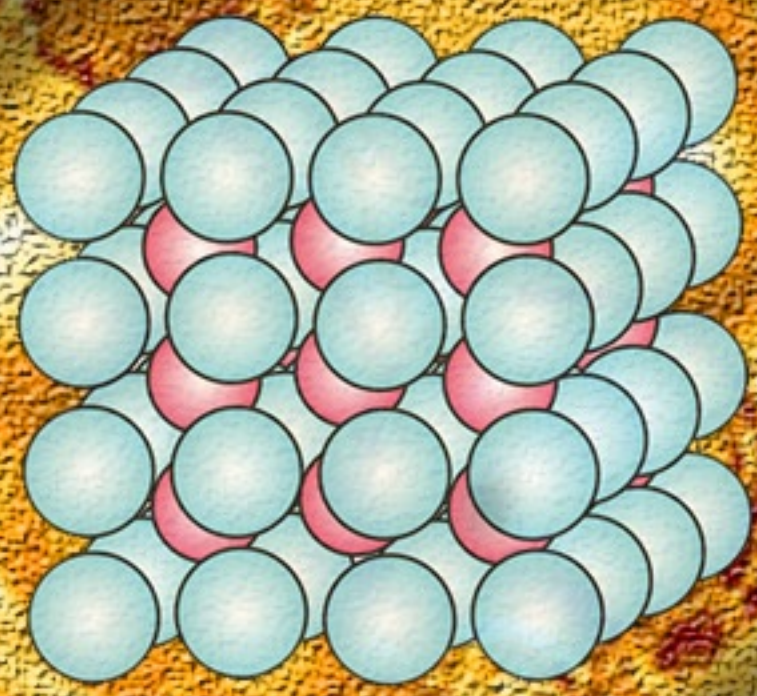
INTERNATIONAL SCIENTIFIC JOURNAL

"MATERIAL SCIENCE"



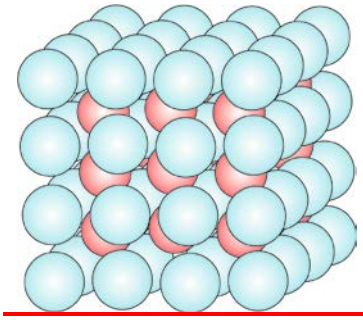
„NONEQUILIBRIUM PHASE TRANSFORMATIONS"

YEAR IV, ISSUE 2/2018

ISSN PRINT 2367-749X
ISSN WEB 2534-8477

PUBLISHER: SCIENTICIC TECHNICAL UNION OF MECHANICAL ENGINEERING INDUSTRY 4.0

108 Rakovski str., 1000 Sofia, Bulgaria
tel./fax (+359 2) 986 22 40, tel. (+359 2) 987 72 90,
office@stumejournals.com, www.stumejournals.com



INTERNATIONAL SCIENTIFIC JOURNAL

MATERIALS SCIENCE. NON-EQUILIBRIUM PHASE TRANSFORMATIONS

PUBLISHER:

SCIENTIFIC TECHNICAL UNION OF MECHANICAL ENGINEERING "INDUSTRY 4.0"

108, Rakovski Str., 1000 Sofia, Bulgaria
tel. (+359 2) 987 72 90,
tel./fax (+359 2) 986 22 40,
office@stumejournals.com

ISSN PRINT 2367-749X, ISSN WEB 2534-8477
YEAR IV, ISSUE 2/ 2018

EDITORIAL BOARD

CHIEF EDITOR

Prof. Dimitar Stavrev – Bulgaria

DEPUTY EDITOR:

Dr. Alexander Krugljakow, Germany
Prof. Sergey Dobatkin, Russia
Prof. Sergey Nikulin, Russia
Prof. Victor Anchev, Bulgaria

RESPONSIBLE SECRETARY:

Assoc. Prof. Tsanka Dikova, Bulgaria

MEMBERS:

Prof. Adel Mahmud, Iraq
Prof. Anna Proikova, Bulgaria
Prof. Bekir Sami Yilbas, Saudi Arabia
Prof. Dermot Brabazon, Ireland
Prof. Dipten Misra, India
Assoc. Prof.Eugeniy Grigoriev, Russia
Prof. F. W. Travis, United Kingdom
Prof. Gennagiy Bagluk, Ukraine
Assoc. Prof. Ibrahim E.Saklakoglu, Turkey
Prof. Iis Sopyan, Malaysia
Prof. Ivan Parshorov, Bulgaria
Prof. Ivanja Markova, Bulgaria
Prof. Janez Grum, Slovenia
Prof. Jens Bergstrom, Sweden
Prof. Leszek Dobrzanski, Poland
Prof. Ludmila Kaputkina, Russia
Prof. Nikolai Dulgerov, Bulgaria
Prof. Omer Keles, Turkey
Prof. Plamen Danev, Bulgaria
Prof. Rui Vilar, Portugal
Prof. Rusko Shishkov, Bulgaria
Prof. Saleem Hashmi, Ireland
Dr. Sefika Kasman, Turkey
Prof. Seiji Katayama, Japan
Prof. Souren Mitra, India
Dr. Sumsun Naher, United Kingdom
Prof. Svetlana Gubenko, Ukraine
Prof. Sveto Cvetkovski, Macedonia
Prof. Ventsislav Toshkov, Bulgaria
Prof. Yovka Dragieva, Bulgaria

C O N T E N T S

THE ROLE OF INTERFACES AND CHARGE OF A MOLECULE IN THE PROCESSES OF NONEQUILIBRIUM CRYSTALLIZATION OF PEPTIDE NANOBIOMATERIALS
PhD , Ass. Prof., Loskutov A. 37

PECULIARITIES OF THE STRUCTURE FORMATION OF MATERIALS OF AL-CU AND AL-CU-C SYSTEMS UNDER THE CONDITIONS OF SPARK-PLASMA SINTERING
Prof., Dr. of Science Syzonenko O., PhD Prystash M., PhD Zaichenko A, Kovalenko O. 41

THE THEORY OF DIRECT MARTENSITIC TRANSFORMATIONS OF STEELS
PhD. Tech. Sci. Skoromnaya S. 45

EFFECT OF LOW-FREQUENCY VIBRATION ON THE STRUCTURE AND RESIDUAL STRESSES IN SLM Ti-6Al-4V ALLOY
Kazantseva N., Rumyantsev S. Fefelov A., Merkushev A., Ezhov I., Vinogradova N. Davydov D. 49

MANUFACTURING OF IONIZING RADIATION SOURCE OF IRUDIUM-192 FOR GAMMA-DEFECTOSCOPES OF GAMMARID-192/120M
Dr. Ashrapov U.T., Dr. Khujaev S.S., Dr. Khalikov U.A., Eng. Isaev Y.A. 52

COMPARATIVE INVESTIGATIONS OF THE MECHANICALLY ALLOYED and PRESSURELESS SINTERED Al–7 wt.% Si COMPOSITES REINFORCED WITH VARIOUS BORIDE PARTICLES
M.Sc. Mertdinç S., M.Sc. Tekoğlu, E., Dr. Ağaoğulları, D., Prof. Dr. Öveçoğlu, M.L. 55

EFFECT OF CASE HARDENING PROCESS PARAMETERS OF ALLOY STEELS ON THEIR WEAR CHARACTERISTICS
Prof. EL-Hebeary, M.R., MSc. EL-Sawy, E.E.T., Prof. EL-Bahloul,A.M.M. 59

DIRECT OBSERVATION OF THERMAL EFFECT APPEARANCE DURING GRAIN BOUNDARIES COMPLETE WETTING TRANSITION IN COPPER-BISMUTH SYSTEM
Ass. Novikov A., PhD Kondratiev A., Prof. Dr. Eng. Bokstein D.,Prof. Dr. Eng. Petelin A., PhD Novikova E. 63

ELECTRODEPOSITION OF SILVER AND ITS INFLUENCE ON THE FORMATION OF COATINGS OF MOLYBDENUM CARBIDE IN TUNGSTATE-MOLYBDATE-CARBONATE MELTS
Prof., Dr. Sc. Malyshev V., Prof., Dr. Sc. Kushchevska N.., Prof., Dr. Sc. Bagliuk G. D.Sc., Ph.Dr. Gab A., Ph. Dr. Lukashenko T., Prof., Dr. Sc. Gaune-Escard M. 66

DEVELOPMENT OF METHODS FOR CALCULATING THE NONEQUILIBRIUM PHASE TRANSFORMATIONS DURING THE CONDENSATION OF SUPERCOOLED STEAM IN THE TURBINE FLOW PATH
Member-corresp., Dr., Prof. Shubenko O., PhD., Sen. Res. Babak M., PhD., Sen. Res. Senetskyi O., Eng. Senetskaya D. 69

THE ROLE OF INTERFACES AND CHARGE OF A MOLECULE IN THE PROCESSES OF NONEQUILIBRIUM CRYSTALLIZATION OF PEPTIDE NANOBIOMATERIALS

PhD , Ass. Prof., Loskutov A.
Institute of Robotics - Moscow State Technological University "STANKIN", Vadkovskii per. 1, Moscow, 127994 Russian Federation
ailoskutov@yandex.ru

Abstract**:** *The influence of various factors on the processes of nonequilibrium crystallization of dipeptide (DPT) from its aqueous solutions has been studied. The nonequilibrium crystallization leads to the formation of spatially heterogeneous structures. Depending on the charge of the DPT molecule (neutral or anion), not only the morphology of the surface of the layers changes, but also its electronic structure. The important role is played by the properties of the substrate-layer interfaces, which are responsible for the formation of ferroelectrics on gold during the crystallization of the DPT anion. The structure of the solid layers is also significantly affected by charges on the substrate surface, which can partially or completely compensate for the charges of individual functional groups in the PT molecule. The observed effects of bipolar resistive switching in peptide layers and the formation of ferroelectrics can find practical application as a smart material of memristor organic electronics.*

Keywords: CRYSTALLIZATION, PHASE TRANSFORMATIONS, SMART BIOMATERIALS, NANOPARTICLES, MEMRISTORS

1. Introduction

The use of biological objects and the principles of their functioning for the organization of matter at the molecular level - biomimetic - is an actual and intensively developing direction in nanotechnology. Discoveries in it gave impetus to the creation of new functional (smart) materials. The characteristic feature that actually makes them smart is their ability to respond to very slight changes in the surrounding environment. The uniqueness of these materials lies not only in the fast macroscopic changes occurring in their structure but also these transitions being reversible. It is assumed that such materials can replace metals as conductors of current, while retaining their inherent resistance and ductility. Also it was found that the hardness of peptide (PTs) nanospheres formed as a result of the self-organization of simple protected DPTs turned out to be higher than the hardness of steel. On the basis of PTs, a material with unique adhesion properties and providing super-strong adhesion was developed.

At present, in spite of the continuously increasing number of PTs studies, the regularities of their binding to solids and the formation of solid structures from them remain to be studied. In order to reliably control the formation of PTs based self-organized structures on solid surfaces, it is necessary to elucidate the roles of different factors in this process, such as: the molecule chemistry, its charge, the chemical nature of a substrate surface and the presence of various defects or foreign “structural” units on it.

Methods of colloid chemistry make it possible to create various ordered nanostructures on solid surfaces as a result of self-assembly and self-organization processes. At the same time, they are characterized by high efficiency, manufacturability and low costs. Unfortunately, the mechanisms for the formation of solid-phase nanostructures are still not disclosed. As a result, there is no possibility of complete control over the technological processes of their production (coatings, 3D printing, etc.).

There is a considerable interest in the processes of self-organization that occur during crystallization from a melt or solidification from a solution. First of all this is due to fundamental problems, in particular, to the problem of molecular design. However, the relationship between molecular structure and macroscopic supramolecular organization is very complex and poorly understood. Therefore, based solely on the structure of the PT molecule, it is very difficult to predict the final structure and properties of solid-phase coatings based on it in advance. So a high level of understanding of the underlying processes and mechanisms is required. All this requires more detailed studies of all stages of the processes of PTs crystallization and the influence of various factors on them.

Previously we investigated basically the synthesis of various bionanocomposites, including different PTs [1-3]. These studies have shown that PT composite materials and coatings with silver and gold nanoparticles (NPs) do have a variety of structural, electrical and tribological properties that make them promising for large-scale practical applications in engineering. Also it was found that due to the specific zwitterionic structure of their molecule, it is possible to modify its chemical, electrical and structural properties simply by changing pH of solution. In this communication, we report the results of studying the influence of molecule charge and different interfaces on the structure and electrical properties of PTs materials to determine the structure-property relationship of the formed layers and the feasibility of practical application of DPT in engineering, for example, as a smart material of organic electronics.

2. Experimental section

In this report, a short DPT {HOOC-$(CH_2)_2$-CO-Glu-Lys-NH-$(CH_2)_3\}_2$ was taken [3]. It belongs to the class of short PTs of neuroprotective effect
and is a mimetic of nerve growth factor. Its structural formula is shown in Fig. 1.

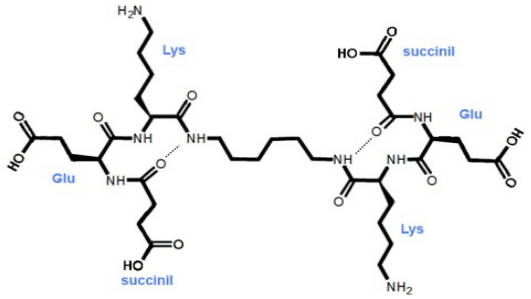


Fig. 1. *Structure of dipeptide molecule.*

When studying the processes of crystallization of DPT layers, the methods of probe microscopy and spectroscopy (AFM, STM, STS), IR and Raman spectroscopy, XPS, interference microscopy and dynamic light scattering were used. The experiments were carried out at pH values 4.2 (neutral molecule) (DPT-0) and 7.6 (anion) (DPT-1) by adding K_2CO_3 solution. In each experiment 10 ml of DPT aqueous solution at different pH was deposited at room temperature on the surface of polycrystalline gold films, as well as on the cleaned glass and freshly prepared mica and HOPG (ZYH with misorientation angles of 3.5°-5°) surfaces. The deposited DPT layers were dried in air at room temperature. Two methods of deposition were used: drop casting and spin coating at 2000–3000 rpm, resulting in thin and ultrathin layers, respectively. The maximum height of the formed thin layer at the boundary of the drop was ≤ 0.5 μm.

3. Results and discussion

The evaporating drop of a colloidal solution deposited on a solid surface is a complex strictly non equilibrium system in which the degree of supersaturation continuously changes, local gradients of

concentrations and temperatures appear, and processes of mass transfer of the solute to the drop boundary proceed. The final structure of the composite layer, which can not be predicted in advance, will be determined by the action of a variety of forces, particle sizes and concentration of reagents. Therefore, the structures of thin layers formed in the center and on the rim of the drop can differ significantly. The limited volume of the article does not allow us to present and consider all changes in the structure and morphology of the formed solid layers that are observed moving the probe from the center of the drop to its periphery. Thus, when moving in the radial direction from the center to the edge of the drop, along with the change in structure, the thickness of the layer also increases and reaches its maximum at drop boundary where the rim is formed. Only the most characteristic structures in our opinion are listed here.

At the initial stages of crystallization, the self-assembly of DPT-0 NPs begins on the gold surface (Fig.2a). Their average size is ca. 50 nm and the aspect ratio (height/diameter) is 1/10. They are assembled into separate units, the forms of which are very diverse.

The layers of DPT-1 on the surface of gold also consist of separate flat NPs, but in this case they form chains with a width of 400-600 nm, oriented in a certain direction (Fig. 2b). The directed aggregation of DPT-1 NPs into anisotropic chain-like structures proceeds probably according to the mechanism of bridge formation between adjacent NPs via non-covalent interparticle interactions.

In the of DPT-1 layers on graphite, a growth of monolayers is observed. Their height is ≤ 0.9 nm (Fig.2c). This is very close to the calculated value for an anion of 0.7 nm [4].

Fig. 2d presents 3-d image of ultrathin DPT-1 layer on mica. In this case the individual mesocrystals are growing. Their height is less than 80 nm, and the angles formed by the crystal faces are 60° and 120°. These structural features indicate on one side a higher degree of perfection of such mesocrystals and on the other side, that the growth front is formed by certain crystal facets. In addition to mesocrystals, individual filaments are also can be seen. The height of these filaments does not exceed 4 nm.

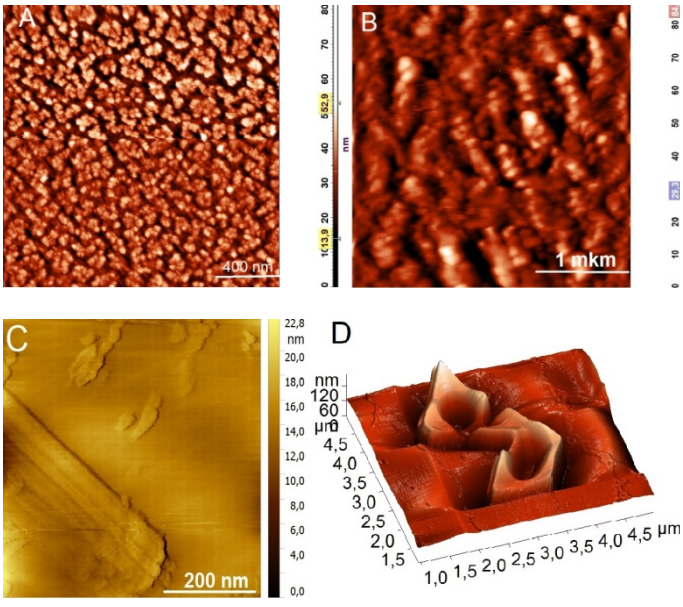


Fig.2. *Examples of self-assembly of DPT molecules in ultrathin layers, DPT-0 (a), DPT-1 (a,b,c) - on gold (a,b), graphite(c) and mica (d)*

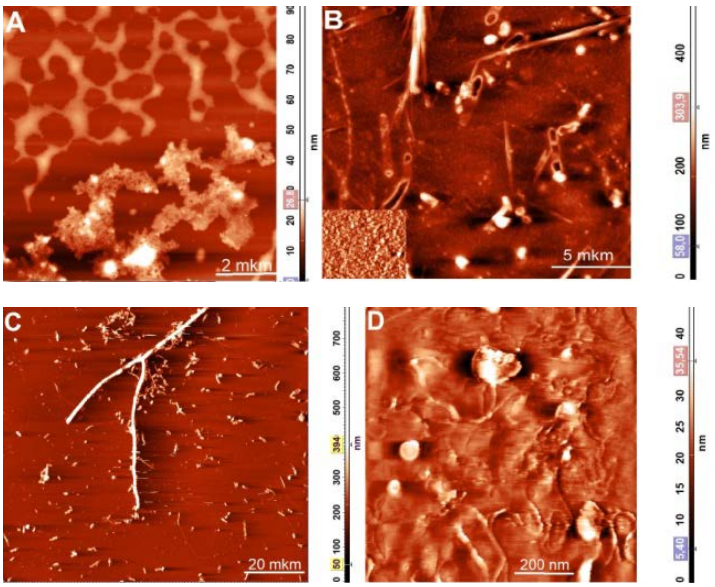


Fig.3. *AFM images of thin layers of DPT-0 on the surfaces of mica (a), gold (b), glass (c) and graphite (d).*

In thin layers of DPT-0 on the surface of mica the coalescence of islands are observed. They have equal thickness about ≈ 2-3 nm (Fig. 3a). Between the individual islands bridges are formed. In this case, structures similar to honeycombs appear. Near the rim there is a coalescence of individual particles of micron size with the formation of a continuous layer with a height up to 35 nm. It should be noted that the growth of such aggregates is observed only at the edges of the drop.

On the surface of gold, the formation of various linear 3-d chains or short rods begins atop of a layer consisting of tightly packed ‘‘pancakes’’ which can be seen at higher resolutions (left corner of Fig. 3b). There is a certain similarity between the DPT-0 structures on mica and gold. Indeed, at the center of the drop on mica, we also see layers consisting of tightly packed NPs, similar to Fig.3b, and only upon moving toward the drop boundary, the growth of individual 3-d aggregates begins. Their length can reach ≥ 10 microns.The morphology of thin layers of DPT-0 on the glass surface can be characterized as having elongated short chains formed by individual flat particles as main structural elements of self-assembling (Fig. 3c). These building blocks forms 100-mkm-long chains composed of individual flat particles with an average length of ca. 800 nm, a width of 1.2 mkm and a height of 100-150 nm. Similar to the gold surface the chains are also built atop of the layer consisting of tightly packed NPs. Thin layers of DPT-0 on graphite completely cover its surface, forming a continuous layer, which has no pronounced relief (Fig. 3d).

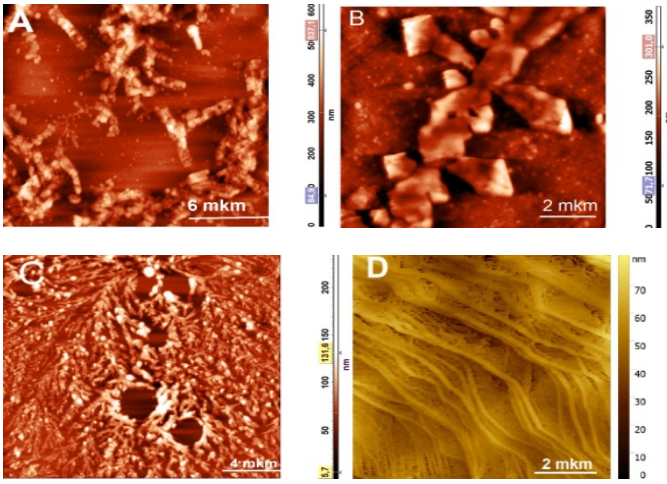


Fig.4. *AFM-STM images of thin layers of DPT-1 on the surfaces of mica (a), gold (b), glass at pH 10 (c) and graphite (d).*

On mica the self-assembly of DPT-1 particles takes place with the formation of aggregates of various shapes (Fig. 4a). The growth of various crystals oriented in two perpendicular directions occurs on the surface of gold atop a layer of densely packed particles (Fig. 4b). At pH 10 on glass substrate, DPT-1 chains build dendrite structures (Fig. 4c). The angle between the branches of dendrites is 30-40°. The formation of such structures was never observed upon DPT-0 crystallization.

In thin layers of DPT-1 on the graphite surface the growth of extended fibrous structures of different widths is observed (Fig. 4d). At a higher resolution, it can be seen that these strands have different widths. The ultra thin DPT-1 layers crystallize on the graphite surface in accordance with the mechanism of 2-d (layer-by-layer) growth of monolayers, so the topography of the clean surface of graphite is copied.

The local tunneling current-voltage characteristics (LTCVC) DPT-0 and DPT-1 layers on gold and graphite are very different (Fig.5).

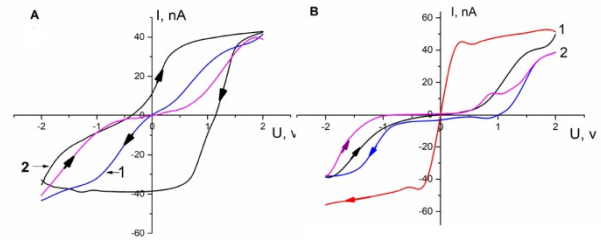


Fig.5. *LTCVC of DPT-0 (1) and DPT-1 (2) on the surface of gold (A) and graphite (B)*

The greatest differences are observed on a gold substrate. In this case, the width of the energy band (E_g) at points on the surface, located at a distance of less than 200 nm, can vary from 0 to 3 eV, the change in the form of LTCVC on different samples is caused by a change in the local work function or the local density of electronic states (LDOS) of the substrate-DPT-tip system. For all LTCVC, the nonlinear form is characteristic and is conformed the model of currents, limited by the space charge.

Regardless of the nature of the substrate and molecule charge, the effect of bipolar resistive switching is observed at all LTVACs, i.e. presence of areas of high (OFF) and low (SET) resistance, depending on the forward or reverse direction of the current. When a molecule becomes an anion, the order of their succession also changes. Thus, the switching effect depends mainly on the charge of the DPT molecule, not on the substrate. The most interesting result is the presence of hysteresis of LTCVC in the DPT-1 layers on the gold surface (Fig.5a). This indicates the existence of residual polarization and the formation of a ferroelectric. An increase in the crystallization temperature of DPT to 90° C on the gold surface does not change the shape of the CVC of the DPT-1 layers and, consequently, its electronic structure. In the case of DPT-0 layers, they become dielectrics with $E_g \geq 3$ eV. However, in this case it does not become a ferroelectric.

The significant local nonuniformity of the electronic structure of DPT layers was found. It is primarily associated with the chosen method of material deposition. Indeed, the evaporation of water from the surface of the drop begins at its periphery, and ends at its center. Therefore, during the evaporation process local DPT concentrations in the drop volume continuously change. In addition, with a decrease in the drop area, the rate of evaporation of water sharply increases; the crystallization conditions change and the formed layer is disordered. So the thickness of the DPT layer and morphology of its surface at the center and at the rim are significantly different. When measuring LTCVCs, a change in the thickness of the layers will also lead to a change in the local strength of the electric field. Thus, the formed layers would have a local lateral disorder in both the interface region and the volume of the layer. In this case the charge injection process also becomes laterally heterogeneous and acquires a filamentary character.

To summarize the experimental results including spectral data, firstly it is necessary to consider the conformation of the neutral (DPT-0) and ionized (DPT-1) molecule and their interactions with gold, graphite, mica and glass surfaces. The total charge of DPT molecule depends on pH, because it contains amino acids with ionic side groups. Molecule is neutral when pH reaches the value of 3-4 and is characterized by four stabilizing intramolecular hydrogen bonds. Then with increasing pH, DPT becomes negatively charged due to the acid dissociation of two terminal carboxylic groups at first, and at pH > 10, the negative charge reaches the value - 4 due to the acid dissociation of two carboxylic groups at the side chains of the glutamic acid residues. The pH range of 7-8 corresponds to DPT molecule having one or two ionized terminal carboxyl groups; and two uncharged amino groups of lysine residues. They can participate in coordination with the surfaces of different substrates. Conformation of an isolated anion in a strongly basic environment is stabilized by eight intramolecular hydrogen bonds. Because of the repulsion of like-charged groups, the DPT chain stretches and its radius of gyration increases. Therefore, the height of the anion decreases in comparison with the height of the neutral molecule (1.2-1,5nm). This is what we observe in the ultrathin layer on the graphite surface.

Owing to amphiphilic character of molecule the presence of water-soluble functional groups of PT molecule (antennas) and hydrophobic hydrocarbon chain, DPT chains self-organize differently on the substrates of various polarities.

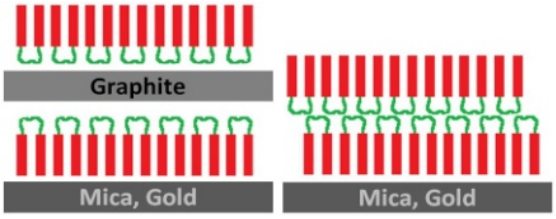


Fig.6. *The scheme of DPT monolayers orientation on graphite, gold and mica surfaces, PTs antennas - red, hydrophobic linkers –green [4]*

The materials we studied differ not only in their structure and chemical composition, but also in the surface charge. Indeed, the surfaces of graphite and glass are electrically neutral, and on the surface of gold a positive charge arises only when DPT-1 is deposited (image charge). The surface of mica, which is a classical dielectric, contains an equal number of positive and negative charges. If two terminal carboxylic groups are negatively charged two antennas of DPT are anchored on mica surface through hydrogen bonding and electrostatically. Remaining part of the molecule including its central hydrophobic unit stays non-adsorbed due to the high surface charge of muscovite (Fig.6).

Therefore, when DPT-0 and DPT-1 are deposited on the surface of gold and mica, the nature of their interactions will be significantly different. Initially neutral surface of gold during adsorption of DPT-0 remains neutral and DPT chain adsorbs entirely, and upon adsorption of anion DPT-1 is charged positively. All this contributes to the localization of the DPT-1 molecule on the surface of mica and gold.

The silanol SiOH groups on the silica surface can participate in hydrogen bonding with PT chains. The interaction between molecules is weak hydrogen bonding between amino- and carboxylic groups and silanol groups of the silica. The surface of graphite is the most inert and hydrophobic. After depositing the PT, it becomes hydrophilic, in contrast to, for example, mica and gold where initially hydrophilic surfaces become hydrophobic (Fig.6). The influence of the substrate is manifested in the way in which the growth mechanism of DPT layers changes from a layer-by-layer on graphite to a growth of individual 3-d aggregates with their subsequent coalescence on the surfaces of mica and gold.

On the non-charged surface of graphite DPT chain adsorbs entirely [3]. Here COOH and NH_2 groups build intramolecular hydrogen

bonds. Because of the van der Waals character of the interaction between the chain and the surface, the strength of the adsorption is moderate.

We have previously found out that self-organization in PT layers [1-2] is observed in case of weak particle-substrate interactions at poor wetting conditions and at low rate of solvent evaporation. Apparently, the stronger interactions between negatively charged carboxyl groups of DPT and positively charged mica and gold surfaces due to a large number of charges prevent the formation of extended ordered structures.

The crystallization processes are largely dependent not only on the nature of the substrate, but also on the surface roughness and the method of deposition used. As a consequence, at different areas of the same substrate, the various structures can be observed.

4. Conclusion

Our experimental results demonstrate that the structure and morphology of the thin layers of the DPT composites depend significantly on the properties of the substrate-layer interface. Otherwise, on different substrates, we would observe the same morphology of relatively thick layers. As a result, a diverse set of crystal morphologies is observed including disc-like particles, dendrites, chains and mesocrystals at all stages of DPT crystallization. Depending on the charge of the DPT molecule (neutral or anion), not only the morphology of the surface of the layers changes, but also its electronic structure. This is due to the fact that the crystallization of DPT-0 leads to the formation of an organic crystal with covalent and hydrogen bonds, and DPT-1 to the formation of a DPT-1 salt with an ionic bond type. The important role is played by the properties of the substrate-layer interfaces, which are responsible for the formation of ferroelectrics on gold during the crystallization of the DPT anion. The structure of the solid layers is also significantly affected by charges on the substrate surface, which can partially or completely compensate for the charges of individual functional groups in the PT molecule. It is known, that polymorphism plays an important role in the manufacture of drugs and products of fine organic chemistry. Since DPT we studied is also a drug, its various polymorphs can exhibit different bioavailability, stability, melting point, solubility. The effect of bipolar electrical switching allows usage these structures as elements of two-terminal resistive nonvolatile memory. Regardless of the specific mechanism for the appearance of CVC hysteresis DPT -1 can find practical application in memristor organic electronics.

This study was supported by the Ministry of Education and Science of the Russian Federation grant 9.1195.2017/4.6.

Literature

1. A. I. Loskutov, O. Ya. Uryupina, S. N. Grigor'ev et al, Colloid J., 2013, 75, p. 301-311.
2. A. I. Loskutov, O. Y. Uryupina, S. N. Grigor'ev et al, Protection of Metals and Physical Chemistry of Surfaces, 2015, 51, p.558-566.
3. A.I. Loskutov, O.A.Guskova, S.N.Grigor'ev et al, J. of Nanopart. Res., 2016, № 18, p. 238-254, DOI 10.1007/s11051-016-3548-1
4. O.A. Guskova, P.G. Khalatur, A.R. Khokhlov et al, Rus. J. Bioorg. Chem., 2010, 36:574–580. doi:10.1134/S10681620 10050043

PECULIARITIES OF THE STRUCTURE FORMATION OF MATERIALS OF AL-CU AND AL-CU-C SYSTEMS UNDER THE CONDITIONS OF SPARK-PLASMA SINTERING

Prof., Dr. of Science Syzonenko O., PhD Prystash M., PhD Zaichenko A, Kovalenko O.
Institute of Pulse Processes and Technologies of NAS of Ukraine – Mykolaiv, Ukraine,
E-mail: sizonenko43@rambler.ru

Abstract: The features of the structure formation of Al-Cu and Al-Cu-C materials under conditions of spark-plasma sintering under conditions of superposition of a direct and pulsating current at a temperature of 600ºC and a mechanical pressure of 60 MPa are studied. The obtained Al-Cu-C system materials with hardness from 400 to 1000 MPa, porosity from 3 to 1% are recommended for use as slip contacts, and also as antifriction materials in friction pairs either in dry (carbon-containing composites) or wet friction (composites not containing carbon).

Keywords: spark-plasma sintering, consolidation of powders, structurization, synthesis, intermetallic compound

1.Introduction

The development of technology and electronics is accompanied by the need for materials with high thermal conductivity, electrical conductivity along with higher tribological characteristics. Such properties are possessed by copper, and also composites on its basis. However, according to the London Metal Exchange in February 2016, the cost of copper on the international market was $ 4,400 per ton, and in February 2018 this figure exceeded the mark of $ 7,200 per ton. This state of affairs diverts the material scientists towards the search for a solution to the problem of synthesizing materials for electrical and tribological purposes with specified properties and reduced cost.

All over the world much attention is paid to the aluminum metallurgy, its alloys and the composites of the Al-Cu system. According to the scale of production and use, aluminum is second after iron, and aluminum-based alloys with added Cu obtained by casting are featured by high conductivity, hardness and durability due to $CuAl_2$ intermetallic phase, and they are handled perfectly in conditions of liquid friction at high loads and high speeds, however the technology of their manufacturing faces certain difficulties [1-4].

Problem discussion

The powder metallurgy methods enable changing the approach to obtaining aluminum-based products [5, 6] and allows producing lightweight, durable and high-density materials with good thermal and electrical conductivity.

In [7] the authors consider the possibility of the synthesis of the composite of Al-Cu-C system with the amount of carbon from 5% to 25% (wt). The synthesized composite material is recommended for use as a slip electric contact The material was received by the method of isostatic pressing at a temperature of 400°C and pressure of 40 Mpa with further holding at a temperature of 500-600°C for 360 minutes.

In [8], the method of spark-plasma sintering [9] was used to obtain compacts of the Al-Cu system, which allowed to reduce the consolidation time and temperature [10, 11]. Investigations of phase transformations in 78% Al - 22% Cu mixture with consolidation in the temperature range 400 - 525 ºC for 10 min at a pressure of 30 MPa have shown the possibility of synthesis of $CuAl_2$ intermetallic.

However, the kinetics of the formation of materials of Al-Cu, Al-Cu-C systems under spark-plasma sintering conditions, as well as the influence of the thickness of the transition intermetallic $CuAl_2$ zone on the material hardness have not been studied sufficiently.

The objective is to study the peculiarities of the structure formation of materials of t Al-Cu and Al-Cu-C systems under the conditions of spark-plasma sintering.

2.Objective and research methodologies

Al, Cu (60% of particles less than 20 μm) and graphite (80% of particles less than 10 μm) powders were used as elementary powders. Mixtures of weight content 50% Al-50% Cu, 75% Al-25% Cu, 87.5% Al-12.5 % Cu, 82% Al-12% Cu--6% C, 70% Al-25% Cu-5% C and 47% Al-47% Cu-6% C were prepared for consolidation purposes.

Powders were consolidated in vacuum by the GEFEST universal experimental complex (Fig.1) [12], which is based on passing through a powder superposition of direct and pulsating current with a frequency of 10 kHz at an operating voltage U = 2 V.

Sintering was carried out in matrices of graphite MPG 6 with an inner diameter of 10 mm, where 2 g of the powder mixture were poured. The powder was filled in layers to study the intermetallic of the transition layer. The temperature of the sample was measured on the wall of the matrix (ΔT between the outer surface of the matrix and samples varied from 150 to 250°) using a standard K-type thermocouple. The compaction pressure was ca. 30 MPa, and the sintering pressure was ca. 60 MPa. The thermocouple was calibrated according to the methods presented in [13].

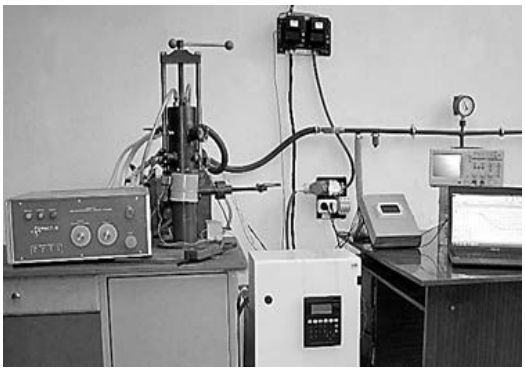


Figure 1. Appearance of GEFEST assembly

The consolidation temperature was chosen according to [8] and was 500 - 600ºC, the holding time was 20 min at a pressure of 60 MPa. Additional experiments were conducted for the 75% Al-25% Cu mixture with a holding time of 40, 80, and 120 min to study the kinetics of the formation of a transition layer in the solid-phase sintering of two-component powder mixtures [14]. The control of the sintering process was carried out with the help of specialized software [15]. The thermograms typical for consolidation of Al-Cu and Al-Cu-C systems are given in Fig. 2. As can be seen from Fig. 2, the holding temperature of the Al-Cu-C system is 100˚ greater than the holding temperature during sintering of the Al-Cu mixture.

The microstructure of the obtained compacts was analyzed as per DSTU ISO 643: 2009 using the BIOLAM-I microscope. To reveal the grain structure of aluminum, Keller's reagent (1% NaOH solution and 0.5% solution of hydrofluoric acid) was used. A 20% aqueous solution of HNO_3 was used to detect the phase of $CuAl_2$ [16].

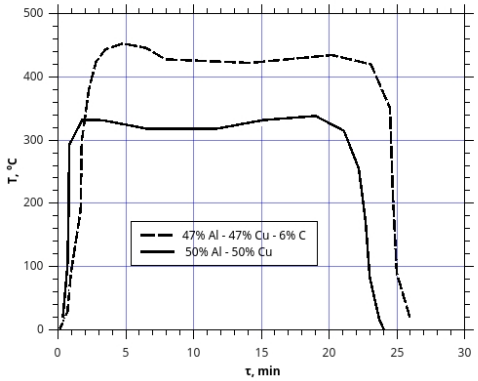


Figure 2. Typical thermograms obtained on the matrix surface during the consolidation of Al-Cu and Al-Cu-C powders

The compacts were tested for Vickers hardness at a load of 5 kg as per DSTU ISO 6507-1:2007, and since the obtained materials had a distinct transition zone between Al and Cu particles, a microhardness determination method was used which allowed estimating the hardness of individual phases of Cu, Al and $CuAl_2$ as per GOST 9450-76 on the device PMT-3.

As a result of consolidation of a powder mixture of 75% Al-5% Cu for 20 min, it was established that in the chosen mode the diffusion processes begin to occur between the aluminum and copper particles [17], which lead to the formation of a two-layer region of the transition zone: eutectic α (Al)-$CuAl_2$ (light area) and intermetallic $CuAl_2$ (dark area) (Fig. 3, 4). The thickness of the $CuAl_2$ zone depends on the holding time and increases to 6 μm with 80 minutes of consolidation (Fig. 5). A further increase in the holding time leads to dissolution of $CuAl_2$ in aluminum [18] and a decrease in the thickness of its layer to 2 μm at 120 minutes of holding.

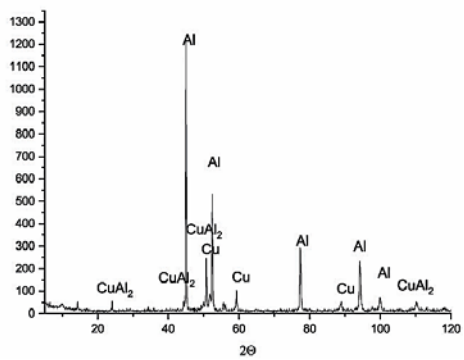
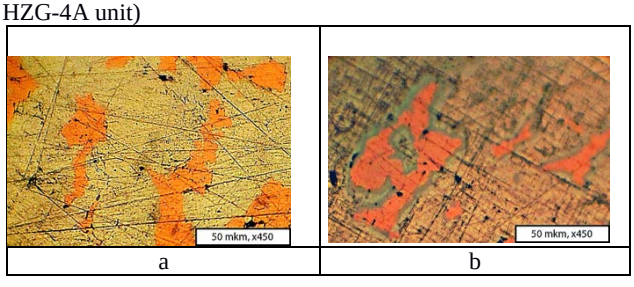
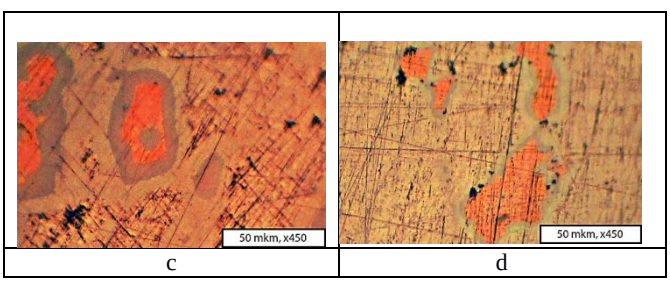


Figure 3. Phase composition of a 75% Al-25% Cu mixture after 20 min of consolidation (CoKα - radiation from the HZG-4A unit)





a) 20 min; b) 40 min; c) 80 min; d) 120 min

Figure 4. Photomicrographs of a transition layer between aluminum and copper particles at different holding times

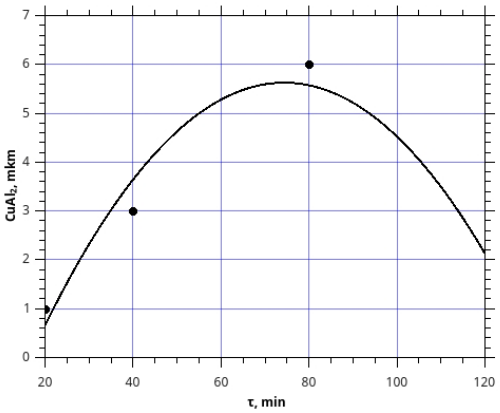


Figure 5. Thickness of the transition layer vs. holding time

The microhardness of the $CuAl_2$ layer is ca. 5 GPa, microhardness of aluminum is ca. 0.4 GPa and copper ca. 0.5 GPa. It is evident that an increase in the thickness of the intermetallic layer also affects the overall hardness of the entire compact. Thus, an increase in the thickness of the $CuAl_2$ layer from 1 μm to 6 μm makes it possible to increase the Vickers hardness of the compact from 330 MPa to 870 MPa (Fig. 6).

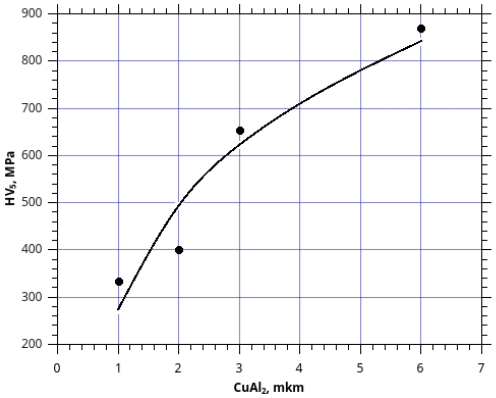
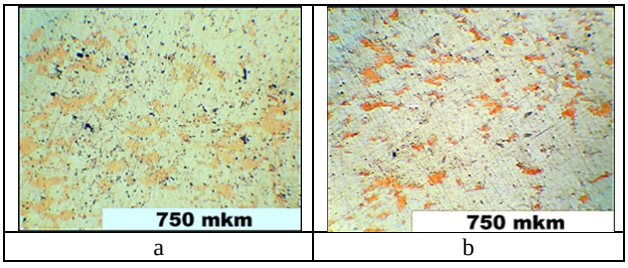
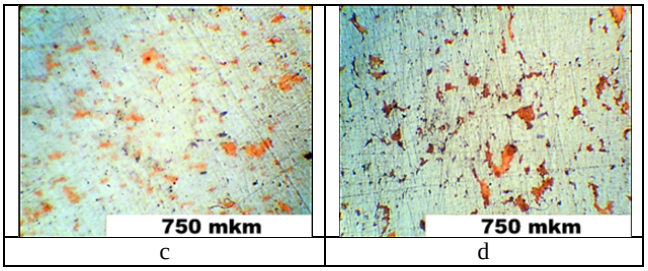


Figure 6. Vickers hardness of consolidated samples of 75% Al- 25% Cu mixture vs. thickness of the $CuAl_2$ intermetallic layer.

The exposure time also affected the porosity of the compacts received. 75% Al-25% Cu samples consolidated for 20 min have a porosity less than 3%. Increasing holding time from 20 to 120 min leads to a decrease in porosity (Fig. 7), so at 40 min the porosity is 1.4%, at 80 min - 0.98%, and at 120 min - 0.5% (Fig. 8).





c d

a) 20 min; b) 40 min; c) 80 min; d) 120 min

Figure 7. Microphotographs of porosity change of a material over increasing holding time, x100

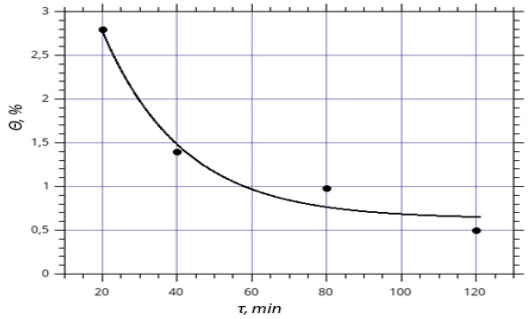
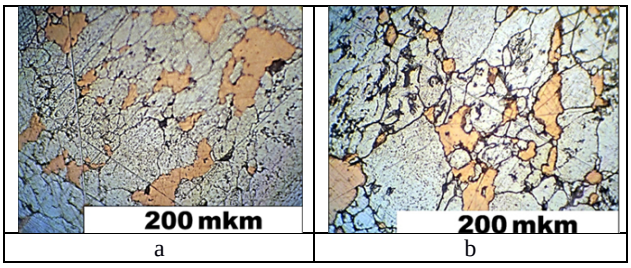


Figure 8. Porosity vs. holding time

By identifying the aluminum structure in consolidated materials we managed to establish that the increase in the holding time had no significant effect on the particle size of the consolidated powder (Fig. 9) and it corresponds to the initial sizes of the Al and Cu powders.

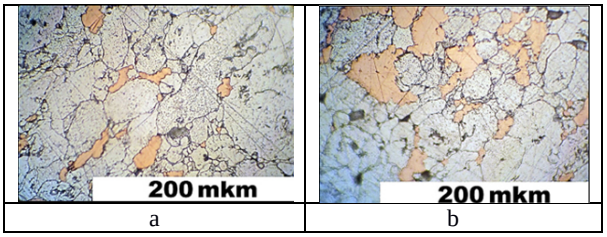


a b

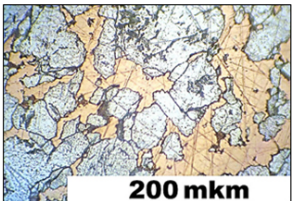
a) 20 min; b) 120 min.

Figure 9. Structure of 75% Al-25% Cu sample after applying Keller's reagent, x450

Consolidation of mixtures of 50% Al-50% Cu, 75% Al-25% Cu and 87.5% Al-12.5 % Cu composition showed that in the selected two-component mixtures the increase in the amount of copper does not significantly affect the thickness of the $CuAl_2$ intermetallic layer, which is from 1 to 1.5 μm (Fig. 10), with the Vickers hardness of the obtained materials ranging from 350 to 400 MPa. (Fig. 11). It should be noted that the obtained thickness values of the intermetallic layer and the hardness of the material are completely consistent with the dependences previously yielded and shown in Fig. 5. and Fig. 6.



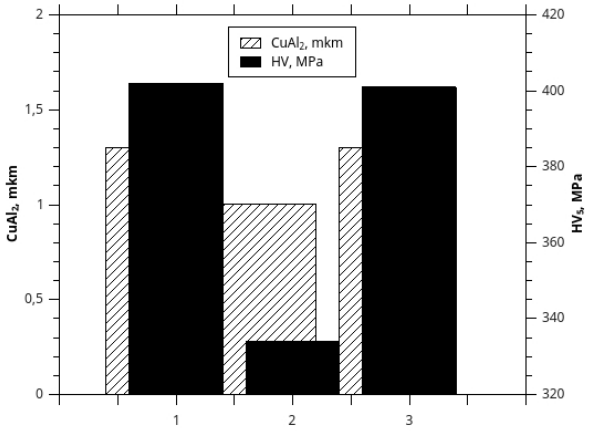
a b



c

a) 87.5% Al-12.5% Cu; b) 75% Al-25 % Cu; c) 50% Al--50% Cu

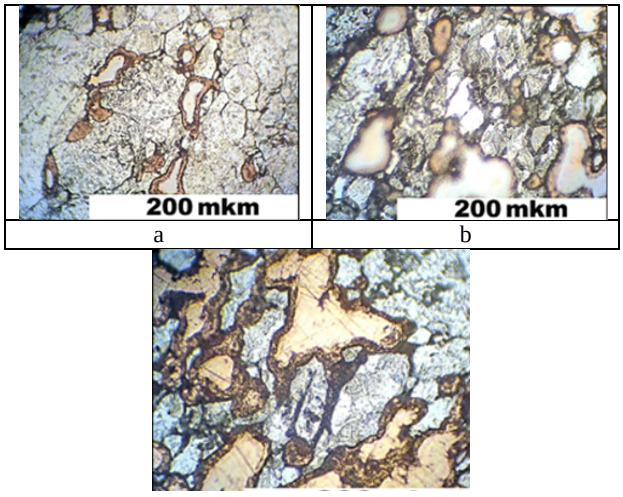
Figure 10. Structure of Al Cu samples after applying Keller's reagent, x450



1) 87.5% Al-12.5% Cu; 2) 75% Al-25% Cu; 3) 50% Al-50% Cu

Figure 11. The thickness of the intermetallic $CuAl_2$ layer and Vickers hardness of Al-Cu composites

Consolidation of 82% Al-12% Cu-6% C, 70% Al-25% Cu-5% C and 47% Al-47% Cu-6% C mixtures revealed that the introduction of a mixture of carbon intensifies the formation of an intermetallic compound $CuAl_2$ (Fig. 12). Thus, for the 82% Al-12% Cu-6% C mixture the characteristic thickness of the intermetallic layer between particles is 2.5 μm (Fig. 13), and for the 47% Al-47% Cu-6% C 7.5 μm. By increasing the amount of $CuAl_2$ (Fig. 14) we yielded the Al-Cu-C materials having a Vickness hardness from 700 to 1,100 MPa. The obtained values of the thickness of the intermetallic layer and the hardness of the material, as well as for the Al-Cu system, completely agree with the dependences in Fig. 5. and Fig. 6 previously obtained.

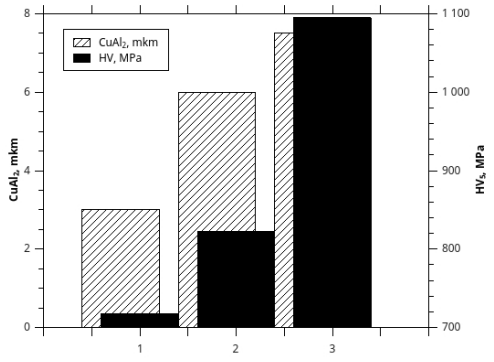


a b

c

a) 82% Al-12% Cu-6% C; b) 70% Al-25% Cu-5% C; c) 47% Al-47% Cu-6% C

Figure 12. The structure of Al-Cu-C samples after applying theKeller's reagent, x450



1) 82% Al- 12% Cu-6% C; 2) 70% Al-25% Cu-5% C; 3) 47% Al-47% Cu-6% C

Figure 13. The thickness of the intermetallic $CuAl_2$ layer and Vickers hardness of Al-Cu-C composites

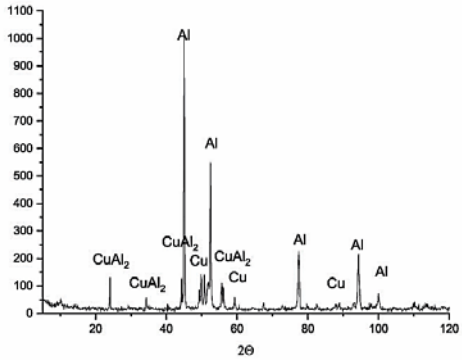


Figure 14. Phase composition of 70% Al-25% Cu-5% C mixture after 20 min of consolidation (CoKα-radiation from HZG-4A unit)

4. Conclusions

1.The features of consolidation and structure formation of materials of the Al-Cu and Al-Cu-C system under conditions of spark-plasma sintering are studied. It is established that under the conditions of spark-plasma sintering, the synthesis of $CuAl_2$ intermetallic is initiated in Al-Cu and Al-Cu-C systems. Moreover, in the composite which contains carbon, the thickness of the intermetallic layer is 2 times greater.

2.Increasing the thickness of the intermetallic layer affects the overall hardness of the entire compact. Thus, an increase in the thickness of the $CuAl_2$ layer from 1 μm to 6 μm makes it possible to increase the Vickers hardness of the compact from 330 MPa to 870 MPa.

3.The thickness of the $CuAl_2$ zone depends on the holding time and increases to 6 μm with 80 minutes of consolidation. A further increase in the holding time leads to the dissolution of $CuAl_2$ in aluminum.

4.The obtained Al-Cu-C system materials with hardness from 400 to 1000 MPa, porosity from 3 to 1% can be recommended for use as slip contacts, and also as antifriction materials in friction pairs either in dry (carbon-containing composites) or wet friction (composites not containing carbon).

5. Literature

1. Snyder, J.; Fujita, T.; Chen, M.W.; Erlebacher, J. (2010) Oxygen reduction in nanoporous metal–ionic liquid composite electrocatalysts. *Nature Materials*, 9 (11), 904–907.

2. Qi, Z.; Zhao, C.; Wang, X.; Lin, J.; Shao, W.; Zhang, Z.; Bian, X. (2009) Formation and characterization of monolithic nano-porous copper by chemical dealloying of Al–Cu alloys. *The Journal of Physics Chemistry*, 113 (16), 6694–6698.

3. Li, Z.; Lu, X.; Qin, Z. (2013) Formation of nanoporous silver by dealloying $Ag_{22}Zn_{78}$ alloy at low temperature in H_2SO_4. *International Journal of Electrochemical Science*, 8 (3), 564–3571.

4. Chen, L.Y.; Yu, J.S.; Fujita, T.; Chen, M.W. (2009) Nanoporous copper with tunable nanoporosity for SERS applications. *Advanced Function Materials*, 19, 1221–1226.

5. Osokin, E. Artemieva, O. (2008) *Powder Metallurgy Processes*. [ebook] Krasnoyarsk: IPK SFU, 421. Available at: http://files.lib.sfu-kras.ru/ebibl/umkd/63/u_lectures.pdf [Accessed 22 Jun. 2016]. ISBN 978-5-7638-1523-8

6. Makhlouf, M, Bachaga, T, Sunol, J, Dammak, M and Khitouni, M (2016) Synthesis and Characterization of Nanocrystalline Al-20 at. % Cu Powders Produced by Mechanical Alloying, *Metals*, vol. 6, no. 7, p. 145.

7. Aminov, J.B., Akramov, M.B., Aminov, B. Majidov, Kh. (2013) Production and research of composite Al-based materials a powder metallurgy method. *Reports of the Academy of Sciences of the Republic of Tajikistan*, 56 (2), 136–139.

8. Q. Kong, L. Lian, Y. Liu and J. Zhang. (2014) Fabrication and Characterization of Nanocrystalline Al–Cu Alloy by Spark Plasma Sintering, *Materials and Manufacturing Processes*, vol. 29, no. 10, pp. 1232-1236.

9. Mamedov, V. (2002) Spark plasma sintering as advanced PM sintering method. Powder Metallurgy, 45, 322–328

10. Khor, K.A.; Yu, L.G.; Stephani, G. (2003) Effect of spark plasma sintering (SPS) on the microstructure and mechanical properties of randomly packed hollow sphere (RHS) cell wall. *Materials Science Engineering*, 356, 130–135.

11. Toyofuku, N.; Kuramoto, T.; Imai, T.; Ohyanagi, M.; Munir, Z.A. (2012) Effect of pulsed DC current on neck growth between tungsten wires and tungsten plates during the initial stage of sintering by the spark plasma sintering method. *Journal of Materials Science*, 47, 2201–2205.

12. Patent of Ukraine No. 107729, MPK (2006.01) B22F 3/14, B22F 3/12, B22F 3/105. Device for obtaining consolidated powder materials/Sizonenko O.N, Ivliev A.I., Grigoriev E.G.; Applicant and patent holder - Institute of Pulse Processes and Technologies of the National Academy of Sciences of Ukraine. - No. a201305519; applied on 29.04.13; published on 10.02.15, Bulletin No. 3. – 6 p.

13. Rubinstein, S.A. Levant, G.A., Ornis, N.M., Tarasevich, Yu. S. (1968) Fundamentals of the theory of cutting metals and cutting tools. - Moscow: Mashinostroyeniye, 392 p.

14. Pines, B.Ya., Geguzin, Ya.E. (1953) Self-diffusion and heterodiffusion in inhomogeneous porous bodies. *Journal of Techn. Physics.*, 23 (9), 1559–1572.

15. Sizonenko, O.N., Litvinov, V.V., Konotop, S.V., Kovalenko, A.A. (2014) Automation of the process of measuring temperature, current and voltage during spark-caking sintering of dispersed compositions // Vestnik of the National Technical University "KhPI". Collection of scientific works. Thematic issue No. 21 (1064) "Engineering and electrophysics of high voltages" - Kharkov, 2014, 130–140.

16. Kovalenko, V.S. (1981) Metallographic Reagents: Handbook/Kovalenko, V.S. 3rd ed., Moscow: *Metallurgiya*, 120 p.

17. Avrahamov, Yu.S. Koshkin, V.I., Petrischev, I.M. Shlyapin, A.D. (2007) Preparation of alloys on the basis of systems of immiscible components by the contact alloying method. *Journal "Mashinostroyeniye i inzhenernoye obrazovaniye"*, 4, 21–30.

18. Baron, Yu. M. (2012) Building Materials Technology: Textbook for high schools, St. Petersburg: Piter, 512 p.

THE THEORY OF DIRECT MARTENSITIC TRANSFORMATIONS OF STEELS

ТЕОРИЯ ПРЯМЫХ МАРТЕНСИТНЫХ ПРЕВРАЩЕНИЙ СТАЛЕЙ

PhD. Tech. Sci. Skoromnaya S.

National Academy of Sciences of Ukraine, National Scientific Center
"Kharkov Institute of Physics and Technology" Kharkov, Ukraine
scoraya09@gmail.com

Abstract: *A theory of martensitic transformations of carbon steels based on the principle of detailed balance is proposed. This theory supplements the theory of Landau phase transitions in crystalline media, as well as the theory of crystallization of Kolmogorov's and Avrami's substance. In the proposed theory the martensitic transformations are described by the equations of induced transitions between two energy levels, which correspond to the number of particles of the initial phase with low energy (austenite) and the number of particles of the transformed phase with higher energy (martensite). The source of the transformations is the particles of the third kind - phonons, the number of which is associated with the induced transitions of particles between the energy levels and depends on the transformation temperature. The conclusions of the proposed theory correspond quantitatively to the experimental data.*

Keywords: *MARTENSITIC TRANSFORMATION, CARBON STEELS, ATHERMAL DIRECT MARTENSITIC TRANSITION, ISOTHERMAL DIRECT MARTENSITIC TRANSITION, TWO-LEVEL SYSTEM*

1. Introduction

During cooling of carbon steel being in γ-phase and characterized as austenite (phase *A*) its structural transformation occurs, which is associated with a change of the crystalline lattice symmetry. FCC symmetry of γ - phase transits to a new, more solid α - phase with BCC symmetry called martensite (phase *M*).

Phase transitions, in which the processes of diffusion and self-diffusion carry slowly, are direct martensitic transformations (DMT). DMT results in a large number of crystals *M* formed in each predefined grain of the initial phase *A*, which have the form of a plate with a thin by an order of magnitude smaller than its sizes in orthogonal directions to it. The size of crystals *M* depends on the initial state of grains *A*: homogeneous and perfect crystal structure *A* gives large crystals *M* and inhomogeneous, imperfect structure gives crystals of small sizes.

For DMT description in Landau theory [1] the expansion of Gibbs free energy is realized according to degrees of strain shear. But in some cases such an expansion does not describe experimental results [2-4]

Another approach consists in rigorous solution of the problem of substance crystallization [5, 6].

However, as practice shows, calculations of phase transformation kinetics using the Avrami equation do not always lead to correct results.

The discrepancies between the theoretical description of DMT and experimental data require further search for theories describing phase transformations in metals and alloys.

2. Physical model of phase transformations in crystalline media

Phase transformations in crystalline media according to their specific features can be described using a two-level system (TLS), the foundations of which have been formulated by Einstein A. [7].

Structural transformation of *A*-phase steel into *M*-phase steel can be characterized in TLS as spontaneous and induced transitions from stable state *A* to metastable state *M* and vice versa with probabilities corresponding to these transitions.

Schematic diagram of such transitions is presented in Fig. 1. In this figure the stable state is characterized by energy ε_A and temperature T_A and the metastable state is characterized by ε_M , T_M , at that $\varepsilon_A < \varepsilon_M$, $T_A > T_M$. The arrows in Fig. 1 denote: μ_{MA} - the probability of spontaneous transition from level *M* to level *A*; w_{MA} and w_{AM} - the probability of the induced transitions of the level *M* to the level *A* and vice versa respectively.

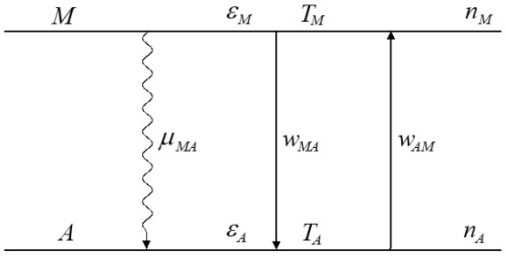


Fig. 1. *AM two-level system:* n_A *- number of elementary cells of phase A;* n_M *- number of elementary cells of phase M*

3. Equation system for description of DMT in carbon steel

When describing DMT in carbon steel the following requirement must be met: the increase in the number of elementary cells of phase *A* is equal to the decrease in the number of elementary cells of phase *M*, provided that the total number of cells is constant.

Let us consider the principle physics of transitions in carbon steel. However, it should be noted that these principle physics are, in our opinion, common for all systems subject to phase transformations.

During quenching the lattice atoms are displaced as a result of thermal vibrations, the concept of a phonon can be used for description of their energy. The phonon is characterized as a quasi-particle with energy $\varepsilon = \hbar\omega$ and quasi-momentum $\vec{p} = \hbar\vec{k}$, where, ω , $\vec{k}$ - frequency and wavenumber of the wave.

As the carbon steel temperature T decreases, the phonons acquire energy comparable to the energy barrier of the phase transition and their effect on the crystalline lattice of carbon steel will initiate the transitions of elementary cells from state *M* to state *A* and vice versa. Such transitions are induced, because they are caused by an external action associated with a temperature decrease. When interacting with *MA* two-level system the number of phonons should vary: decrease in the number of elementary cells of phase *M* leads to increase in phonons (phonon emission) and vice versa, increase in the number of elementary cells of phase *M* leads to decrease in the number of phonons (phonon absorption).

We consider two DMT modes of carbon steel below: athermal and isothermal.

4. *Athermal DMT of carbon steel*

Athermal DMT of carbon steel occurs at $T(t)$ decreasing within the range of $T_K \le T(t) \le T_H^*$, were T_H^* - initial temperature of the experiment $T_K \le T_H^* \le T_H$.

The initial equations of athermal DMT at a sufficiently large number of phonons ($N >> n_A, n_M$) are as follows:

$$\begin{aligned}
&\frac{\partial n_M}{\partial t} - \gamma \frac{\partial n_M}{\partial T} = \mu_{MA}(T)(n_A - n_M)N, \\
&\frac{\partial n_A}{\partial t} - \gamma \frac{\partial n_A}{\partial T} = -\mu_{MA}(T)(n_A - n_M)N, \\
&\frac{\partial N}{\partial t} - \gamma \frac{\partial N}{\partial T} = -\mu_{MA}(T)(n_A - n_M)N,
\end{aligned} \qquad (1)$$

were, $T(t) = T_H^* - \gamma t$ - temperature change in course of the time, $\gamma = (T_H^* - T_K)/t_{AM}$, $\mu_{MA} = w_{MA} = w_{AM}$ - the relation between the transition probabilities, which is valid at all temperatures.

To solve Eqs. (1) we determine the dependence of the probability of the induced transitions $\mu_{MA}(T)$ upon the temperature in the following form:

$$\mu_{MA}(T) = \mu(T_H^*)\left(1 - (1 - \beta k \tilde{T}^k)\exp\left[-\tilde{T}^k\right]\right), \qquad (2)$$

were, $\tilde{T}(T) = (T_H^* - T)/(T_H^* - T_K)$.

The representation (2) corresponds to the quenching method in one cooler when metal samples heated to the quenching temperature are immersed in the quench liquid until completely cooled.

As the temperature is decreased the velocity of DMT of phase *A* to phase *M* increases to the maximum value and then it decreases to zero, where the DMT velocity can be assumed to be proportional to the transition probability (2).

As the temperature is decreased from the initial $T = T_H^* \le T_H$ to $T = T_K$, DMT occurs in the alloy steel, as a result of which the elementary lattice cells of phase *A* almost completely transit to phase *M*.

The solution of equation system (1) under condition (2) has the following form:

$$N(\xi) \approx N_{eq}, \qquad (3)$$

$$n_M(\xi) \approx \frac{n_{M0} + n_{A0}}{2}\left(1 - \frac{n_{A0} - n_{M0}}{n_{M0} + n_{A0}} exp\left(-2\mu' N_{eq}\xi\right)\right) \qquad (4)$$

,

$$n_A(\xi) \approx \frac{n_{M0} + n_{A0}}{2}\left(1 + \frac{n_{A0} - n_{M0}}{n_{M0} + n_{A0}} exp\left(-2\mu' N_{eq}\xi\right)\right). \qquad (5)$$

were, $\xi(t,T) = t + F(T, T_H^*)$, $n_{M0} = n_M(0)$, $n_{A0} = n_A(0)$, $N_0 = N(0)$, $N_{eq} = N_0 - (n_{A0} - n_{M0})/2$, $\mu' = \mu(T_H^*)$, $F(T, T_H^*) = \frac{1}{\gamma}\int_{T_H^*}^{T}\left\{1 - \left(1 - \left(1 - \beta k(\tilde{T}(x))^k\right)\exp\left[-(\tilde{T}(x))^k\right]\right)\right\}dx$.

Analysis (3) - (5) shows that the total number of elementary cells that have transited from level *A* to level *M* is determined by the following expression:

$$n_{MS} = (n_{A0} + n_{M0})\left(1 - exp\left(-2\mu' N_{eq}\xi(t,T)\right)\right). \qquad (6)$$

Expression (6) is obtained as a result of summing the phase *M* for a large number of TLS with a short characteristic transition time ($\mu' t_{AM} >> 1$) into which the temperature interval is divided. Phase *M* is formed in each of these TLSs in such a way that the final state of one TLS determines the initial state of the subsequent TLS. The total amount of the transited phase *M* can be obtained by summing the phase *M* in each TLS to which the DMT temperature interval is divided.

Thus, it can be concluded from the expression (6) that as the temperature is decreased from the initial temperature $T = T_H^* \le T_H$ to $T = T_K$ then DMT occurs in the alloy steel as a result of which the elementary lattice cells of phase *A* almost completely transit to phase *M*.

5. *Isothermal DMT of carbon steel in high-temperature range*

The high temperature range will be considered as a specified by ratio $T_K \le T(t) \le T_H^*$. Intense thermal vibrations of the crystalline lattice are observed within this temperature range; it corresponds to availability of a large number of phonons in the system, i.e. $N_0 >> n_{A0}, n_{M0} >> 1$.

For example, for an isothermic DMT when quenched within heterogeneous temperature range Ac_3 the DMT velocity increases first from zero, reaches a maximum at T ~ 700° C then decreases and at <550 ° C assumes a small value [8].

For analytical description of isothermal DMT of carbon steel a solution for athermal DMT is applicable provided that the characteristic time of athermal DMT - t_{AM} must be replaced by the characteristic time of isothermal DMT - t_{AM}^* which is much greater than the first ($t_{AM}^* >> t_{AM}$). In this case, at a given experiment temperature T_H^* the expression (6) can be transformed to the following form:

$$\frac{n_{MS}}{(n_{M0} + n_{A0})} = \left(1 - exp\left(-2\mu' N_{eq} t\left(1 - exp\left(-\beta\left(\frac{t}{t_{AM}^*}\right)^k\right)\right)\right)\right) \qquad (7)$$

We used analytical dependence (7) to describe isothermic DMTs of steel ($Fe + 7\%Cr + 2\%Ni$) [2].

Comparison of the theoretical dependence (7) with experimental data [2] is carried out by transforming (7) to the percentage of the amount of the transformed phase *A* upon the time:

$$\frac{n_{AS}}{n_{A0}} = A \cdot 100 \cdot \left(1 - exp\left(-Bt\left(1 - exp\left(-Ct^k\right)\right)\right)\right), \qquad (8)$$

were, $A = 1 + n_{M0}/n_{A0}$, $B = 2\mu' N_{eq}$, $C = (t_{AM}^*)^{-k}$.

Digitized experimental curves [2] (points) and analytical solutions (8) (solid lines) are shown in Fig. 2 a), b).

Comparison of the analytical dependencies describing the isothermal DMT of one of the alloy steel types with experimental data (Fig. 2) shows their good quantitative agreement. This agreement indicates the possibility of describing DMT processes on the basis of the detailed balance principle formulated for elementary cells of phase *A* (austenite) and phase *M* (martensite) - the main participants of DMT kinetics.

The values of A, B, C, k coefficients obtained as a result of approximating the experimental data by the analytical dependence (8) are presented in Table 1.

6. *Isothermal DMT of carbon steel in low-temperature range*

As the temperature of martensitic transformations decreases, when $T_{Kом} \le T(t) \le T_H^* \le T_K$, the intensity of vibrations of the

crystalline lattice also decreases, which leads to decreasing the phonon number, i.e. to the relations $N_0 > \left(n_{A0} - n_{M0}\right)/2 >> 1$.

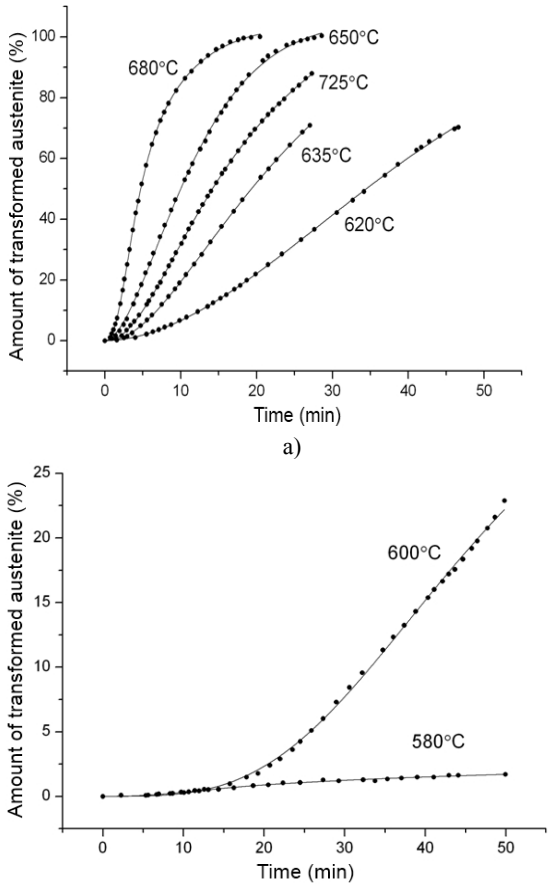


Fig. 2. *Comparison of digitized experimental data (points) with analytical solutions (8) (solid lines) for different temperatures of isothermic DMT of steel* $Fe + 7\%Cr + 2\%Ni$

a) Amount of transformed austenite (%);
b) Time (min)

Table 1. The values of A, B, C, k coefficients and characteristic time t^*_{AM} of isothermic DMT for different quench temperature

	Quench temperature, T^*_{H} (°C)						
	580 *	600*	620*	635	650	680	725
A	2.51	525.61	104.41	167.51	106.07	104.3	130.94
B	0.02	9.3E-4	0.45	0.02	0.15	0.17	4.1E-2
C	0.02	1.53E-4	2E-3	0.05	8.8E-3	0.16	6.8E-2
k	1.73	2.53	0.87	1.21	0.81	1.545	1.21
t^*_{AM}	10.60	33.6	$1.3 \cdot 10^3$	11.51	20.18	3.3	9.2

* The experimental data are insufficient for approximation.

Besides, it is known from experiments, that as the temperature decreases from martensitic T_{K} to room temperature $T_{\text{Ком}}$, DMT is observed, as a result of which the amount of transformed austenite increases from 5% at $T^*_{\text{H}} = 450$ °C to 95% at $T^*_{\text{H}} = 300$ °C [2, 9]. In this case, the DMT characteristic time $\tilde{t}_{AM}$ is practically the same for the full temperature range and is short in comparison with DMT characteristic time at high temperatures t^*_{AM} ($t^*_{AM} >> \tilde{t}_{AM} \approx 1$ min.)

Under these conditions the expressions for a high-temperature isothermal DMT can be used to describe isothermic DMT at low temperatures, if only in the expression for γ we replace T_{K} by $T_{\text{Ком}}$ and t^*_{AM} by $\tilde{t}_{AM}$,the probability of the induced transitions μ' by μ'' which corresponds to the frequencies of induced transitions at low quench temperatures.

At that, because of a small number of phonons, the exponential summands in denominators of accurate solutions of equations (1) can not be omitted.

In view of the fact that the number of phonons is still large compared with the number of elementary cells in phase *A* and phase *M*, the athermal DMT process can also be represented as a number of transitions from one TLS to another.

In general, based on solutions for DMT in high-temperature range the expression for total amount of transformed austenite is valid:

$$\frac{n_M^{tot}(t)}{n_{A0}A} \approx \frac{1}{2}\frac{\left(1 - A\frac{\left(n_{A0} - n_{M0}\right)}{\left(n_{A0} + n_{M0}\right)} exp\left(-2\mu'' N_{eq} t\right)\right)}{1 - \frac{n_{A0} - n_{M0}}{2N_0} exp\left(-2\mu'' N_{eq} t\right)}, \qquad (9)$$

If martensite formed in high-temperature range is excluded in (9), the amount of transformed austenite in low-temperature range will be equal to:

$$n_M(t) = n_M^{tot}(t) - n_{M0} = \frac{\frac{\left(n_{A0} - n_{M0}\right)}{2}\left(1 - exp\left(-2\mu'' N_{eq} t\right)\right)}{1 - \frac{n_{A0} - n_{M0}}{2N_0} exp\left(-2\mu'' N_{eq} t\right)}. \qquad (10)$$

With a relatively small number of phonons it can be shown that the amount of transformed phase *A* can be represented with a sufficient degree of accuracy by the sum of two solutions of the form (10).

In dimensionless notation the amount of transformed phase *A* can be represented as a sum of constant magnitude and two exponents:

$$\frac{n_{MS}(t)}{n_{A0}} = A' - B' exp\left(-Bt\right) - C' exp\left(-Dt\right), \qquad (11)$$

were, $A' = 100\left(1 - \frac{n_{M0}}{n_{A0}} - \frac{n'_{M0}}{n_{A0}}\right)$, $B' = 100\left(1 - \frac{n_{M0}}{n_{A0}}\right)A$, $C' = 100\left(1 - \frac{n_{M0}}{n_{A0}}\right)C$.

The theoretical dependence (11) was used to interpret experimental data according to isothermic DMT within low-temperature range [2].

The points obtained by digitizing the experimental data are shown by marks in Fig. 3. Solid lines depict the corresponding curves obtained from (11) at the values of coefficients given in Table 2.

The obtained analytical dependence (11) includes five constant coefficients, the values of which depend on the transformation temperature and are determined by experiment.

Comparison of analytical dependencies describing the isothermal DMT with the experimental data of the same process for one of the types of alloyed steel shows good quantitative agreement. The obtained agreement indicates the possibility of using DMT model based on the principle of detailed balance in alloy steels within a low-temperature range.

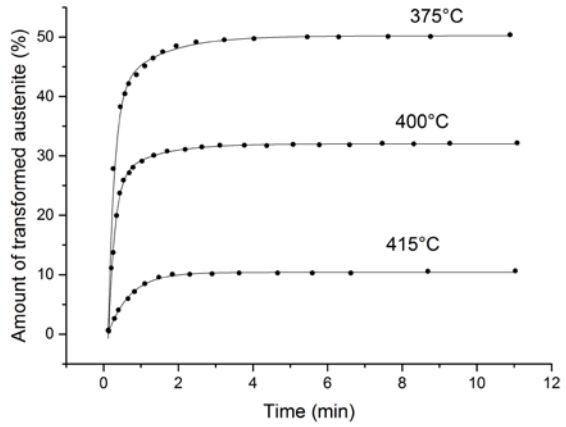


***Fig. 3**. Isothermal DMT in low-temperature range*

a) Amount of transformed austenite (%);
b) Time (min)

Table 2. The values of coefficients of curves (11) describing the experimental data [2].

°C	A'	B'	B	C'	D
415	10.39448	12.54669	1.67272	0	0
400	32.02108	6.86054	0.93142	59.43278	6.12407
375	50.19302	85.35374	6.10650	11.05937	0.83587

7. Conclusion

The paper analyzes the existing approaches in describing phase transitions in crystalline lattices of solids starting with the phenomenological paper of Landau and ending with publications of Kolmogorov and Avrami on nucleation and growth of a new phase. By the example of phase transformations of carbon and alloy steels it is noted that the proposed theories do not always give theoretical diagrams of austenite decay kinetics that are in good agreement with the experimental data. To eliminate the noted drawbacks in the existing theories it is proposed in this paper to describe the phase transformations of carbon steels on the basis of the principle of detailed balance formulated first by Einstein. On the basis of the approach proposed in this paper a system of equations has been obtained that describes both athermal and isothermal direct martensitic transformations of carbon steels.

In high-temperature range $T_{\text{K}} \le T\left(t\right) \le T_{\text{H}}^{*}$ and at a large number of phonons due to such a temperature the DMT process can be represented in the form of a large number of TLSs with a short transition characteristic time ($\mu' t_{AM} >> 1$). In each of these TLSs a phase *M* is formed in such a way that the final state of one TLS determines the initial state of the next one. The total amount of the transformed phase *M* is obtained as a result of summing the phase *M* in each TLS to which the temperature interval of the DMT is divided.

The analytical dependences obtained from the initial equations include four constant coefficients, the values of which depend on the transformation temperature and are determined by experiment. Comparison of analytical dependencies describing the isothermal DMT with experimental data of the same process for one of the types of alloy steel ($Fe+7\%Cr+2\%Ni$) shows their good quantitative agreement. Such a quantitative agreement indicates the possibility of using DMT model based on the principle of detailed balance in alloy steels within a high-temperature range.

It was concluded on basis of the obtained analytical solutions that within a high-temperature range DMT occurs in alloy steel with decreasing temperature from initial $T = T_{\text{H}}^{*} \le T_{\text{H}}$ to $T = T_{\text{K}}$, as a result of which the elementary lattice cells of phase *A* almost completely transit to phase *M*.

The analytical dependences of isothermal DMT of alloy steels in a low-temperature range ($T_{\text{Ком}} \le T\left(t\right) \le T_{\text{H}}^{*} \le T_{\text{K}}$), when a small number of phonons are realized ($N_0 > \left(n_{A0} - n_{M0}\right)/2 >> 1$), can be represented as a sum of three summands: a constant summand and two decreasing in time exponents, each of which has its own constant factor and its characteristic time value. The values of the constant summand, two constant factors and two characteristic times (only five constants) depend on the transformation temperature and are determined by experiment. Comparison of analytical dependencies describing the isothermic DMT of one of the alloy steel types with the experimental data in low-temperature range shows a good quantitative agreement. Such an agreement indicates the possibility of using DMT model of alloy steels based on the principle of detailed balance in a low-temperature range.

I want to express my gratitude to Tkachenko Viktor Ivanovich for his interest in this work and valuable comments.

References

1. Landau, L.D. K teorii fazovykh perekhodov. - ZHETF, T. 7, 1937, p. 19 - 32. L,ll
2. Kurdyumov, G.V. Yavleniya zakalki i otpuska stali. M.: Metallurgizdat. 1960. 64 p.
3. Koval', Yu.N. Deformatsionnyye i relaksatsionnie yavleniya pri prevrashcheniyakh martensitnogo tipa. K.: Naukova Dumka, 2010. 288 p. (Koval' Yu.N., Lobodyuk V.A.).
4. Estrin, E.I. Ustoychivost' reshetki i martensitnie prevrashcheniya. - V kn. Martensitnie prevrashcheniya. K.: Nauk. dumka, 1980. 29 p.
5. Kolmogorov, A.N. K statisticheskoy teorii kristallizatsii metallov. - Izv. AN SSSR. Ser. matem. T. 1. Vyp. 3. 1937. p. 355–359.
6. Kristian, Dzh. Teoriya prevrashcheniy v metallakh. Ch. 1. Termodinamika i obshchaya kineticheskaya teoriya. - M.: Mir. 1978. 806 p.
7. Eynshteyn, A. K kvantovoy teorii izlucheniya. - UFN. T. 86, Vyp. 3. 1965. P. 371-381.
8. Gulyayev, A.P. Metallovedenie. Uchebnik dlya vuzov. 6-e izd., pererab. i dop. - M.: Metallurgiya. 1986. 544 p.
9. Kogan, L.I. O kinetike polimorfnogo prevrashcheniya legirovannogo zheleza: v sb. "Problemy metallovedeniya i fiziki metallov". - M.: Metallurgizdat. T. 2. 1951. p. 204 - 215. (Kogan L.I., Entin R.I.).

EFFECT OF LOW-FREQUENCY VIBRATION ON THE STRUCTURE AND RESIDUAL STRESSES IN SLM Ti-6Al-4V ALLOY

ВЛИЯНИЕ НИЗКО-ЧАСТОТНОЙ ВИБРАЦИИ НА СТРУКТУРУ И ОСТАТОЧНЫЕ НАПРЯЖЕНИЯ В СЛС TI-6AL-4V СПЛАВЕ

Kazantseva N.[1], Rumyantsev S.[2] Fefelov A.[3], Merkushev A.[3], Ezhov I.[1], Vinogradova N..[1] Davydov D.[1]
M.N. Miheev Institute of Metal Physics of Ural Branch of Russian Academy of Sciences, Ekaterinburg, Russia [1]
Ural State University of railway transport, Ekaterinburg, Russia[2]
Regional Engineering Center of laser and additive technology, Ural Federal University, Ekaterinburg, Russia [3]

Abstract: *The effect of the low-frequency vibration processing on the residual elastic stresses in the Ti-6Al-4V alloy manufactured by 3D printing (Selective laser melting) was investigated. The studied sample was manufactured horizontally in respect to the building platform. Different vibration oscillations modes (vertical, horizontal, and elliptical) were chosen for study. The oscillations were done with frequency of 16 Hz, and a processing time was 20 minutes. Studies shown that 3D printed sample had a high level of residual elastic stresses, which were changed after vibration treatment. The optimal parameters of vibration processing, which provide a minimum level of residual elastic stresses in 3D printed Ti-6Al-4V alloy are discussed.*
***KEYWORDS**: TITANIUM ALLOY, SLM, 3D PRINTING, MICROSTRUCTURE, RESIDUAL STRESSES*

1. Introduction

Analysis of the residual stresses is one of the important tasks solved in the design of metallic parts and constructions. Residual stresses can have both the negative and positive effects on the structure of the materials. In many cases, the decrease in the level of residual stresses in the critical parts of the metal constructions leads to the increase of their reliability and durability. Most impact of the residual internal stresses is found to be associated with the limitation of exploitation capacity of the material under cyclic loads, small plasticity of the material, or at low temperatures [1]. Residual stresses are present in the material, regardless of the presence or absence of external influences. They arise because of local plastic deformations from non-uniform heating, local external mechanical action, local structural-phase changes.

Vibration treatment has been successfully used for several years in the oil and gas industry for decreasing of the residual internal stresses in the welded joints [2]. This process is provided with the fact, that in the case of resonant vibration, high dynamic stress amplitudes appear in the structure of the metal, which significantly affect the redistribution of stresses in the entire volume of the material. It was found that the vibration processing of titanium alloys allowed one to reduce the residual internal stresses up to 60%. As it is also shown, the necessary frequency for such vibration processing of metals should be not less than 50 Hz [3].

High level of the residual elastic internal stresses was found in the Ti-6Al-4V alloys manufactured by selective laser melting [4]. Tensile twins given an evidence of the existence of the high level of the tensile stresses in the 3D printed Ti-6Al-4V material were observed in [5].

The aim of this work is to study the possibility of using the vibration treatment with decreased frequency to change the level of residual stresses in the Ti-6Al-4V alloy manufactured by the 3D printing.

2. Experimental procedure

Ti-6Al-4V samples were manufactured by 3D printing using the selective laser melting (SLM) with the EOSINT M280 (EOS GmbH) 3D printing machine equipped with an Ytterbium fiber laser, and operating at 1075 nm wavelength (IPG Photonics Corp.). Standard regime for manufacturing of the titanium alloys was used. The chemical composition of a powder corresponded to the ASTM B348 standard for medical titanium alloy (grade 23). Structural studies were done with the transmission electron microscopes JEM 200CX and Tecnai G2 30 Twin with scanning systems and energy dispersive spectrometer EDAX, GATAN-filter image. Mechanical properties were measured at room temperature with nanoindentor NanoTest; the load F = 32 mN, load time was 10 s, and the measurement error was 2 %. Vibration tests were done with the laboratory-training stand for assessing the impact of vibration on railway products. The vibration frequency was 16 Hz. Three consecutive oscillation modes (vertical, horizontal, and elliptical) were applied; a processing time was 20 minutes. The test modes were set from a personal computer with licensed software. An X-ray diffractometer DRON-3 with Cu K_α radiation was used in this study. A sample cut from a bar of industrial medical hot-rolled and hot-pressed medical Ti-6Al-4V (ELI) alloy (ASTM F136, Grade 5) was taken as a reference [6]. Residual internal stresses leading to a shift in the X-ray lines were calculated from the formula [7]: $\sigma_1 + \sigma_2 = -\frac{E}{\nu} \cdot \frac{\Delta d}{d}$, where E is Young's modulus, ν is Poisson's ratio (ν = 0.3 for Ti-6Al-4V), d is interplanar distance. Residual surface stresses were calculated from the following formula [8]: H_{IT} - $H_{IT,0}$, where $H_{IT,0}$ is the hardness of the reference sample, obtained with nanoidentor.

3. Results and discussion

TEM results are presented in Figures 1-4. Figure 1 presents the structure of the reference sample. Two-phase structure with plates of the HCP α-phase and grains of retained BCC β-phase can be observed in this sample (Fig.1a). SAED pattern taken from this region contains the reflexes of HCP and BCC phase in positions corresponding to the relationships between BCC and HCP crystal lattices (Fig.1b).

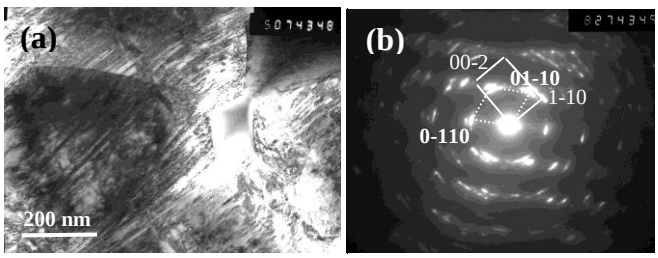


***Fig. 1.** Microstructure of the reference sample: (a) the bright-field image; (b) SAED pattern to (a), zone axis $[0001]_{HCP}$ // $[110]_{BCC}$*

High cooling rates at SLM method result in the formation of the acicular α´ martensitic phase in Ti-6Al-4V (Fig.2a-b). Thin twins are observed in the structure of the as-build sample (Fig.2c). The twin plane is corresponds to the tensile HCP {10-12} twin plane (Fig.2 d). The twinned structure with the same twin plane is

also observed in the sample after vibration (Fig.3a-c). High density of the defects one can see inside the HCP plates (Fig.3c).

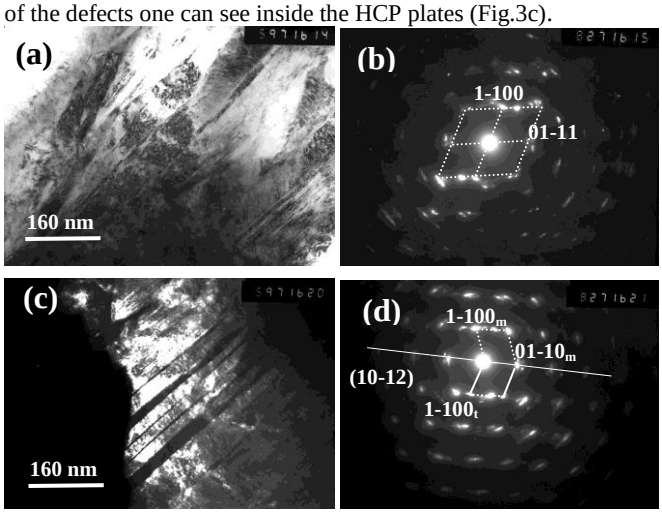


Fig. 2. *Microstructure of the as-build sample: (a) the bright-field image; (b) SAED pattern to (a), zone axis [01-11]$_{HCP}$; (c) the dark-field image taken in HCP twin reflex; (d) SAED pattern to (c), zone axis [0001]$_{HCP}$, (10-12) twin plane*

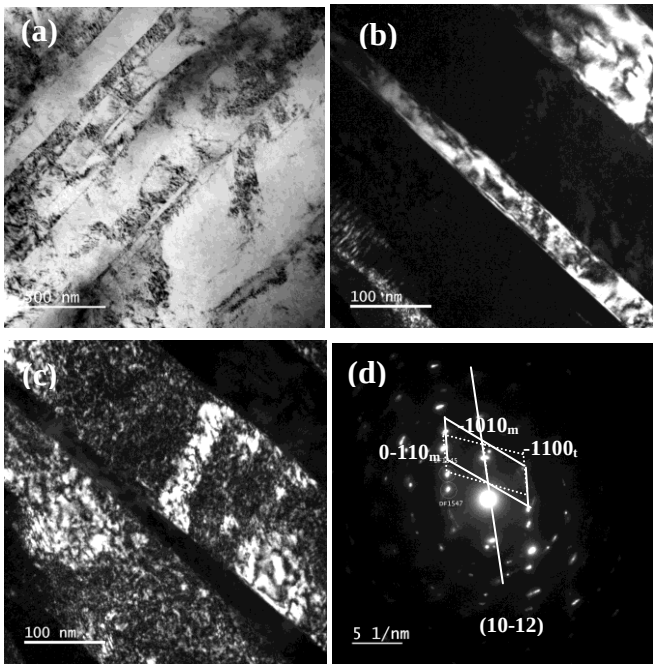


Fig. 3. *Microstructure of the as-build sample: (a) the bright-field image; (b) the dark-field image taken in HCP twin reflex; (c) the dark-field image taken in matric reflex; (d) SAED pattern to (c), zone axis [0001]$_{HCP}$, (10-12) twin plane*

We did not found the recrystallization grains in the sample after vibration, which could testify the occurring the relaxation process in the structure. The β-phase regions with high defect density were also found in this sample (Fig.4).

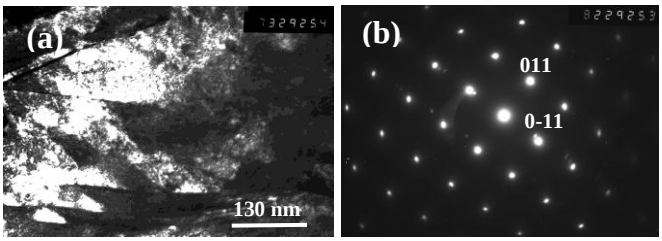


Fig.4. *BCC region in the sample after vibration: (a) the dark field image taken in (0-11)$_{BCC}$ reflex; (b) SAED pattern to (a), zona axis [100]$_{BCC}$*

According to X-ray analysis BCC phase is present in both samples the as-build and after vibration (Fig.5). However, in as-build sample almost all BCC diffraction lines coincide with HCP diffraction lines (Fig.5a). In TEM pictures, we did not found the BCC regions in the as-build sample. Probably, it is associated with the small and local presence of BCC phase in the structure of the as-build sample. After vibration the intensity of the BCC diffraction lines are higher than that in the as-build sample (Fig.5b). Last fact means that the vibration promotes the phase transformation $\alpha' \rightarrow \beta$.

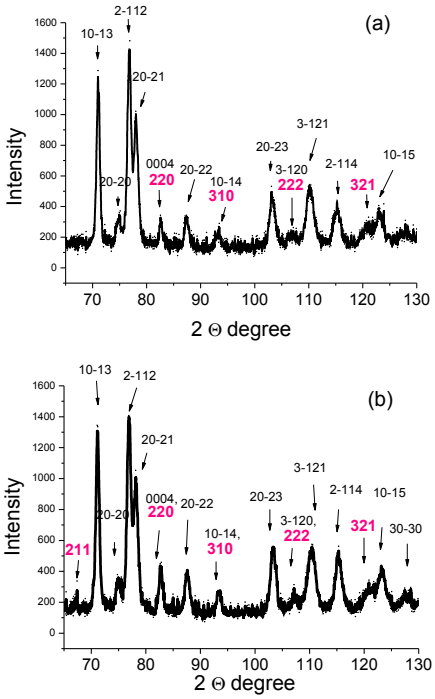


Fig.5. X-ray results of the studied samples: (a) as-build; (b) after vibration

Results of nanoidentation and X-ray analysis are presented in Table 1.

Table 1: *Results of nanoidentation*

Sample	E_{IT}, GPa	H_{IT}, GPa	Residual internal stresses (MPa)	Residual surface stresses (MPa)
reference	132	5.3	-	-
As-build	174	5.6	189	300
after vibration	177	5.9	458	600

As can be seen from the Table 1, the high level of the tensile internal stresses is found in the as-build sample. The results of X-ray and nanoidentation are correlates with each other. After vibration, the level of the residual elastic stresses is increased in comparison with that in as-build sample. In contrast to surface hardening treatments, vibration acts in the same way on both the internal and surface residual stresses.

Conclusion

Thus, low-frequency vibration used in this study affects the structure, phase composition and residual elastic stresses of the 3D printed sample. These results are promising for a possibility of using low-frequency vibration processing for titanium products manufactured by 3D printing. It is known that surface of the titanium products needs to be cleaned after every heat treatment. Low frequency vibration treatment is a non-expensive method, which allows one to save the material.

Effect of vibration exposure depends on not only the frequency, but also the amplitude and shape of the oscillations.

Thus, by changing the modes of oscillation and the time of action, it is possible to select the optimal parameters for the relaxation process, which would promote the decreasing of the residual elastic stresses.

Acknowledgments

This work was supported by Russian Found of Basic Research [№ 17-03-00084] and State programs "Diagnostics" [№ AAAA-A18-118020690196-3]. The structural study and mechanical tests were done in the collective centers of the Institute of Metal Physics, Ural Division of Russian Academy of Sciences.

References

1. Birger I. A. Residual stresses, – M., Mashgiz, 1963, 233 p. (in Russian)
2. Gilmanshin R. A., Erofeev V. V., Sharafiev R. G., Yakupov V. M. Effect of vibration treatment on the level of residual stresses and mechanical characteristics of welded joints // Oil and gas business. Machines and devices. 2015. 13 (4). p. 185-192.
3. Lashchenko G. I. Technological opportunities of vibration processing of welded structures (Review) // Automatic welding. 2016. 754 (7). p.28-34.
4. Yadroitsev I., Yadroitsava I. Evaluation of residual stress in stainless steel 316L and Ti6Al4V samples produced by selective laser melting // Virtual and Physical Prototyping. 2015. 10(2). p. 67-76.
5. Krakhmalev P., Fredriksson G., Yadroitsava I., Kazantseva N., du Plessis A., Yadroitsev I. Deformation Behavior and Microstructure of Ti6Al4V Manufactured by SLM // Physics Procedia. 2016. 83. p. 778-788.
6. http://www.yunchtitanium.com/ti-round-bar
7. Gorelik S. S, Rastorguev L. N, Skakov Yu. A. X-ray and electron-optical analysis, – M, Metallurgy, 1970.
8. GOST R 57172-2016 "Definition of surface residual stresses by the indentiation method", – M. Standardinform, 2016 (in Russian).

MANUFACTURING OF IONIZING RADIATION SOURCE OF IRUDIUM-192 FOR GAMMA-DEFECTOSCOPES OF GAMMARID-192/120M

Dr. Ashrapov U.T.[1], Dr. Khujaev S.S.[1], Dr. Khalikov U.A.[1], Eng. Isaev Y.A.[2]
Institute of Nuclear Physics[1], Tashkent, Republic of Uzbekistan, ashrapov@inp.uz, khujaev@inp.uz, khalikov@inp.uz
«VBM Engineering» Co., Ltd.[2], Tashkent, Republic of Uzbekistan, y.isaev@vbm.uz

Abstract: *The paper presents research on the development of ionizing radiation source of iridium-192 for gamma-ray flaw detector. Nuclear-physical processes of neutron activation of natural iridium on a nuclear reactor have been studied.*
Iridium disks were irradiated with neutrons of the VVR-SM reactor, radiochemical methods were used to reprocess iridium disks, hermetic sources of Iridium-192 were manufactured,
The iridium-192 source was placed in the source holder and equipped with gamma-defectoscope (gamma-ray flaw detector) of Gammarid-192/120M.
With a gamma-ray flaw detector with iridium-192 source, non-destructive testing of welded pipeline seam was carried out.
X-ray photographs of non-destructive testing of welded seams were obtained, according to the sensitivity, which meet the requirements of the GOST-7512-82 «Control nondestructive control. Connections welded. Radiographic method».
KEYWORDS: *NATURAL IRIDIUM, NUCLEAR REACTOR, NEUTRON- IRRADIATION, IRIDIUM-192 RADIONUCLIDE, IONIZING RADIATION SOURCE, GAMMA-RAY FLAW DETECTOR, NONDESTRUCTIVE TESTING, X-RAY IMAGE.*

Introduction

Gamma-ray flaw detectors of Gammarid-192/120M complete with iridium-192 ionizing radiation source are universal portable hose devices designed for radiographic quality control of products with different manufacturing techniques (cast, welded, forged, pressed and others) without their destruction [1].

The effective operation of the gamma flaw detector of Gammarid-192/120M depends on the timely charging of the gamma flaw detector by the iridium-192 source of necessary activity.

At the Institute of Nuclear Physics, work was done on the production of Iridium-192 sources with an 80-120 Curie activity and their charging into the radiation head of a gamma-ray flaw detector of Gammarid-192/120M.

Preconditions and means for the decision of problem

For the production of iridium-192 with a high specific activity (≥250 Ci/g Ir)on the VVR-SM reactor, studies were carried out: thermal neutron fluxes density in vertical channels of the reactor, the output of the induced radionuclide iridium-192 activity; cadmium ratios of radionuclide iridium-192; the influence of the thickness of the iridium disk on the yield of iridium-192 activity.

For local monitoring of the thermal neutron flux density, a thermo-neutron sensor TND-2,0 [2]was used, which operates in the range from $5.\cdot10^{12}$ neutron/sm^{2}s to 5.10^{12} neutron/sm^{2}s.

Cadmium monitors in form of metal disks (∅=3mm, h=0,2mm, m=3,0mg) made from an alloy of aluminum and cobalt (0,1%) packed with cadmium cover (h=1,0 mm) and without cadmium cover were used to determine cadmium ratios.

Activity of monitors cobalt-60 and radionuclide iridium-192 were measured by spectrometric equipment: multichannel analyzer of impulses SU-01P with Ge-Li detector DGDK-100 with the program «Aspekt, Angamma» and multichannel gamma-spectrometer DSA 1000 «Canberra HP» with Ge detector GC with standard software package Genie 2000.

For the production of Iridium-192 sources, the following installations were designed and manufactured: installation for radiochemical processing of neutron irradiated iridium disks, installation for the production of iridium-192 sources and their sealing, equipment for placing the Iridium-192 source in the holder and rolling the holder from the sources.

Decision of considered problem

The metal iridium disks (diameter - 3,0 mm, thickness - 0,2 mm, weight - 31,7 mg) were packed in aluminum foil and placed in a block-container EC-10 (L=340 mm, ∅=25 mm) [3], which was loaded into a vertical channel of reactor, located in the internal cavity of the fuel assemble of IRT-4M.

Iridium disks were irradiated with neutrons in the following regime: reactor power 10 MW, the arrangement of iridium disks at a distance of 35-45 sm below the upper point of the reactor core, thermal neutron flux density is $\geq0,9\cdot10^{14}$ neutron/sm^2 sec, exposure time is 800÷1680 hours.

After irradiation iridium disks were removed from the packaging and and placed in a special device for radiochemical processing, where they were treated with a solution of alkali, water and dried.

Irradiated iridium disks were placed in a stainless steel capsule, and are provided with a lid and hermetically sealed with argon-arc welding. Verification of the tightness of the Iridium-192 source was carried out by the immersion method [4].

The iridium-192 source was placed in the holder, then cover is hermetically sealed with argon arc welding and the holder is connected to a flexible shaft of Gammarid-192/120M gamma-ray flaw detector.

Results and discussion

Natural iridium consists of two stable isotopes: Iridium-191 (38,5 %) and Iridium-193 (61,5 %) [5].

Irradiation of the iridium-191 reactor with neutrons leads to a rapid burn up of iridium-192 radionuclide by the resonant neutron flux (Table 1).

Table 1. The scheme of reception ^{192}Ir radionuclide and nuclear - physical characteristics of ^{192}Ir, ^{193} Ir, ^{194}Ir radionuclides [8].

Nuclear transition	Type of nuclear reaction	Cross sec-tion of active-tion, barn	Half -life per-iod	E_γ,МэВ
$^{191}Ir \rightarrow {}^{192}Ir$	(n,γ)	700	74,1 days	E_γ: 0,296; 0,308; 0,317; 0,468; 0,589; 0,604; 0,612. E_β:0,24; 0,54; 0,67.
$^{192}Ir \rightarrow {}^{192}Pt$	β^- (95%)	-	-	-
$^{192}Ir \rightarrow {}^{192}Os$	E.C. (5%)	-	-	-
$^{192}Ir \rightarrow {}^{193}Ir$	(n,γ)	700	-	-
$^{193}Ir \rightarrow {}^{194}Ir$	(n,γ)	130	17,4 hour	

It should be noted that during the formation of radionuclides iridium-193 and iridium-194, iridium-192 burns strongly and the yield of iridium-192 decreases.

The table 2 shows the potential differences obtained by a thermo-neutron sensor TND-2.

Table 2. Potential difference in vertical channels of the reactor VVR-SM.

Distance below the top of the vertical channel , sm	Number of the vertical channel					
	5-7	4-4	4-2	3-4	3-7	2
	mV	*mV*	*mV*	*mV*	*mV*	*mV*
10	8,0	11,1	10,3	10,0	10,0	6,0
15	10,2	11,1	14,2	11,1	12,6	8,0
20	13,7	14,1	18,5	13,9	16,4	10,4
25	16,2	17,1	22,0	16,7	19,8	12,1
30	18,4	19,8	25,3	19,2	22,1	13,5
35	20,0	21,3	27,0	20,5	23,8	14,1
40	21,1	22,0	28,6	21,2	25,0	14,1
45	20,0	22,0	28,0	21,0	24,4	14,1
50	18,6	21,0	25,8	20,0	23,0	13,0
55	16,0	18,8	23,0	19,0	20,0	12,0
60	15,5	15,2	22,0	16,4	19,9	11,6
65	13,2	13,0	15,4	14,2	16,2	10,2

It can be seen from the table 3 that the potential differences and, correspondingly, the neutron flux density have high values at a distance of 35-45 sm from the top point of the irradiation vertical channel of the reactor.

The yield of induced radionuclide iridium-192 activity depends on the thickness of iridium disk (Table 3).

Table 3. Influence of the yield of induced iridium-192 radionuclide activity on the thickness of the iridium disk.

Number of reactor vertical irradiation channel	Thickness of Ir disk, micron	Weight of Ir disk, g	Activity of Ir-192 in the iridium disk, Ci	Activity of Ir-192 at Ir disk weight $1\cdot10^{-5}$ g, Ci	Output of induced activity of Ir-192 radionuc-lide
2	0,5	$1,5\cdot10^{-5}$	$8,9\cdot10^{-6}$	$6,02\cdot10^{-6}$	1,0
	20	$4,7\cdot10^{-3}$	$9,1\cdot10^{-4}$	$1,93\cdot10^{-6}$	0,32
	60	$11,1\cdot10^{-3}$	$1,95\cdot10^{-3}$	$1,75\cdot10^{-6}$	0,29
	80	$19,7\cdot10^{-3}$	$2,69\cdot10^{-3}$	$1,36\cdot10^{-6}$	0,22
4-1	0,5	$1,5\cdot10^{-5}$	$2,6\cdot10^{-6}$	$1,75\cdot10^{-5}$	1,0
	20	$6,2\cdot10^{-3}$	$2,7\cdot10^{-3}$	$3,35\cdot10^{-6}$	0,19
	60	$13,1\cdot10^{-3}$	$5,05\cdot10^{-3}$	$2,91\cdot10^{-6}$	0,26
	80	$19,5\cdot10^{-3}$	$2,8\cdot10^{-3}$	$1,4\cdot10^{-6}$	0,23

It can be seen from the table 3 that the larger the thickness of the iridium disk, the less the yield of induced iridium-912 activity.

Table 2 gives the values of cadmium ratios for iridium-192.

Table 4. The values of cadmium ratios for iridium-192.

Irradiated sample	Weight of iridium sample , g	Number of the vertical channel	Activity of Iridium-192, Bq	Cadmium attitude, R_{Cd}
Iridium-191	$1,5\cdot10^{-5}$	2-6	$5,97\cdot10^{5}$	9,19
Iridium-191 + Cd cover	$1,5\cdot10^{-5}$	2-6	$2,66\cdot10^{4}$	
Iridium-191	$1,5\cdot10^{-5}$	4-1	$3,98\cdot10^{5}$	12,69
Iridium-191 + Cd cover	$1,5\cdot10^{-5}$	4-1	$3,13\cdot10^{4}$	
Iridium-191	$1,5\cdot10^{-5}$	2	$3,32\cdot10^{5}$	8,13
Iridium-191 + Cd cover	$1,5\cdot10^{-5}$	2	$1,67\cdot10^{4}$	

The iridium disk which has been wrapped up in cadmium cover is badly activated by thermal neutrons, as cadmium absorbs practically all thermal neutrons, as for cadmium, the thermal neutron absorption cross section is 2450 barn.

Resonant neutrons make a partial contribution to the yield of induced radionuclide activity of iridium-192, however, the yield of the induced iridium-192 radionuclide activity increases with the increase in the thermal neutron flux density.

Iridium wrapped in a cadmium cover is activated by resonant and thermal neutrons by the ratio:

$$R_{Cd}=a/a_p \quad (1)$$

where: R_{Cd} - cadmium attitude, a - activity of iridium without cadmium cover, a_{p-} activity of iridium with cadmium cover.

It follows from formula 1 that the larger the cadmium ratio, the smaller the fraction of resonant neutrons in the total neutron flux density [6].

The basic characteristics of pilot Iridium-192 source are given in table 5.

Table 5. The Iridium-192 source basic characteristics [7].

Name, characteristic and unit of measurement	Data
1. Working surface	bottom
2. The power of the exposure dose of the source measured by the method of direct measurements using a dosimeter of the type DKS-04, Ampere/kg	$3,2\cdot10^{-6}$
3. The power of the exposure dose of gamma radiation when the radiation head is charged with iridium-192 source at a distance of 50 mm from the surface of the radiation head with Iridium-192 source, Ampere /kg (milliroentgen/hour)	$2,39\cdot10^{-9}$ (40)
4. Confidence limits of the total error in the results of measuring the exposure dose rate of a source at a probability of 0,95, in %	±20
5. Date of exposure dose rate measurement	02/26/2016
6. Radionuclide activity of iridium-192 in the source, Bq, (Curie)	$2,96\cdot10^{12}$ (80)
7. External dimensions of the source, mm	∅ - 4,5 h – 8,0
8. Dimensions of active part of the source , mm	∅- 3,0 h – 4,5
9. Material of source capsule	stainless steel
10. Source tightness	hermetic capsule
11. The level of radioactive contamination of the source with radioactive substances when determined by the smear removal method , Bq, not more than	185

Figures 2 and 3 show x-ray photographs of nondestructive testing of welded joints of pipelines of various diameters, obtained by radionuclide iridium-192.

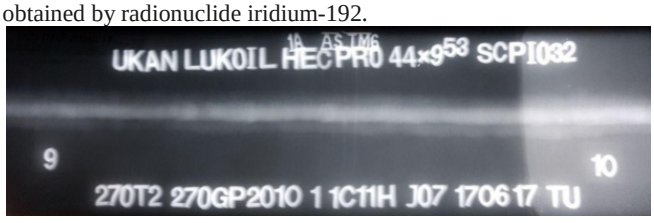


Figure 2. X-ray image of a welded pipeline of a diameter of 1120,0 mm obtained by gamma-ray flaw detector of Gammarid-192/120M with the iridium-192 source.



Figure 3. X-ray image of a welded pipeline of a diameter of 50,8 mm obtained by gamma-ray flaw detector of Gammarid-192/120M with the iridium-192 source.

The main results gamma radiography the test sample of the metal pipe, received gamma-ray flaw detector of Gammarid-192/120M with Iridium-192 source are shown in table 4.

Table 6. The main results of gamma radiography the test sample of the metal pipe.

Serial number of Gammarid-192/120M (source number of Iridium-192)	Radiation thickness of metal, mm	Expo-sure time, sec	The exposure dose rate on the surface of the radiation head with source, μSv/s	Sensitivity of the X-ray picture according to GOST 7512-82 (II class of sensitivity), mm	X-ray optical density
1128 (15)	20,0	25	0,083	0,4	2,0

Conclusion

Nuclear-physical processes of neutron activation of natural iridium on a nuclear reactor VVR-SM have been studied.

At the reactor neutron irradiation of natural iridium disks radionuclide iridium-192 with specific activity ~250 Ci/g Ir (up to 8 Ci for one iridium disk) was obtained.

The metal disks of natural iridium had been irradiated by thermal neutrons in vertical channel of VVR-SM reactor at reactor power 10 MW, thermal neutrons stream density is $0,9 \cdot 10^{14}$ neutron/sm^{2}s and irradiation time is 800÷1680 hours.

After irradiation of natural iridium disks they were advanced by radiochemical method and Iridium-192 sources are made. Argon arc welding and check of tightness of Iridium-192 source capsule have been spent.

The technological line on manufacturing tight Iridium-192 sources activity 80-120 Ci and their complete sets with gamma-ray flaw detector of Gammarid-192/120M have been created.

The Irtidium-192 source has been placed in holder with whom rolling, connection with flexible shaft and charge Iridium-192 source in radiating head gamma-ray flaw detector of Gammarid-192/120M are spent.

Nondestructive testing of metal pipes welded seams is spent and also x-ray pictures are received on sensitivity and quality, corresponding requirements of GOST-7512-82 «Control nondestructive control. Connections welded. Radiographic method» [8].

In the Republic Uzbekistan carrying out of teamwork with foreign partners under nondestructive testing over USA standards ASME on construction of the thermal power station, the gas-chemical plant and, the gas processing plant complex has obtained of international recognition and has shown efficiency of application of radiographic quality monitoring with gamma-ray flaw detector of Gammarid-192/120M completed with Iridium-192 sources.

References:

1.Gamma-defectoscope type of «Gammarid-192». The description and the maintenance instruction. Moscow. 1988. p.7;
2. P.G.Afanasev, T.B.Ashrapov, N.Abdusalamov, etc. Research Of Spatial Distribution of Thermal Neutrons Stream in Active Zones of Research Nuclear Reactors by Means of Small-sized Thermo-neutrone Gauges. IV All-Union Meeting on Metrology of Neutron Radiation on Reactors and Accelerators. Moscow, 1985. P.67-68;
3. Yuldashev B.S., Ashrapov T.B., Mirzaev N.M., Ashrapov U.T. Container for irradiation of samples in reactor. // Preliminary patent of Republic Uzbekistan # IDP04633. 2000;
4. Ashrapov U.T., Ergashev Kh.A., Makhkamov Sh.M.. Method of Leak Tightness Control of Ionization Radiation Source. Preliminary patent of Republic Uzbekistan. #4943.1997;
5. Levin V.I.Reception of radioactive isotopes//Moscow, Atomizdat. 1972. P. 25;
6. Levin V.E. The nuclear physics and nuclear reactors// Moscow, Atomizdat 1979. P.161;
7. Passport #15/14 for the Iridium-192 experimental source with Iridium-192 radionuclide.// Institute of Nuclear Physics of Academy Sciences of Republic Uzbekistan. Tashkent, 2014. p 4;
8. GOST--7512-82 «Control not destroying. Connections welded. Radiographic method ». Standards Publishing House // Moscow, 1982. p- 22.

COMPARATIVE INVESTIGATIONS OF THE MECHANICALLY ALLOYED and PRESSURELESS SINTERED Al–7 wt.% Si COMPOSITES REINFORCED WITH VARIOUS BORIDE PARTICLES

M.Sc. Mertdinç S.[1], M.Sc. Tekoğlu, E.[1], Dr. Ağaoğulları, D. [1], Prof. Dr. Öveçoğlu, M.L.[1]
Istanbul Technical University, Faculty of Chemical and Metallurgical Engineering, Department of Metallurgical and Materials Engineering, Particulate Materials Laboratories (PML), Ayazağa Campus, 34469 Maslak, Istanbul, Turkey[1]
mertdinc@itu.edu.tr

Abstract: *This study reports the milling time optimization of the Al-7 wt.% Si alloys by using planetary ball mill, the incorporation of 2 wt.% LaB_6, NbB_2, VB and TiB_2 particles into Al-7 wt.% Si matrix and the fabrication of composites using cold pressing and pressureless sintering. Mechanical alloying (MA) time carried out for 4, 8, 12, 16 and 20 h was optimized via crystallite size and phase determinations and microstructural investigations. 12 h was chosen as optimum MA time. Then, different particulate reinforcements were added to Al-7 wt.% Si matrix to constitute boride reinforced composites. All composite powder batches were also milled for 12 h, then compacted and sintered at 570°C for 5 h. Microstructural, physical and mechanical (hardness and wear volume loss) properties of these composites were performed. Hardness values of 120.8 ± 11.37 and 121.77 ± 19.02 were obtained for the LaB_6 and TiB_2 reinforced composites, respectively.*

Keywords: ALUMINIUM BASED COMPOSITES, PARTICULATE REINFORCEMENT, SINTERING, MICROSTRUCTURE

1. Introduction

Nowadays, metal matrix composites (MMCs) have wide range of application areas like aviation, defense and automotive [1–3]. Strength to weight ratio is an important parameter to improve the MMCs, so light metals are reinforced with ceramic particles that enable high strength to improve the properties of matrix metals or alloys [1,2,4,5]. Among the light-weight metals, Al-Si alloys draw a considerable interest due to their low density, low thermal expansion, high wear resistance, high stiffness, high corrosion resistances and good formability [3,6–8].

Although Al based composites were always produced with liquid-state production techniques, it is possible to produce this composites with solid-state processes [9,10]. Wettability of the reinforcement materials in the Al matrix is generally poor, so high energy milling can be used to produce homogeneous microstructures [10]. SPEX shaker mill, attritor ball mill, planetary ball mill, tumbler ball mill, vibratory ball mill are some types of mills that used for mechanical alloying (MA) in solid-state processes [10,11]. Amongst them, planetary ball mill is utilized for production of the milled powders in large quantities [11]. This is the main advantage of the planetary ball mill although SPEX shaker mill have 3 times higher rotation speed than that of planetary ball mill [11]. During the MA, powder particles are fractured, cold welded, fractured again and rewelded at high energy ball mill media. Therefore, powder particles are work hardened, particle sizes refine and composition homogeneity is achieved [11].

Up to now, aluminides, nitrides, carbides, oxides and borides were used as reinforcements for Al based MMCs due to their superior mechanical properties [12]. In this work, planetary ball mill were used for mechanical alloying and homogeneous dispersion of the reinforcement materials into the Al-7 wt.% Si matrix. LaB_6, NbB_2, VB and TiB_2 were chosen as reinforcement particulate materials for these experiments. Also, various boride reinforced Al-7 wt.% Si powders were milled for constant time, and they were pressed and sintered to produce boride reinforced composites. Mechanical, physical and microstructural properties of the boride reinforced composites were characterized.

2. Experimental Procedure

Al (Alfa Aesar™, 99.5 % purity, particle size ≤ 12 μm), Si (Alfa Aesar™, 99.99 % purity, particle size ≤ 20 μm), LaB_6 (Alfa Aesar™, 99 % purity, particle size ≤ 44 μm), NbB_2 (Alfa Aesar™, 99 % purity, particle size ≤ 44 μm), VB (Alfa Aesar™, 99 % purity, particle size ≤ 44 μm) and TiB_2 (Alfa Aesar™, 99 % purity, particle size ≤ 44 μm) powders were used as raw materials in the present study. As-blended Al-7 wt.% Si powders that were named as Al7Si were mechanically alloyed for 4, 8, 12, 16 and 20 h using a FRITSCH™ (400 rpm) planetary ball mill. Hardened steel vials (500 ml) and balls (ϕ 6 mm) were used, and ball-to-powder weight ratio was chosen as 7/1. Vials filled with powder batches were sealed inside a Plaslabs™ glove box (under Ar gas supplied by Linde™ with 99.999 % purity) to prevent the oxidation. MA'd powders were characterized by Bruker™ D8 Advanced Series X-ray diffractometer (XRD) with CuK_α (λ=1.5406 Å) radiation, 35 kV and 40 mA operating conditions to determine the crystalline phases. Also, Bruker™-AXS TOPAS 4.2 software was used to crystallite size and lattice deformation calculations. Then, morphologies of the powders were characterized via JEOL™ JCM-6000Plus NeoScope scanning electron microscope (SEM) coupled with energy dispersive spectroscopy (EDS).

After the morphological characterizations, optimum MA time was determined and 2 wt.% different types of boride reinforcements (LaB_6, NbB_2, VB and TiB_2) were added into Al7Si matrix one by one. 12 h MA'd powders were compacted using a MSE™ MP-0710 one-action hydraulic press under 450 MPa uniaxial pressure. Each compacted sample was debinded in a Protherm™ tube furnace under Ar gas flow at 420°C for 2 h with 2°C/min heating and cooling rate. Debinded bodies were sintered at 570°C in a Linn™ HT-1800 furnace under inert Ar atmosphere for 5 h (heating and cooling rate was 10°C/min).

Microstructural characterizations of the sintered samples were carried out using XRD and SEM. Density measurements of the sintered compacts were carried out using Archimedes method. Then, Vickers microhardness tests were conducted on the sintered samples using a Shimadzu™ HMV microhardness tester under a load of 25 g for 10 s. Result for each sample is the arithmetic mean of 10 successive indentations and standard deviations. Wear tests were carried out Tribotechnic™ oscillating tribotester by using 100Cr6 steel balls (6 mm), 3 N applied force, 5 mm/s sliding speed and 25,000 mm total sliding distance. Morphologies of the worn surfaces were examined with SEM. Besides, compression tests were performed to determine the compression strength, yield strength and strain at Shimadzu™ Autograph AGS-J at loading rate of 0.18 mm/min.

3. Results and Discussion

First of all, Al7Si matrix alloy was MA'd for different durations, and phase and morphology investigations were conducted to determine the optimum MA duration. Fig. 1(a)-(e) show the XRD patterns of the Al7Si powders MA'd with different durations (4, 8, 12, 16 and 20 h). XRD patterns of the powders displayed only the Al and Si phases. Intermetallic phase formation and contamination

were not detected in the powders even after 20 h milling (within the detection sensitivity of the diffractometer).

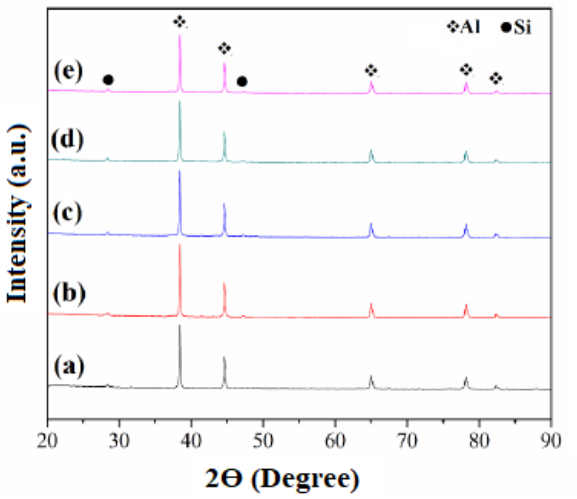


Fig. 1: *XRD patterns of the Al7Si powders MA'd for 4 h (a), 8 h (b), 12 h (c), 16 h (d) and 20 h (e).*

Calculated average crystallite sizes and average lattice deformations of the MA'd (for 4, 8, 12, 16 and 20 h) Al7Si powders are given at Table 1. Average crystallite sizes of the powders were reduced and their lattice strains were increased with increasing MA time. Because, plastic deformation during milling provided the lattice strain increment [13].

Table 2: *Average crystallite sizes and lattice deformations of the MA'd (for 4, 8, 12, 16 and 20 h) Al7Si powders.*

MA time [h]	Average crystallite size [nm]	Average lattice strain [%]
4	88.2	0.118
8	73.7	0.189
12	62.4	0.221
16	56.9	0.299
20	48.7	0.345

SEM micrographs of Al7Si powders MA'd for 4, 8, 12, 16 and 20 h are presented at Fig. 2 (a)-(e), respectively. 4 h MA'd powder get flattened due to the ball-to-powder collisions. Besides, 8 and 12 h MA'd powders have equiaxed and agglomerated particle morphologies. However, 16 and 20 h MA'd powders get flattened again. Moreover, flattened particles cause crack and porosity formation after pressing and sintering [11]. Therefore, optimum MA duration was selected as 12 h to obtain homogeneous particle size formation.

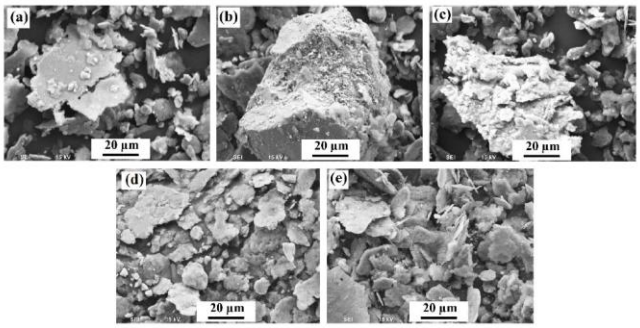


Fig. 2: *SEM micrographs of the Al7Si powders MA'd for 4 h (a), 8 h (b), 12 h (c), 16 h (d) and 20 h (e).*

After the MA time optimization, all different reinforcement particles were added to Al7Si and these blends were MA'd for 12 h to constitute Al7Si-2LaB_6, Al7Si-2NbB_2, Al7Si-2VB and Al7Si-2TiB_2 powders. Microstructural and phase characterizations were performed for the MA'd powders, then microstructural, physical and mechanical properties of the sintered bodies were characterized after pressing and sintering of these MA'd powders.

Fig. 3(a)-(d) show the XRD patterns of the Al7Si-2LaB_6, Al7Si-2NbB_2, Al7Si-2VB and Al7Si-2TiB_2 powders, respectively. Only Al, Si and boride phases were detected. There is not intermetallic phase formation between the Al, Si and reinforcement particles.

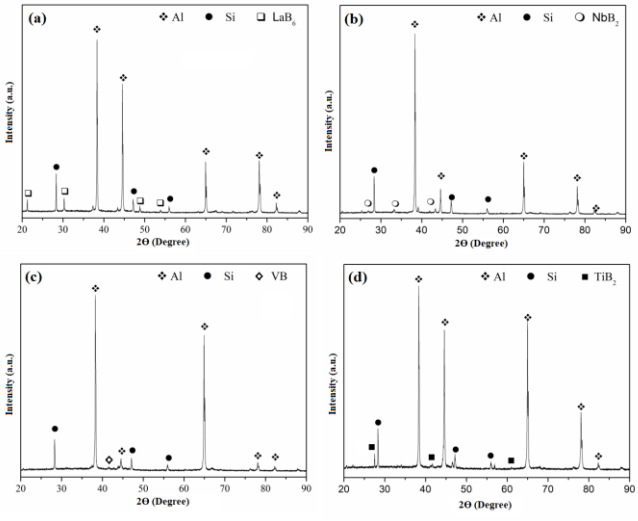


Fig. 3: *XRD patterns of the boride reinforced Al7Si powders MA'd for 12 h: Al7Si-2LaB_6 (a), Al7Si-2NbB_2 (b), Al7Si-2VB (c), Al7Si-2TiB_2 (d).*

SEM micrographs of the boride reinforced Al7Si powders MA'd for 12 h (Al7Si-2LaB_6, Al7Si-2NbB_2, Al7Si-2VB and Al7Si-2TiB_2 powders) are given in Fig. 4(a)-(d). Hard and brittle reinforcement particles caused the fracturing of the matrix material during milling. Flaky shaped particles were seen in Fig. 4 for all reinforced powders. However, the fracturing is seen obviously in the NbB_2 and TiB_2 reinforced powders (Fig. 4(b) and (d)).

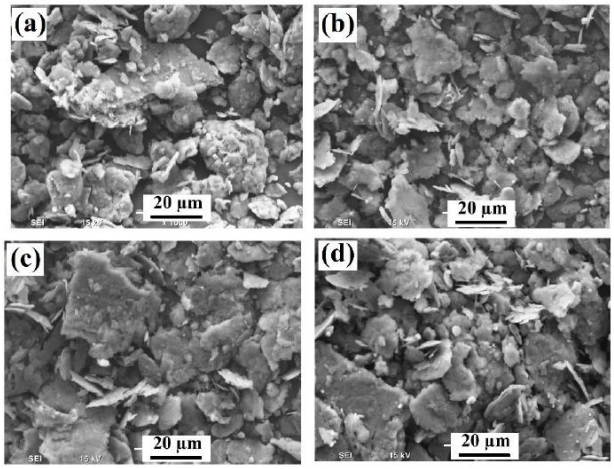


Fig. 4: *SEM micrographs the boride reinforced Al7Si powders MA'd for 12 h: Al7Si-2LaB_6 (a), Al7Si-2NbB_2 (b), Al7Si-2VB (c), Al7Si-2TiB_2.*

Each powder was compacted and sintered. After that, microstructural, physical and mechanical properties of the sintered compacts were determined via characterization investigations and their results are explained below.

OM images of the sintered compacts are given in Fig. 5 (a)-(d) for Al7Si-2LaB_6, Al7Si-2NbB_2, Al7Si-2VB and Al7Si-2TiB_2 samples. Si (dark regions) distributed homogeneously into the Al matrix. Also, particulate reinforcements distributed homogeneously via MA.

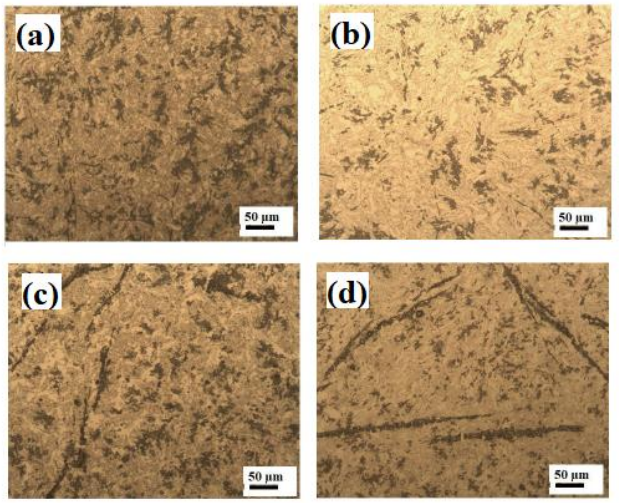


Fig. 5: *OM images of the sintered boride reinforced Al7Si samples: Al7Si-2LaB_6 (a), Al7Si-2NbB_2 (b), Al7Si-2VB (c), Al7Si-2TiB_2 (d).*

Theoretical density and Archimedes density results are presented at Table 2. The highest relative density value was reached with LaB_6 reinforcement and the lowest relative density value was obtained with TiB_2 reinforcement. Densities of the samples related with the interfacial area between the reinforcement and matrix material. If the reinforcement particles inhibit the diffusion during solid-state sintering, lower densities enabled than the theoretical densities [8]. Otherwise, densities of the reinforced samples are low due to the flaky shaped morphologies of the milled powders. These flaky microstructures affect negatively the compaction and dense bodies were not produced.

Table 2: *Density measurements of the sintered samples.*

Sample	Theoretical Density (g/cm^3)	Archimedes Density (g/cm^3)	Relative Density (g/cm^3)
Al7Si	2.672	2.62	88.18
Al7Si-2LaB_6	2.690	2.66	88.90
Al7Si-2NbB_2	2.672	2.65	87.96
Al7Si-2VB	2.696	2.64	87.89
Al7Si-2TiB_2	2.692	2.58	86.01

Table 3 shows the average Vickers microhardness results taken from the 10 successful indentations for each sample. Hardness of the MA'd and sintered composites with various reinforcements are higher than the hardness of the MA'd and sintered Al-Si matrix alloy. The Vickers microhardness value of the VB reinforced composite is the highest value amongst all samples. Besides, wear volume tests were conducted for all reinforced samples. VB reinforced composite has the lowest wear volume loss. Therefore, VB reinforcement improve the wear resistance and microhardness of the matrix.

Table 3: *Microhardness measurements and wear volume losses of the sintered samples.*

Sample	Vickers Microhardness (HV)	Standard Deviation	Wear volume loss (mm^3)
Al7Si	104.7	±20.1	-
Al7Si-2LaB_6	120.8	±11.3	0.007
Al7Si-2NbB_2	114.9	±14.6	0.012
Al7Si-2VB	135	±28.4	0.005
Al7Si-2TiB_2	121.7	±19.0	0.010

Wear tracks of the Al7Si-2LaB_6, Al7Si-2NbB_2, Al7Si-2VB, Al7Si-2TiB_2 sintered compacts are presented in Fig. 6(a)-(d). Abrasive grooves were observed at these SEM images. Wear track of the Al7Si-2VB sample is the narrowest one. These wear track images are in good agreement with the wear volume loss results.

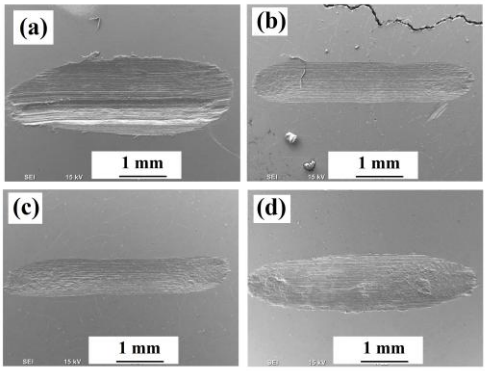


Fig. 6*: SEM images of the wear tracks taken from the sintered samples: Al7Si-2LaB_6 (a), Al7Si-2NbB_2 (b), Al7Si-2VB (c), Al7Si-2TiB_2.*

Compression strength, yield strength, elastic strain and strain of the all sintered samples are listed at Table 4. The highest yield strength was obtained for the TiB_2 reinforced composite whereas the highest compression strength was obtained for the LaB_6 reinforced one. Also, elastic strains of the composites were not high; this situation is probably arisen from the flaky shaped reinforced and milled powders. These types of hard and brittle reinforcements resulted in a weak bonding in the ductile matrix and mechanical properties were not found as so high.

Table 4: *Compression strength, yield strength, elastic strain and strain of the sintered samples.*

Sample	Yield Strength (MPa)	Compression Strength (MPa)	Elastic Strain (%)	Total Strain (%)
Al7Si-2LaB_6	103	164	0.37	2.18
Al7Si-2NbB_2	101	152	0.27	0.60
Al7Si-2VB	93	140	0.31	0.66
Al7Si-2TiB_2	119	142	0.42	0.68

4. Conclusion

In this study, effects of the various types of boride reinforcements into the Al7Si matrix were examined. The usage of the planetary ball mill in mechanical alloying applications was also investigated. Based on the characterization investigations, results can be summarized as below:

- Al7Si matrix powders were milled for different durations. Although, crystallite sizes reduced with increasing MA time, particles were started to be flattened after 12 h of MA. Therefore, optimum MA time was chosen as 12 h.
- Among the sintered samples, the highest relative density was obtained for the Al7Si-2LaB_6 sample
- Among the sintered samples, the highest hardness and wear resistance were obtained for the Al7Si-2VB sample. Besides, Al7Si-2TiB_2 composite has the highest yield strength.

References

[1] D. Garbiec, M. Jurczyk, N. Levintant-Zayonts, T. Mościcki, Properties of Al-Al<inf>2</inf>O<inf>3</inf> composites synthesized by spark plasma sintering method, Archives of Civil and Mechanical Engineering. 15 (2015) 933–939. doi:10.1016/j.acme.2015.02.004.

[2] M. Hossein-Zadeh, M. Razavi, M. Safa, A. Abdollahi, O. Mirzaee, Synthesis and structural evolution of vanadium carbide in nano scale during mechanical alloying, Journal

of King Saud University - Engineering Sciences. 28 (2016) 207–212. doi:10.1016/j.jksues.2014.03.010.

[3] S.Q. Wu, H.Z. Wang, S.C. Tjong, Mechanical and wear behavior of an Al/Si alloy metal-matrix composite reinforced with aluminosilicate fiber, Composites Science and Technology. 56 (1996) 1261–1270. doi:10.1016/S0266-3538(96)00085-1.

[4] A.K. Bodukuri, K. Eswaraiah, K. Rajendar, V. Sampath, Fabrication of Al–SiC–B4C metal matrix composite by powder metallurgy technique and evaluating mechanical properties, Perspectives in Science. 8 (2016) 428–431. doi:10.1016/j.pisc.2016.04.096.

[5] K.D. Woo, D.L. Zhang, Fabrication of Al-7wt%Si-0.4wt%Mg/SiC nanocomposite powders and bulk nanocomposites by high energy ball milling and powder metallurgy, Current Applied Physics. 4 (2004) 175–178. doi:10.1016/j.cap.2003.11.002.

[6] W.K. Kang, F. Yilmaz, H.S. Kim, J.M. Koo, S.J. Hong, Fabrication of Al-20 wt%Si powder using scrap Si by ultra high-energy milling process, Journal of Alloys and Compounds. 536 (2012) S45–S49. doi:10.1016/j.jallcom.2012.01.106.

[7] W.S. Miller, L. Zhuang, J. Bottema, A.J. Wittebrood, P. De Smet, A. Haszler, A. Vieregge, Recent development in aluminium alloys for the automotive industry, Materials Science and Engineering: A. 280 (2000) 37–49. doi:10.1016/S0921-5093(99)00653-X.

[8] E. Tekoğlu, D. Ağaoğulları, S. Mertdinç, A.H. Paksoy, M.L. Öveçoğlu, Microstructural characterizations and mechanical properties of NbB2and VB particulate-reinforced eutectic Al-12.6 wt% Si composites via powder metallurgy method, Advanced Powder Technology. (2018). doi:10.1016/j.apt.2018.05.013.

[9] R. Flores-Campos, D.C. Mendoza-Ruiz, P. Amézaga-Madrid, I. Estrada-Guel, M. Miki-Yoshida, J.M. Herrera-Ramírez, R. Martínez-Sánchez, Microstructural and mechanical characterization in 7075 aluminum alloy reinforced by silver nanoparticles dispersion, Journal of Alloys and Compounds. 495 (2010) 394–398. doi:10.1016/j.jallcom.2009.10.209.

[10] M.S. El-Eskandarany, Introduction, Mechanical Alloying. (2015) 1–12. doi:10.1016/B978-1-4557-7752-5.00001-2.

[11] C. Suryanarayana, Mechanical alloying and milling, Progress in Materials Science. 46 (2001) 1–184. doi:10.1016/S0079-6425(99)00010-9.

[12] Ö. Balci, D. Ağaoğullari, H. Gökçe, I. Duman, M.L. Öveçoğlu, Influence of TiB2 particle size on the microstructure and properties of Al matrix composites prepared via mechanical alloying and pressureless sintering, Journal of Alloys and Compounds. 586 (2014) s78–s84. doi:10.1016/j.jallcom.2013.03.007.

[13] J. Milligan, R. Vintila, M. Brochu, Nanocrystalline eutectic Al-Si alloy produced by cryomilling, Materials Science and Engineering A. 508 (2009) 43–49. doi:10.1016/j.msea.2008.12.017.

Acknowledgements

This study was supported by The Scientific and Technological Research Council of Turkey (TUBITAK) with the project number of 214M093. The authors would like to express their appreciations to Yakup Yürektürk for his help in mechanical tests.

EFFECT OF CASE HARDENING PROCESS PARAMETERS OF ALLOY STEELS ON THEIR WEAR CHARACTERISTICS

Prof. EL-Hebeary, M.R[1]., MSc. EL-Sawy, E.E.T[2], Prof. EL-Bahloul,A.M.M.[3]
[1] Faculty of Engineering, Cairo University., [2]Graduate student, Faculty of Engineering, Cairo University, Giza, Egypt. [3]Faculty of Engineering, Mansoura University ,Mansoura ,Egypt.

elhebeary@yahoo.com

Abstract: *Cane chains are very important transmission elements which are carefully designed according to fatigue strength and wear resistance. To increase the life of cane chains, the resistance of the surface failure should be increased. In this investigation, experiments were carried out to evaluate the wear resistance using wear test rig designed and manufactured for this purpose. Three types of steels were used, namely 16MnCr5, 17CrNiMo6, and 18MnCrB5. Discs manufactured from these steels were carburized for different periods of time (6, 10, and 12 hours). Tempering process was carried out at different temperatures to obtain hardness values of 48, 52, and 56 HRC. The accumulated weight loss was measured and the wear rates were determined for each case hardened steel at the constant normal test load of 800 N. The accumulated weight loss was measured as a function of the number of revolutions. Wear rate was calculated and presented with case hardened depth and hardness for all steels. The hardness distribution and carbon content of carburized layer was presented as a function of the distance from the surface. Carburized layer microstructure and carbide percentage were presented and measured. From test results, it was concluded that the wear rate for all steels under investigation decreases with the increase of their case hardness. Minimum wear rate was obtained at hardness 56 HRC. Wear rate for all steels decreases with the increase of carburizing time tending to reach a minimum at carburizing time 10 hours. Wear rate for steel 16MnCr5 is less than that of the wear rate for 17CrNiMo6 and 18MnCrB5 by about 15% and 45% respectively under the same testing conditions. Carburized layer, carbon content and case depth increase with the increase of carburizing time.*

Keywords: Heat Treatment, Carburizing, Case Hardening, Alloy Steel, Cane Chain, Wear Rate, Sugar Industry.

1. Introduction

Chains are very important transmission elements which are to be carefully designed for efficient working of machines. All parts of chains are subjected to elaborate machining, heat treatment [1], grinding and assembling. Chains are the most important elements in the sugar company.

The parts of chains are manufactured as follows: Rollers should not only have excellent wear resistance but also rigidity; therefore, case hardened alloy steels are used as the material for rollers. Since pins require high wear resistance and toughness, case hardened alloy steels [2], which are rigorously selected and the surface is hardened and ground. Bushes require also wear resistance, case hardened alloy steels with external and internal surfaces hardened and ground.

Chains usually work under the most severe conditions. They are subjected to high tensile load since they are transmitting a large quantity of canes . High wear resistance is necessary to prevent them from wearing away in service. Thus, steels of which chains are made must be properly heat treatable.

Wear resistance is considered as the most important parameter for proper selection of the material to be used for chains manufacturing. Hardness, microstructure and chemical composition of steel play a marked role in wear resistance. Although hardness and relative wear are linearly proportional for most of the commercial metals, the same simple relation does not hold for a range of steels where it becomes necessary to consider chemical composition as well as hardness.

Many papers discuss the wear rate with different case depth and case hardness for different steels [3]. The aim of this work is to study the best heat treatment for chain components with regard to hardness and case depth for the three selected steels 16MnCr5, 17CrNiMo6, and 18MnCrB5. Carburizing process was carried out for 6, 10, and 12 hours, with final hardness values of 48, 52, and 56 HRC, depending on the tempering temperature to select the most suitable material which results in the lowest wear and longer life of chain.

2. Experimental work

2.1. Wear Testing Machine

A rolling contact wear testing machine was constructed purposely for this investigation and presented in Figure 1.

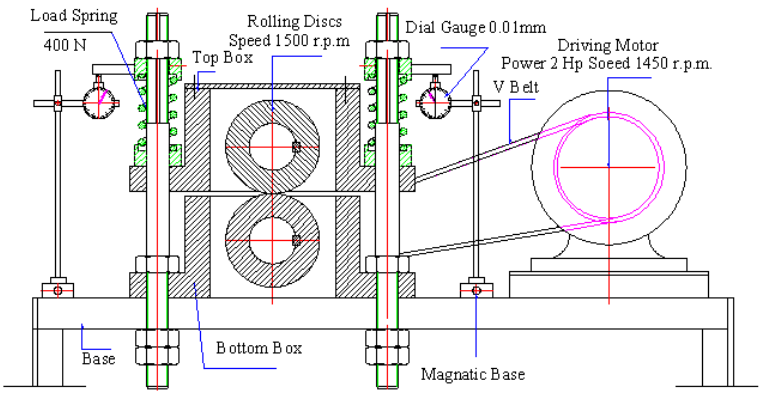


Fig.1. Schematic layout of the test rig.

2.2 calibration curve of spring

Calibration curve for two springs to apply the required load between the drive and the driven rollers are presented in Fig. 2

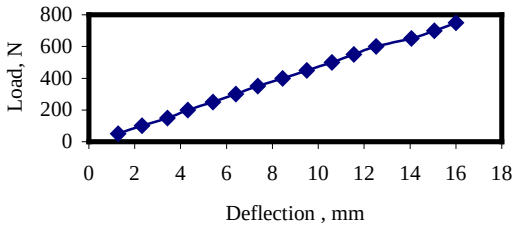


Fig. 2. Calibration curve of spring

2.3. Test specimens

Specimens were obtained in form of round bars 80 mm diameter, for tested materials 16MnCr5, 17CrNiMo6 and 18MnCrB5 and then cut to 15 mm length, which was machined as presented in Figure 3.

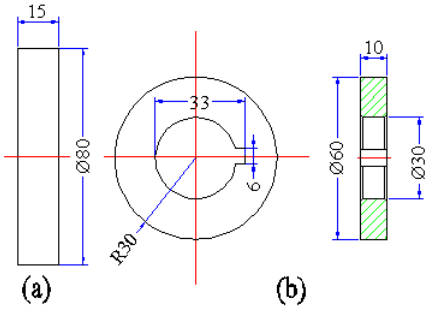


Fig. 3. The shape and dimensions of specimens.

Wear resistance experiments were performed for specimens with heat treatment under dry rolling condition. In this work 54 discs were used, 18 discs from each tested materials, divided into 9 groups; 2 discs for each group. Each group of two discs was subjected to a specific heat treatment conditions. The chemical compositions of tested steels are given in table 1.

Table 1 Chemical composition for tested materials.

Steel	C	Mn	Si	P	S	Cr	Mo	Ni	v	Cu
16MnCr5	0.17	1.17	0.23	0.005	0.009	0.88	0.10	0.082	0.004	0.25
17CrNiMo6	0.17	0.60	0.24	0.009	0.010	1.64	0.27	1.53	0.006	0.19
18MnCrB5	0.18	1.00	0.23	0.011	0.021	1.02	0.24	0.14	0.006	0.11

2.4. Heat treatment of specimens

The heat treatment technique used in this investigation was liquid carburizing followed by hardening and tempering as presented in Figure 4. Discs and other small specimens examinations were heated in liquid carburizing at the temperature of 915^{0}C[4], for a predetermined period of time. The specimens hardening at temperature 860^{0}C and kept for 1 hour to be hardened by oil quenching. After quenching the discs were tempered to obtain the hardness 48, 52 and 56 HRC respectively.

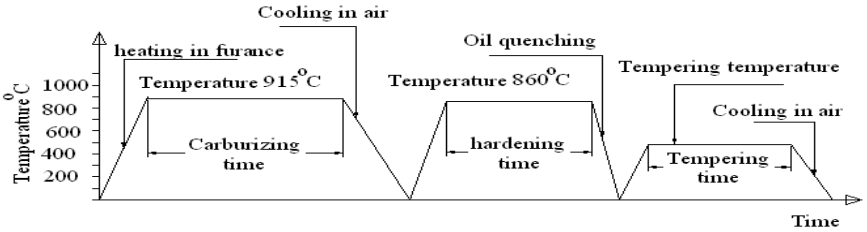


Fig. 4. Applied heat treatment cycle of test discs.

2.5. Wear Measurements

Before each test, the discs were carefully cleaned. The discs were mounted in such a way to have always the same orientation in order to be sure that rolling has occurred in the same starting and direction through out the test. Tests were carried out using a constant load of 800 N created by means of two springs, as shown in Fig. 1. Tests were also carried out at the constant speed of 1500 r.p.m., corresponding to a rolling velocity of 4.71 m/s at the surface of the discs.

The machine was stopped after a predetermined time interval for weighing the discs, after cleaning and dried, using a digital balance of 210 gr capacity and 10^{-4} gr accuracy. The accumulated loss of weight in mgr. was plotted against the number of revolutions. Wear rate was calculated using the following equation [5].

Wear rate = (Accumulated weight of removed metal) / (Load*total number of revolutions).

2.6. Examinations

Hardness, microstructure and Scanning Electron Microscope examinations were carried out using instruments types HWDM7, TSS capacity 1500 HV, optical Microscope type OLMYPUS X50 – X400 and type JSM 5410. Specimens 29 mm diameter and 15 mm length were prepared grinded, polished and etched using 4% Nital solution

Carbon percent distribution in the carburized case was measured using Emission Spectrometer, type Thermo Jarrell Ash (TJA) 181, wave spectra 14000 Kv.

3. Results and Discussion

Figure 5 demonstrates the variation of accumulated loss of the driving and driven discs with the number of revolutions for the as received materials under investigation.

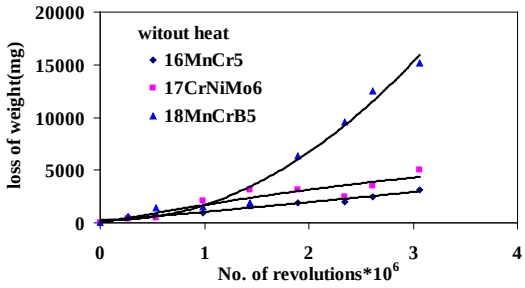


Fig. 5. The losses of weight for tested materials, as received.

Figures (6.a,b) demonstrates the variation of accumulated loss

of weight of the driving and driven discs versus the number of revolutions at carburizing time (6, 10 and 12 hours) for different materials and different case hardness respectively.

From Figures 6.a and 6.b it is noticed that the accumulated loss of weight increases with increasing the number of revolutions for all materials, also for all case depth and case hardness.

Figure 6.a demonstrates the variation of the rate of wear and case hardness for 16MnCr5 at the different carburizing time.

Figure 6.b demonstrates the variation of the rate of wear and carburizing time for 16MnCr5 at the different hardness.

From Figure 6.a it is clear that the wear rate decreases with increasing the case hardness for all tested materials and carburizing time [6]. Also, the wear rate of 16MnCr5 is smaller than that of the wear rate for 17CrNiMo6 and 18MnCrB5 for all carburizing time and from Figure 6.b it is clear that the minimum wear rate occurred at carburizing time 10 hours for all hardness. Also the wear rate of 16MnCr5 is smaller than that of the wear rate for 17CrNiMo6 and 18MnCrB5 for all carburizing time, and from figure, it is clear that the wear rate will decrease with increasing the case hardness[7], and from Figure 6.b it is clear that the minimum wear rate will occur at carburizing time equal 10 hours for all hardness. Also, the wear rate of the hardness 56 HRC is smaller than that of the wear rate for hardness 52 HRC and hardness 48 HRC for all materials.

Wear rate for material 16MnCr5 is less than that of the wear rate for materials 17CrNiMo6 and 18MnCrB5 by about 15% and 45% respectively at carburizing time 10 hours and hardness 56 HRC. This attributed to the carbides contents for material 16MnCr5 is less than that of the carbides for materials 17CrNiMo6 and 18MnCrB5 respectively, the carbides contents for materials 16MnCr5, 17CrNiMo6 and 18MnCrB5 equal to 38%, 42% and 56% respectively.

The retained austenite for steel 16MnCr5 is regular and quantity is less. The retained austenite for steel 17CrNiMo6 is irregular, its volume and area are bigger. The retained austenite for steel 18MnCrB5 is medium but concentrated and its volume is bigger.

The increase of retained austenite resulting from further increase the case depth decrease the yield and ultimate stress of the material[8]. It also decreases the fatigue limit. This is believed to be the reason for the increase in the wear rate. Also for the greatest case depth and case hardness, the rigidity of the case hardened materials increase and a further increase of weight of removed metal and wear rate.

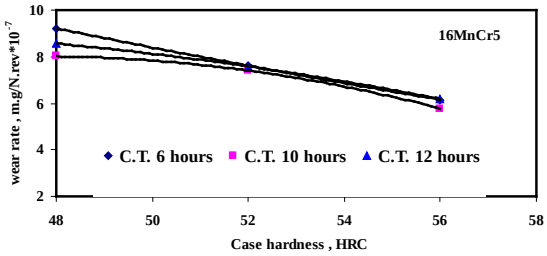


Fig. 6.a. The relation between wear rate and case hardness for steel 16MnCr5

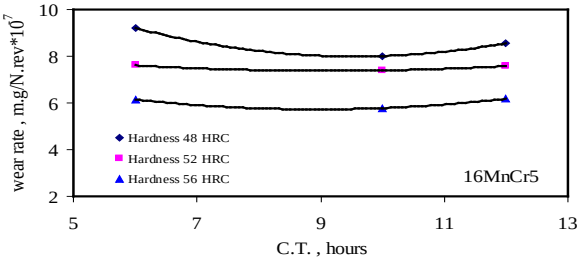


Fig. 6.b. The relation between wear rate and carburizing time for steel 16MnCr5 at the different case hardness.

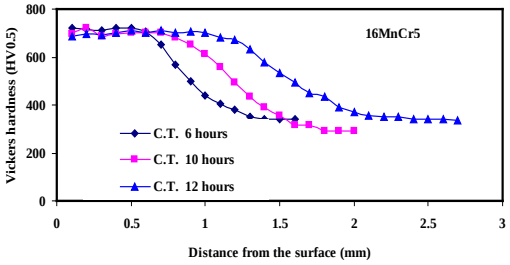


Fig. 7.a. The hardness distribution with subsurface depth for steel 16MnCr5 at different carburizing time.

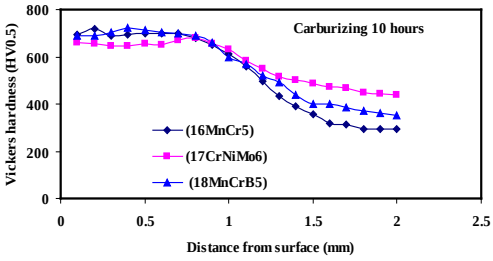


Fig. 7.b. The hardness distribution with subsurface depth for different steels at carburizing time 10 hours.

Figures 7. a, b. Demonstrates the hardness distribution with subsurface depth for different steels and different carburizing time after quenching.

The core hardness of steels16MnCr5, 17CrNiMo6, and 18MnCrB5; measured after quenching are 314, 449, and 333 HV respectively. This attributed to the hardness values increasing as the martensite volume fraction increased [9]. The material 16MnCr5 has lowest wear rate. This result indicates that hardness strongly affects the wear resistance of materials. Martensite for steel 16MnCr5, its distribution is better and quantity is high[10].

From Figures (8, 9 and 10) the retained austenite in material 16MnCr5 is less than that for materials 17CrNiMo6 and 18MnCrB5, and the martensite fraction in material 16MnCr5 is higher than that for materials 17CrNiMo6 and 18MnCrB5. Structure for all materials are martensite, retained austenite and carbide.

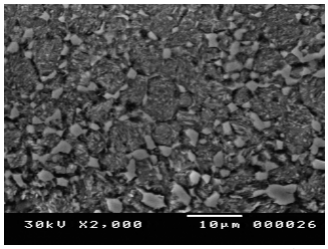


Fig. 8. Material 16MnCr5 after 10 hours carburizing time and hardness 56 HRC.

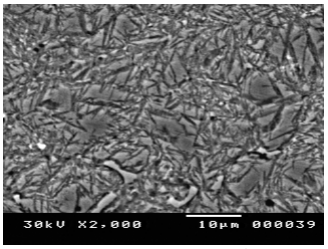


Fig. 9. Material 17CrNiMo6 after 10 hours carburizing time and hardness 56 HRC.

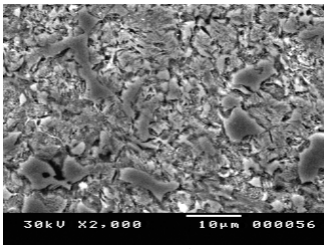


Fig. 10. Material 18MnCrB5 after 10 hours carburizing time and hardness 56 HRC.

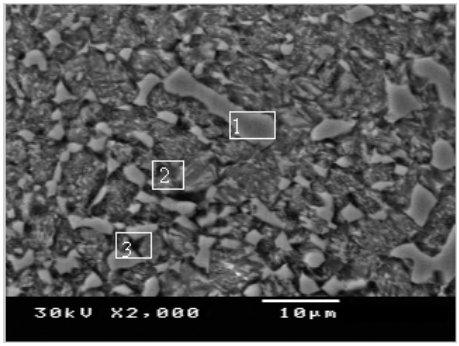


Fig. 11. X-ray analysis of carburized layer for material 16MnCr5 at carburizing time 10 hours and hardness 56 HRC.

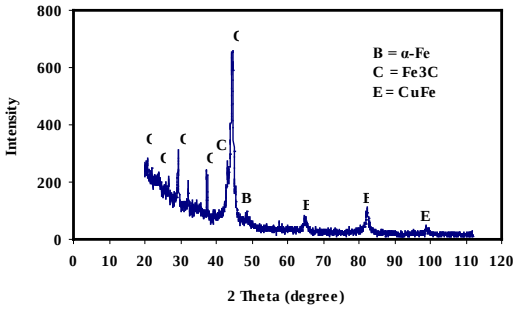


Fig. 12. X-ray diffraction pattern of 16MnCr5 at carburizing time 10 hours and hardness 56 HRC.

Table 2 Chemical composition at points (1,2,3) for material 16MnCr5

Element	Si	Mo	Cr	Mn	Fe	Ni	Cu	C	Point
Wt %	0.1	0.1	4.1	2.5	92.7	0.1	0.4	0.1	1
Wt %	0.1	0.1	1.6	1.6	96.3	0.1	0.4		2
Wt %	0.1	0.4	1.8	2.3	95		0.4		3

The phase structure of the surface alloying layer by X-ray diffraction for material 16MnCr5 at carburizing time 10 hours and hardness 56 HRC.

Table 3 Phases present in material 16MnCr5 at carburizing time 10 hours and hardness 56 HRC.

Phase number	Symbol	Phase name	Crystal structures
01 – 085 – 1410	α – Fe	Martensite	Cubic
01 – 085 – 0871	Fe_3C	Iron Carbide	Orthorhombic
01 – 071 – 7667	Fe, Cu	Copper Iron	Cubic
00 – 023 – 0298	Fe, C	Austenite	Cubic

X-ray analysis was shown in figure 12. The carbides in the diffusion layer formed by alloying and carburizing were α – Fe, Fe_3C, and Fe, Cu. And table 3 shows the types and the phases for material 16MnCr5 [11].

From microstructure, Scanning Electron Microscope (SEM) and X-ray diffraction, it was noticed that the retained austenite for material 16MnCr5 is regular and quantity is less. Furthermore, martensite distribution is better and its area fraction is larger.

Conclusions

1- Wear rate for all materials under investigation decreases with the increase of their case hardness. Minimum wear rate was obtained at hardness 56 HRC.

2- Wear rate for all tested materials decreases with the increase of carburizing time, tending to reach a minimum at carburizing time 10 hours. This may be attributed to the decrease in retained austenite in the carburized matrix. Further increase of the carburizing time may result in a pronounced increase in wear rate due to larger area of carbides obtained at longer carburizing time.

3- Wear rate for material 16MnCr5 is less than that of the wear rate for 17CrNiMo6 and 18MnCrB5 by about 15 % and 45% respectively under the same testing conditions.

4- Carburized layer, carbon content and case depth increase with the increase of carburizing time.

5- The appearance of the retained austenite was accompanied by a decrease in both hardness and wear resistance of tested materials.

6- Wear rate for materials 16MnCr5, 17CrNiMo6 and 18MnCrB5 at carburizing time 10 hours and hardness 56 HRC is less than that of the wear rate for the same materials without heat treatment by 55%, 67% and 83% respectively.

References

1 El-Bahloul, A.M.M., Sammed, A.A. and Rassoul, S.A.,((Improving the wear resistance of Egyptian steels by case hardening)) PEDAC 92, Dec. 27-29 (1992) 13 – 21.

2 El-Bahloul, A.M.M., Sammed, A.A. and Rassoul, S.A.,((On the effect of microstructure on wear resistance of steels)) PEDAC 92, Dec. 27-29 (1992) 37 – 44.

3 El-Bahloul,A.M.M.,((Surface capacity of gears of circular-arc tooth-profile))Wear, 193 (1996), 146 – 154.

4 Zakharov, B.,((Heat treatment of metals)) Peace Publishers, Moscow (1962) 110 – 113.

5 Krishnakumar. K, Arockia Selvakumar. A, ((A Review of Failure analysis found in Industrial Roller Chains)) International Journal of ChemTech Research, Vol.8, No.12 pp 598-603, 2015.

6 Wieczorek, A.N., Myszka, D.,((Abrasive wear properties of Fe-Based alloys desiged for mining applications)) Arch. Metall. Mater. 62 , 3, 1521-1534, 2017.

7 Paul Aondona Ihom, ((Case hardening of mild steel using cowbone as energiser)) African Journal of Engineering Research, Vol. 1(4), pp. 97-101, October 2013.

8 Tatsuya K., Manabu K. and Suguru Y., ((Effect of Si Concentration on Carbon Concentration in Surface Layer after Gas Carburizing)) ISIJ International, Vol. 56, No. 9, pp. 1638–1645,2016

9 Luciana S.R.,Danilo B. V., Jeferson A.M., Cassius O.F.T. R., ((Surface Contact Fatigue Failure of a Case Hardened Pinion Shaft)) Materials research, 17(3), 535-541, 2014.

10 Mohammed Abdulraoof Abdulrazzaq,((Investigation the Mechanical Properties of Carburized Low Carbon Steel)) Int. Journal of Engineering Research and Application, ISSN: 2248-9622, Vol. 6, Issue 9, (Part -2), pp.59-64, September 2016.

11 Oyetunji A. and Adeosun S.O., ((Effects of Carburizing Process Variables on Mechanical and Chemical Properties of Carburized Mild Steel)) Journal of Basic & Applied Sciences, 8, 319-324, 2012.

DIRECT OBSERVATION OF THERMAL EFFECT APPEARANCE DURING GRAIN BOUNDARIES COMPLETE WETTING TRANSITION IN COPPER-BISMUTH SYSTEM

Ass. Novikov A[1]., PhD Kondratiev A., Prof. Dr. Eng. Bokstein D.,Prof. Dr. Eng. Petelin A[2]., PhD Novikova E.
National University of Science and Technology «MISIS»

E-mail:[1] novikov@misis.ru , [2]alexander-petelin@yandex.ru

Abstract: *Grain boundary wetting process takes place during the contact of solid metal phase with the metal melt. The liquid bismuth network formation along grain boundaries (GB) connected with wetting process was investigated in copper polycrystalline samples. The endothermic thermal effect in the temperature range close to complete GBs wetting transition temperature for Cu-Bi system was observed. Thermal effect size of GB wetting per mol of copper passed into bismuth melt during process of forming wetting GB channels was characterized as 21-23 kJ/mol.*

KEYWORDS*: GRAIN BOUNDARIES, COMPLETE WETTING, COPPER, BISMUTH, THERMAL EFFECT, TRANSITION TEMPERATURE*

1. Introduction

Grain boundaries wetting via interaction of solid copper with bismuth melt saturated with copper was investigated in detail in works of several liquid-metal wetting research teams [1, 2]. In particular it has been found that in temperature interval 560 – 620 °C in polycrystal copper samples transition to grain boundaries (GB) complete wetting takes place, wherein GB surface energy (γ_b) passes through a value equal to double energy of boundary surface solid copper - melt ($2\cdot\gamma_{SL}$) and by further heating becomes larger than it. Each GB in polycrystal has its own complete wetting transition temperature [3] that is due to the fact that GB surface energy is different in any single case because of individual crystallographic misorientation of bound grains [4]. As a consequence, complete wetting transition temperature range in polycrystal occurs. At temperatures higher than complete wetting temperature, instead of GB a substitutional grain boundary melt channel forms; and it "eats" overtime GB al over it [5].

The morphology of complete wetting growing channels and kinetics of their growth were investigated in [6]. In the work [7] it is marked that via passing to complete wetting negligible positive (absorbing) thermal effect may be observed. The reasons and the value of the effect, as well as the fact of its existence are still opened to question. That is why the aim of this investigation was reliable detection of GB complete wetting transition thermal effect and its quantitative assessment for the system copper – bismuth.

2. Experimental

For the thermic analysis of thermal effect interactability connected with GB wetting with melt the process of polycrystal copper sample should be investigated, i.e. the sample that contains large amount of GBs in contact with bismuth. At temperature close to 271 °C (melting point of pure bismuth) bismuth, saturated with copper, melts, that provides melt interactability with GBs of solid copper sample via further heating. The heating process itself as well as concurrent thermal effects measurement was carried out with the use of differential scanning calorimeter DSC Labsys.

In experiments copper (with purity 99,996 mass %) and chemically pure bismuth (99,99 mass%) were used. Bismuth melt was saturated with copper till the saturation concentration at a temperature of 650 °C.

Studying the process of heating the copper in contact with bismuth was carried out in two variants. They differ in that: in the first case the copper samples with a polycrystal structure with a predetermined grain size were used. In the second case, the copper samples, that were prepared, have the same size and shape as in the first case but which have a monocrystal structure. It helps to identify effects associated only with GBs, because in the first case (a polycrystal) there were enough of them, and at a given grain size we could make an estimate of their total amount in the test sample. In the second case, they were no effects (a monocrystal), and thus GB grooves and channels at complete wetting could not be formed. (Volume dissolution of copper samples in both cases could not occur, because they were in contact with saturated with copper bismuth melt).

For polycrystal and monocrystal versions of copper samples the original copper subjected to preliminary mechanical deformation (sediment under pressure) and subsequent heat treatment. Selection of an appropriate heat treatment conditions in the first case provided the polycrystal samples with an average grain size of 50 microns. Heat treatment in the second case allowed growing to a value of grain diameter of 5-7 mm. The grain size was determined by optical microscope Leica DMILM and scanning electron microscope Hitachi S-800. Using the method of electroerosion cutting, the copper samples were cut from large grain preform to monocrystal containing no more than one of each grain. The size of each copper blanks for runs in the first and second cases was the same. Blanks were made as thin circular disks of thickness 300 mm and 5 mm in diameter, which corresponds to the conditions of their use in the differential scanning calorimeter Setaram «AlexSys».

In both cases copper plates in contact with crushed bismuth (saturated with copper) were put into alumina crucible posed in the calorimeter. In the atmosphere of high-purity argon the samples were heated with the rate 5 K/min from room temperature (25^0C) to 650 °C, and inverse cooling with the same rate to room temperature. Consequently, calorimetric curves "heating –cooling" became available:- in the first variant – for the polycrystal copper plates in contact with bismuth;- in the second variant – for the monocrystal copper plates in contact with bismuth.Basic materials and experimental regimes in both cases were the same.

3. Results

Fig. 1 shows the thermal heating curves of polycrystal copper samples in bismuth (upper curve) and monocrystal copper samples in bismuth (lower curve). At a temperature of about 270 C (the exact value of 267 C) in both curves the deep (substantial) positive thermal effect is observed. It is associated with the melting of bismuth (saturated with copper) that is present in both cases. Further heating to a temperature of 590 C for both variants occur

without observed thermal effects. When such heating studied melts liquidus point is not achieved [8]. At temperatures of 596-615 C samples with polycrystal structure demonstrate double positive thermal effect, which is clearly seen in the inset in the right part of Fig. 1 on an enlarged scale. This effect is small in comparison with the effect of melting bismuth, but it appears quite clearly. At the lower curve (monocrystal copper), this effect is absent.

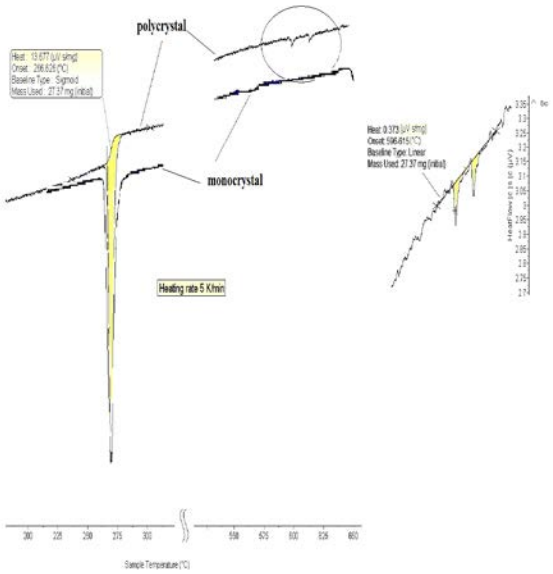


Fig.1. *Thermal heating curves of polycrystal (upper curve) and monocrystal (lower curve) copper samples in the bismuth melt.*

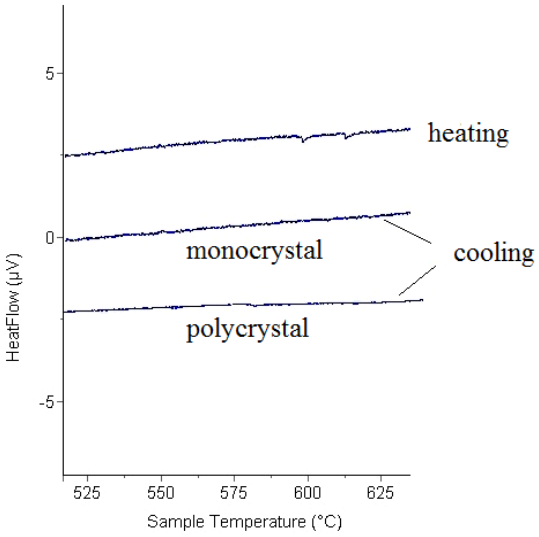


Fig.2. *Thermal cooling curves of the polycrystal copper (lower curve) and the monocrystal copper (middle curve) in the bismuth melt. The upper curve shows the temperature interval of occurrence of the thermal effect when heated polycrystal copper in bismuth.*

Fig. 2 shows the thermal cooling curves of polycrystal and monocrystal copper in bismuth melt. The temperature range of cooling curves is associated with the temperatures of the thermal effect appearance during heating of polycrystal copper in bismuth, which is presented for comparison in the same figure (upper curve). It may be noted that cooling occurs in both cases the same, without the observed thermal effects.

The full view of curves "heating - cooling" can be found in a scaled-down view by the example of copper monocrystal samples in contact with bismuth in fig. 3

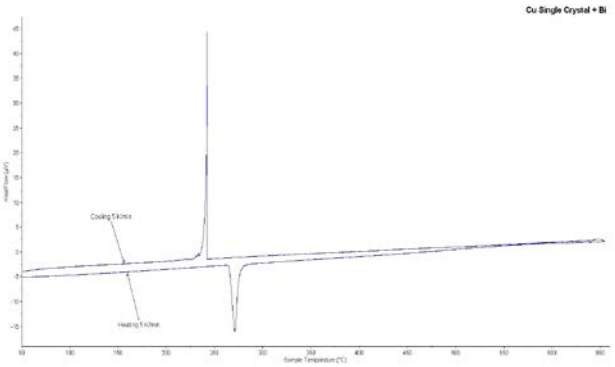


Fig. 3. *Thermal curves "heating-cooling" for monocrystal copper in contact with bismuth.*

The presented curves show that the monocrystalline copper in contact with bismuth undergoes no transformations in the "heating - cooling" process in the temperature range 25 – 650 C. Bismuth melts independently from copper (positive effect on the heat curve) and crystallizes (a negative effect on the cooling curve). Similar curves for polycrystal copper in contact with bismuth differ from those shown in fig. 3 only in the presence of a positive thermal effect at 596 - 615 C (see Fig. 1), which is inappropriate to show in this scale.

When the experiment had been carried out, metallographic specimen of polycrystal copper in sections perpendicular to the plane were made, i.e., contact surfaces of solid copper and bismuth melt at temperatures above 270 C. Fig. 4 show photo of the copper microstructure. In picture GBs are clearly visible, which are partially or completely filled with bismuth. Light thin strips of bismuth are grain-boundary channels of penetration of the melt in the complete wetting of the GB. However, it should be noted that only a part of GBs in a polycrystal sample is filled with bismuth, there are a completely "empty" (i.e. without bismuth) GBs as well as partially "empty" GBs.



Fig. 4. *Microstructure of polycrystal copper after "heating - cooling" in bismuth melt.*

Detailed analysis of microphotographs of specimen of polycrystal copper after the "heating - cooling" in bismuth melt has

given the opportunity to assess the proportion of GBs filled with bismuth, i.e., the proportion of GB channels of bismuth formed during the experiment (fraction of fully wetted with bismuth GBs in samples of polycrystal copper). This proportion is approximately 10 % of all GBs in polycrystal samples, which were in contact with bismuth during the experiment.

4. Discussion

Calorimetric study of the copper polycrystal samples heating in bismuth melt showed that in the transition temperature range of the GBs to complete wetting with melt the thermal effect is observed, which is absent in the same conditions in case of monocrystal samples, i.e. in the absence of GBs. As in the polycrystal occurs the growth of deep GB channels, it is natural to assume that this process is the cause of the thermal effect. We can assume that the thermal effect is a consequence of the withdrawal of copper from sample volumes (border volumes), which when GBs were wetted were filled with bismuth. The only way out of copper from the border areas of the grain and making space for melt via formation of channels is the transition (displacement) it in melt, and thus the formation of a supersaturated bismuth-copper melt. Copper dissolution in the melt can be regarded as the cause of the thermal effect when wetted GBs. The fact, that in a subsequent cooling the occurrence of any thermal effects up to the crystallization temperature of bismuth is not marked, is that reversibly reverse formation of dissolved during the formation of GB channels copper does not happen.

The heat effect magnitude, accompanying the transition to complete wetting of the GBs and the formation of GB channels, can be estimated from the known heat of bismuth melting $-\Delta H_{S \to L}$ (Bi). The area on the thermal curve corresponding to the thermal effect on bismuth melting is proportional to the total heat absorbed by the sample containing a known amount of moles of bismuth. The magnitude of the thermal effect upon GB wetting (596-615 ^{0} C) may be determined by the ratio of areas of the GB melting thermal peak and the peak at the bismuth melting. Using this fact thermal effect of GB wetting, divided by the total mass of the sample, was calculated. It was equal to 0.0327 J.

To compare the magnitude of the observed thermal effect with the magnitude of changes in the surface energy of the transition to the complete wetting of the GBs was estimated surface area of GBs filled with bismuth melt. For this purpose it was assumed that the copper grains in the sample have the form of cubes (calculation in the first embodiment) or icosahedron (in the second embodiment). Geometric analysis allowed in both cases by the proportion of wetting GBs (10%) to determine the surface area of the GBs wetting, which was found to be $1.7 \cdot 10^{-5}$ m^2 in the first case and $1.8 \cdot 10^{-5}$ m^2 in the second case. Thus, the magnitude of the thermal effect per surface unit of GBs wetted by bismuth melt is about $2 \cdot 10^3$ J/m^2. This is thousands of times greater than the possible values of the surface energy associated with the GB and the boundary of solid and liquid phases in the Cu - Bi (the value of the surface energy at the boundaries of Cu_s - Bi_L is 0.2 - 0.4 J/m^2 [9]). This indicates that the observed thermal effect is not associated with capillary processes at GBs.

We can assume that the absorbed heat when GBs were wetted is associated with the transition of the copper to the bismuth melt - this is the heat of dissolution. Dissolution of copper in bismuth by GBs is stimulated by the process of wetting. The solubility of copper in liquid bismuth increases with temperature, the wetting process "imitates" the temperature increase near the GBs and initiates a transition of the copper into the melt. All the heat that would absorb when copper was dissolved in bismuth with temperature increase is being recorded in a narrow temperature range in the transition to complete wetting of the GBs.

Then the effect of the heat on 1 mole of copper, passed into the melt was estimated. The volume of GB formed channels (thickness of bismuth in the channels was assumed to be 2 microns), and the amount of copper in the moles, repressed in the melt when wetted were determined. As a result, the thermal effect value was obtained equal to 23 kJ/mol (cubic grain shape for copper) and 21 kJ/mol (for the icosahedral shape of grains of copper). It is of the same order of magnitude as the fusion heat of pure copper which equals to 13 kJ/mol. Received "specific" values of the thermal effect, as can be seen, not very sensitive to the method of description of the grain structure of the sample. But they may undergo significant changes due to the influence of the two factors that require a reliable experimental confirmation. This is the value of the thickness in the GB layer of bismuth channels which, as shown by microarray analysis, may vary for different channels and at different depths within a wide range (0.1 to 10 microns). Furthermore, this is proportion value of bismuth fill GBs of all GB network of the sample. Both of these quantities cannot be defined exactly, the interval value depends on the depth of the statistical analysis of the sample structure after thermal tests. Those are why the values of the thermal effect of wetting the GBs should be regarded as tentative, and require clarification.

5. Conclusion

In consequence of the experiments on copper GB complete wetting with bismuth melt study that were carried on, it was found that:

- thermal effect due to process of passing to copper GB complete wetting was found which is proved by carrying out a parallel investigation of monocrystal copper behavior in bismuth melt when heated;

- thermal effect size of GB wetting per mol of copper passed into bismuth melt via process of forming wetting GB channels was characterized as 21-23 kJ/mol.

6. References

[1] B. Joseph, F. Barbier, G. Dagoury, M. Aucouturier: Scripta Mater. Vol. 39 (1998) p. 775.

[2] B. Joseph, F. Barbier, M. Aucouturier: Vol. 42 (2000) p. 1151.

[3] B. Straumal, T. Muschik, W. Gust, B. Predel: Acta metall. mater. Vol. 40 (1992) p. 939.

[4] T. Yoshino, Y. Nishihara, S.-I. Karato: Earth and Planetary Science Letters, Vol. 256 (2007) p. 466.

[5] Y. Amouyal, S.V. Divinski, Y. Estrin, E. Rabkin: Acta Materialia, Vol. 55 (2007) p. 5968.

[6] A.A. Novikov, B.S. Bokstein, A.L. Petelin, A.O. Rodin: Vol. 133 (2014) p. 113.

[7] B.B. Straumal, S.A. Polyakov, E. Bischoff, W. Gust, B. Baretzky: Acta Mater. Vol. 53 (2005) p. 247.

[8] T.B. Massalski (Ed.), Binary Alloy Phase Diagrams, 2nd ed., ASM International, Materials Park, OH, 1990.

[9] V. Missol, Phase interface surface energy in metals. M.: Metallurgiya, 1978, p. 176.

ELECTRODEPOSITION OF SILVER AND ITS INFLUENCE ON THE FORMATION OF COATINGS OF MOLYBDENUM CARBIDE IN TUNGSTATE-MOLYBDATE-CARBONATE MELTS

Prof., Dr. Sc. Malyshev V. [1], Prof., Dr. Sc. Kushchevska N. [1]., Prof., Dr. Sc. Bagliuk G. D.Sc.[2,], Ph.Dr. Gab A.[1], Ph. Dr. Lukashenko T.[1], Prof., Dr. Sc. Gaune-Escard M. [3]
Institute for Engineering & Technology – University "Ukraine", Ukraine [1]
I.M. Frantsevich's Institute for Problems in Materials Science of the National Academy of Sciences of Ukraine, Ukraine [2]
IUSTI, Ecole Polytechnique, Aix-Marseille University, France [3]

gbag@ukr.net

Abstract: *Electrochemical behavior of silver in tungstate-molybdate melts was studied by potentiometric and voltammetric methods. The electrode process was identified as a single-electron reversible one. The effect of silver on the electrochemical deposition of molybdenum carbide coatings and their electrochemical corrosion behavior in a sodium polysulfide melt was studied.*

Keywords: ELECTRODEPOSITION, MOLYBDENUM CARBIDE, SILVER, COATING, POWDER

1. Introduction

Electrochemical deposition of molybdenum carbide coatings from oxide and halide-oxide melts was studied earlier. Deposition of coatings with a thickness of up to 50 μm and roughness of 2-3 μm was shown to be possible. The effect of silver ions on electrochemical deposition of tungsten and tungsten carbide from chloride melts was also described [1, 2]. But the effect of silver ions on electrochemical deposition of molybdenum carbide from tungstate-molybdate-carbonate melts has not been studied yet.

In order to study cathodic reduction of silver from a tungstate melt, and apply it for electrochemical deposition of molybdenum carbide-silver coatings, we used a complex of electrochemical and physico-chemical methods such as: voltammetry, potentiometry, potentiostatic and galvanostatic electrolysis, X-ray analysis, and profilometric analysis.

2. Experimental

All the measurements were performed with an access for air. A graphite crucible (grade MPG-7) with the melt acted as an anode. The melt was prepared from pre-dried components: analytical grade Na_2WO_4 and Na_2MoO_4, chemically pure MoO_3 and $LiCO_3$. Silver molybdate was synthesized in a form of deposit by mixing aqueous solutions of $AgNO_3$ and Na_2MoO_4. A half cell [$Pt,O_2|Na_2WO_4$-$0.2WO_3$] acted as a reference electrode. It was separated from the bulk melt by an alundum diaphragm [3, 4]. A face silver indicator electrode was prepared by melting the silver in an alundum tube of 1.5 mm diameter. Nickel plates (10 x 20 x 1 mm) were used as cathodes for the electrochemical deposition.

Electrochemical behavior of both molybdenum and silver should be known for elaborating the process of their electrochemical codeposition with a formation of electroplate. The electrochemical behavior of molybdenum was studied earlier [5].

3. Result and discussion

3.1 Electrochemical behavior of silver in the tungstate-molybdate melt

Two waves are observed in voltammograms for Na_2WO_4-MoO_3-Ag_2MoO_4 melts at -(0.3-0.5) V and –(1.1-1.2) V (Fig. 1). The last of them corresponds to reduction of dimolybdate ions $Mo_2O_7^{2-}$ to molybdenum metal. The major wave at the platinum electrode is preceded by the alloy-formation wave absent at the silver electrode. Potentiostatic electrolysis at the first-wave potential produces silver metal. The following changes occur in the current-potential curves with increasing Ag_2MoO_4 concentration: the silver deposition potential is shifted by about 300 mV positive; the $Mo_2O_7^{2-}$ reduction wave potential is shifted from -(1.1-1.2) V to -(0.3-0.4) V due to electrodeposition of molybdenum on already deposited silver, the molybdenum oxidation wave is displaced from -(1.0-1.1) V to -(0.3-0.4) V.

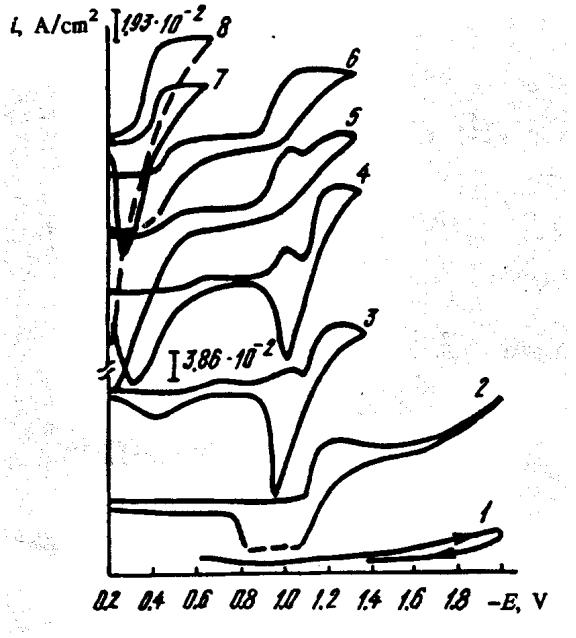


Fig. 1 *Voltammograms for Na_2WO_4 (1), Na_2WO_4 - 2mol.%MoO_3 (2), and Na_2WO_4 - 2mol.%MoO_3 - Ag_2MoO_4 melts with the following concentrations of Ag_2MoO_4: 3,4 - 2.5×10^{-5}; 5 - 5×10^{-5}; 6 - 7.5×10^{-5}; 7 - 1×10^{-4}; 8 - 1.5×10^{-4} mol/cm^3. Cathode - Pt, T = 1173 K.*

Potentiodynamic polarization curves of the silver electrode in the melt Na_2WO_4-MoO_3-Ag_2MoO_4 (Fig. 2) exhibit two waves in the potential ranges -(0.3-0.5) V and -(1.1-1.2) V, respectively. The first wave corresponds to the cathodic reduction of silver ions Ag^+ to the metallic silver. The second wave indicates the reduction of dimolybdate ions $Mo_2O_7^{2-}$ to the metallic molybdenum.

A proportionality between the limiting current i_1, and the Ag_2MoO_4 content; the wide-range independence of the $i_1/v^{1/2}$ ratio from the scanning rate of the electrode polarization (here i_1, is the limiting current, $v= dE/d\tau$ is the scanning rate), as well as the magnitude of the diffusion constant i_1/nFc (1-6 μm/s) indicate the diffusion control of the electrode process. Stationary polarization curves plotted in semilogarithmic coordinates E - $\log(i_d - i)$ confirm the single-electron reversible type of the charge transfer ($0.93 < n < 1.19$) (Fig. 3).

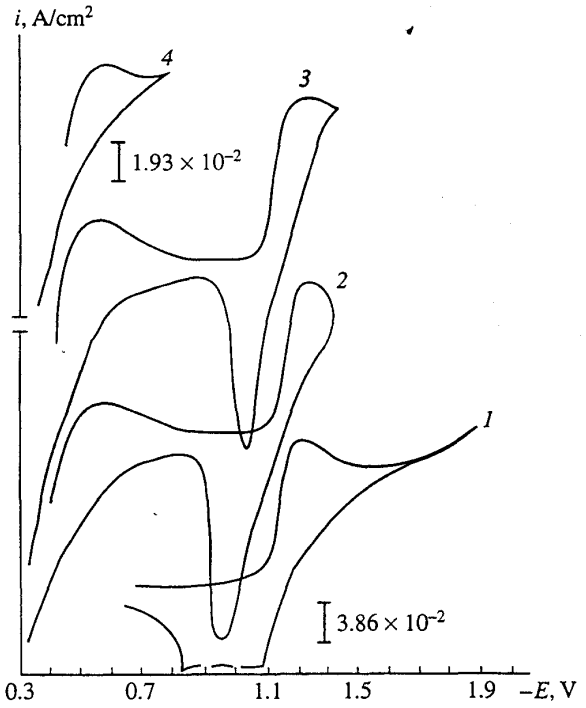


Fig. 2 *Potentiodynamic polarization curves (T = 1173 K, polarization rate 0.1 V/s) of the Ag electrode in the following melts: Na_2WO_4 - 2mol.% MoO_3 (1); Na_2WO_4 - 2mol.% MoO_3 - 75 mmol/l Ag_2MoO_4 (2); Na_2WO_4 - 2mol.% MoO_3 - 100 mmol/l Ag_2MoO_4 (3); Na_2WO_4 - 2mol.% MoO_3 - 250 mmol/l Ag_2MoO_4 (4).*

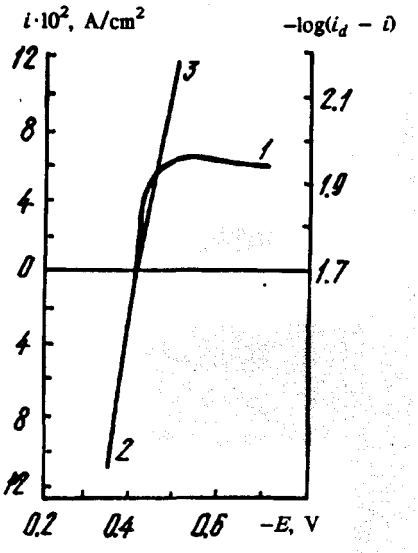


Fig. 3 *Cathodic (1) and anodic (2) polarization of silver electrode in Na_2WO_4 - 1×10^{-4} mol/cm³ Ag_2MoO_4 melt and its semilog presentation (3). T = 1173 K.*

Potentiodynamic measurements (Fig. 4) lead to the following conclusions: (1) the silver equilibrium potential does not depend on MoO_3 content within its range from 1 to 20 mol %; (2) the dependence of silver equilibrium potential on the Ag^+ concentration corresponds to the single-electron reaction; and (3) platinum-oxygen electrode potential is almost independent of Ag_2MoO_4 content.

The abovementioned indicates that silver in the sodium tungstate solution exists in a form of single-charged cations Ag^+, that are not bonded with the O^{2-} ions.

Silver deposition potential is 0.5 - 0.6 V higher than that of molybdenum. Insofar as there are no Ag-Mo alloys in the phase diagram [6-8], silver may be supposed to somehow affect the electrochemical deposition of the molybdenum carbide and, in so doing, to affect properties of the electroplate.

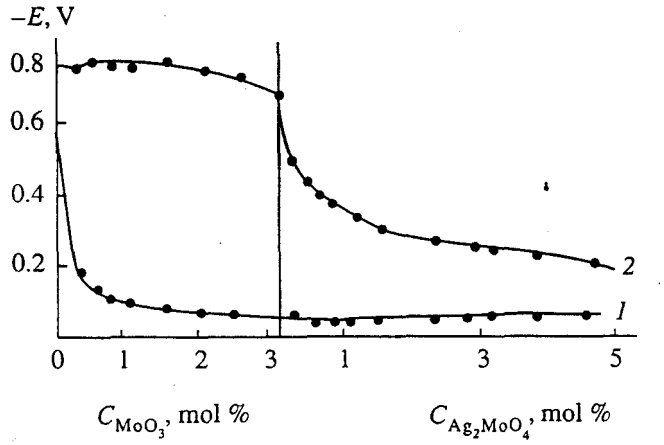


Fig. 4 *Chronopotentiometric curves of Mo (1) and Ag (2) electrodes in the Na_2WO_4 melt with the sequential addition of MoO_3 and Ag_2MoO_4. T = 1173 K.*

3.2 The effect of silver and the electrolysis conditions on electrochemical deposition of molybdenum carbide deposits

The effect of silver on the electrochemical deposition of Mo_2C coatings was studied earlier in a Na_2WO_4-Na_2MoO_4-5mol.%MoO_3-10mol.%Li_2CO_3 melt. Silver molybdate was added within the concentration range from 10^{-3} to 10^{-1} mol.%. A graphite crucible (grade MPG-7) was used as the anode. Nickel plates (10 x 20 x 1 mm) were used as the cathodes. Electrochemical deposition of Mo_2C was performed at 1073 -1223 K and cathodic current density of (2-50) x 10^2 A/m^2. The deposit was subjected to X-ray analysis (using a diffractometer DRON-2.0) and profilometric analysis (using a profilograph PR-201). The thickness of the coatings was measured by a high-speed indicator 2IGM.

Small additions of Ag_2MoO_4 (10^{-3}-10^{-2} mol.%) to the previously studied electrolyte result in significantly decreasing the roughness of the electroplate (the profile amplitude becomes lower than 1 μm instead of 2-3 μm) and increasing its maximum thickness to 150 um. However, when Ag_2MoO_4 content exceeds 10^{-2} mol %, the deposit becomes spongy and their adhesion to the substrate worsens.

At 1073 K and Ag_2MoO_4 content 10^{-3}-10^{-2} mol.% the spongy deposits Mo_2C-Ag are formed. In a temperature range of 1073 to 1123 K thin (up to 10 μm) deposits are obtained, while above 1223 K they are again non-adhered and spongy. The optimum is a range from 1123 to 1173K.

When cathodic current density is lower than 5 A/dm^2, the metallic silver is mainly deposited, within the range 5-15 A/dm^2 it is a Mo_2C-Ag coating with proper adhesion, and at a higher current density the dendrites rapidly begin to grow.

The co-deposited silver increases the free corrosion potential of Mo_2C by 0.7-0.8 V, i.e. from -1.05 ± 0.05 to -0.35 ± 0.05V.

3.3 Corrosion-electrochemical behavior of steel 45 electroplated with molybdenum carbide, in the sodium polysulfide melt

Weight loss of the samples with a Mo_2C-Ag electroplate after a 34-day test in the Na_2S_3 melt at 623 K is 3.5 ± 0.5 g/m^2, which is comparable to the losses of the diffusionally chromized Steel 45. This testifies the applicability of the electroplating for corrosion protection of containers for sodium-sulfur chemical cells.

Cyclic potentiodynamic polarization curves of the electroplated and diffusionally chromized Steel 45 recorded in the Na_2S_3 melt at 623 K are similar (Fig. 5), being analogous to the curves of the graphite electrode [9]. The cathodic peak A is attributed to a formation of the blocking layer of Na_2S_2 and the peak B is attributed to the transformation of Na_2S_2 to Na_2S. Polarization curves of samples with porous electroplate (Fig. 5) exhibit also peaks C and D, which are peculiar to steel electrodes. The peaks become more distinct with an increase in the test duration, thus

indicating the accelerated etching of the defects. This fact can be used to assess the quality of plating.

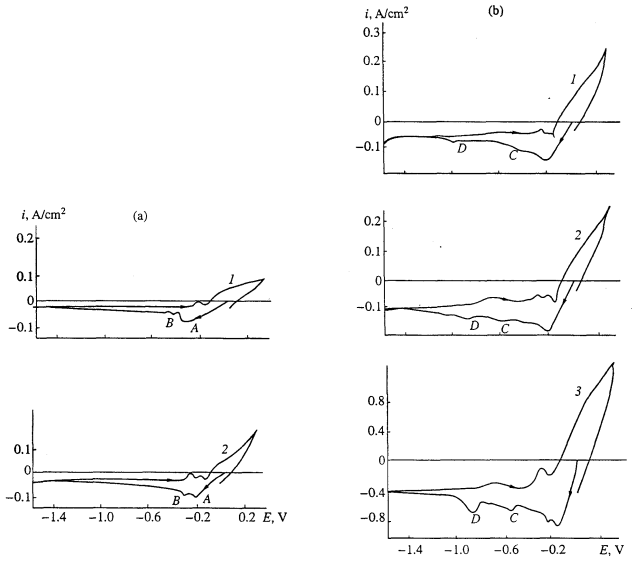


Fig. 5 *Cyclic potentiodynamic (0.01 V/s) polarization curves (T = 623 K) of the coated steel 45 in Na_2S_3 melt: (a) proper coatings: (1) diffusionally chromized; (2) electroplated with molybdenum carbide - silver; (b) porous with molybdenum carbide - silver coatings after exposure to the melt for 0.5 h (1) and 3 h (2); uncoated steel 45 (3).*

4. Conclusion

Electrochemical behavior of silver in tungstate-molybdate melts was studied. The electrodeposition of silver proceeds according to the single-electron reversible mechanism and is diffusionally controlled. The effect of silver on the electroplating with molybdenum carbide was also studied. Conditions for proper electroplating were experimentally determined. The electroplates may be recommended for pilot corrosion protection of containers for sodium-sulfur chemical cells.

5. Literature

[1] Malyshev V.V., Kushkov H.B., Shapoval V.I., Environmentally appropriate technologies and resource saving in high-temperature electrochemical synthesis, deposition of metal coatings on superhard materials, and processing of used cutting and boring tools, in book «Green Industrial Applications of Ionic Liquids, ed. by R.D. Rogers et al., Kluwer Academic Publishers, the Netherlands, 2003.

[2] Malyshev V., Electrodeposition of different types of tungsten cathode deposits from ionic melts, Materials Science, 47, 2011, 345-354.

[3] Zoski C.G., Handbook of Electrochemistry, Elsevier, 2007.

[4] Laboratory Techniques in Electroanalytical Chemistry, ed. by Kissinger P.T., Heinemann W.R., 2nd ed., N.Y., Marcel Dekker, Inc., 1996.

[5] Malyshev V., Gab A., Gaune-Escard M., Molybdenum Electrometallurgical Processes in Ionic Melts, Materials and Manufacturing Processes, 23, 2008, 748-751.

[6] Kurlov A.S., Gusev A.I., Tungsten and Molybdenum Carbides and W(Mo)–C Diagram, Inorganic Materials, 42, 2006, 121-127.

[7] Chapter 2: Phase diagrams in alloy systems, Intermetallic Chemistry, ed. by Ferro R., Saccone A., Pergamon Materials Series, 13, 2008, 7-80.

[8] Science of Hard Materials, ed. by Viswanadham R., Springer, 2012.

[9] Dobson J.C., McLarnon F.R., Cairns E.J., Voltammetry of Sodium Polysulfides at Metal Electrodes, J. Electrochem. Soc., 133, 1986, 2069-2076.

DEVELOPMENT OF METHODS FOR CALCULATING THE NONEQUILIBRIUM PHASE TRANSFORMATIONS DURING THE CONDENSATION OF SUPERCOOLED STEAM IN THE TURBINE FLOW PATH

РАЗРАБОТКА МЕТОДОВ РАСЧЕТА НЕРАВНОВЕСНЫХ ФАЗОВЫХ ПРЕВРАЩЕНИЙ ПРИ КОНДЕНСАЦИИ ПЕРЕОХЛАЖДЕННОГО ПАРА В ПРОТОЧНОЙ ЧАСТИ ТУРБИНЫ

Member-corresp., Dr., Prof. Shubenko O., PhD., Sen. Res. Babak M.,
PhD., Sen. Res. Senetskyi O., Eng. Senetskaya D.
National Academy of Science of Ukraine A. N. Podgorny Institute of Problems of Mechanical Engineering - Kharkiv, Ukraine
E-mail: shuben@ipmach.kharkov.ua, aleksandr-seneckij@ukr.net, dasha.seneckaya@gmail.com

Abstract:
Methods for calculating the nonequilibrium phase transformations during the condensation of supercooled steam in the turbine flow path are developed. In the process of realization, the development of the classical Zel'dovich-Frenckel's theory for the case of nonstationary nucleation of a new phase with fast extensions of supercooled steam is considered. A numerical-analytical method for calculating condensation was designed and implemented in the form of a software package, which consistently takes into account the nonstationarity of the process. Numerical studies have shown high efficiency and accuracy of the method.
KEYWORDS: PHASE TRANSFORMATIONS, CONDENSATION, SUPERCOOLED STEAM, MOISTURE, TURBINE STAGE, MATHEMATICAL MODEL.

1. Introduction

Every year, the consumption of electricity increases, which in turn is compensated mainly by powerful thermal and nuclear power plants. One of the main problems arising in the operation of powerful power units is the work of the last stages of the low-pressure part in the wet steam area. Improvement of working processes in the two-phase flow, in which the formation, transformation and transfer of moisture has a significant negative effect on the characteristics of the stages, is one of the possibilities for further improving the economy and reliability of turbomachines [1, 2].

At the present time, at the modern period of development of turbine construction, the problems of the theory of the nucleation of moisture are analyzed and solved with taking into account the three-dimensional flow of steam in the turbine stages, the nonstationarity of the nucleation of a new phase and the energy exchange with the growth of condensed particles [3 – 5]. To solve the problems posed, it is necessary to obtain a system of equations that take into account nonstationarity, nonisothermal effects, and those that possess universality.

In this paper, we consider the problems of nonequilibrium homogeneous condensation in the expansion of supercooled steam in the turbine flow path. These studies are very relevant, since the nucleation of drops largely determines the nature of the further course of the working fluid. Its detailed investigation and description is necessary for the creation of appropriate gas-dynamic calculation schemes and for studying complex physical phenomena associated with the emergence of "condensation turbulence", the intensification of nonstationary processes, as well as the further transformation of water-droplets and their influence on working processes in the turbine flow path.

2. Fundamentals of the classical theory of the new phase nucleation

The new phase nucleation theory is closely related to the basic concepts of statistical physics and uses the fundamental results of Gibbs and Einstein. In the modern form it was developed by Zel'dovich [6], who received

(1) $$\frac{\partial f}{\partial t}+\frac{\partial j}{\partial g}=0, \quad j=DN\frac{\partial}{\partial g}\frac{f}{N}.$$

Expression (1) has the form of the Fokker-Planck's equation and represents the basic equation of the new phase nucleation kinetics, where g is the number of molecules in the nucleating droplet ("size"); $j(g,t)$ is the flow of nuclei in the size space; $D(g)$ is the diffusion coefficient; $f(g,t)$ and $N(g,t)$ are the kinetic and equilibrium distribution functions, respectively.

With time-independent external conditions, the system establishes a stationary distribution of droplets in size

$$f_{\mathrm{ST}}=\frac{1}{2}N\mathrm{erfc}(\tfrac{g-g_*}{\Delta}),$$

where $\mathrm{erfc}(z)=\frac{2}{\sqrt{\pi}}\int_z^\infty \mathrm{e}^{-x^2}dx$ is additional probability integral; $\Delta=\left\{-\frac{1}{2K_{\mathrm{B}}T}\cdot\frac{\partial^2 W}{\partial g^2}\Big|_*\right\}^{-1/2}$ is critical region width; K_{B} is the Boltzmann's constant.

The nucleation rate I_{ST}, that is, the number of stable nuclei formed in the system per unit time, is defined as the size-independent stationary flow

(2) $$j_{\mathrm{ST}}=I_{\mathrm{ST}}=\frac{D_*N_*}{\Delta\sqrt{\pi}}=\frac{1}{2\sqrt{\pi}}\cdot\frac{\partial\dot{g}}{\partial g}\Big|_* N_*\left\{-\frac{1}{2K_{\mathrm{B}}T}\cdot\frac{\partial^2 W}{\partial g^2}\Big|_*\right\}^{-1/2},$$

where $\dot{g}$ is the macroscopic rate of change in the size of the nucleus, which can be determined through the diffusion coefficient D in accordance with the well-known Einstein's relation

$$-\frac{D}{K_{\mathrm{B}}T}\frac{\partial W}{\partial g}=\dot{g}.$$

Concretizing the input quantities in the equation (2) as applied to the condensation of supercooled steam, Ya. I. Frenckel obtained an expression for the stationary nucleation rate (the Zel'dovich-Frenckel's formula) [7]

(3) $$I_{\mathrm{ST}}=\alpha_c W\left(\frac{2}{\pi}\right)^{1/2}\frac{p}{K_{\mathrm{B}}T}\cdot\frac{1}{\rho'}(\sigma m_{\mathrm{M}})^{1/2}N_1\exp\left(-\frac{4\pi\sigma}{3K_{\mathrm{B}}T}r_*^2\right),$$

where p is the steam pressure; ρ' is the liquid density; σ is the surface tension coefficient; m_{M} is the molecule mass; r_* is the radius of the critical nucleus; α_c is the condensation coefficient.

An analysis of the above theory shows that the assumption of stationarity of the nucleation process is violated in many practical cases, in particular, with the expansion of supercooled steam in the turbine flow path.

In this connection, it is advisable to consider the refinement of the kinetic aspects of nucleation associated with the situation noted above, when the steady-state approximation for the solution of equation (1) is not applicable. It should also be noted the need for detailed consideration of heat- and mass-transfer between a separate nucleus and steam.

3. Development of the classical theory as applied to working processes in the stages of wet-steam turbines

Let us further consider the development of the classical theory for the case of a nonstationary nucleation of a new phase with fast extensions of supercooled steam. The process of the nonstationary nucleation of a new phase is described by the Zel'dovich's equation (1). The nonstationarity of the problem is related to the time dependence of the external conditions and, consequently, the coefficients of equation (1).

To characterize the nonstationarity level, we introduce a certain quantity connecting the relaxation time to the stationary distribution τ_{rel} and the change rate of the nucleation barrier $\frac{\partial}{\partial t}(\frac{W_*}{K_\text{B}T})$, it is the nonstationarity coefficient *n*

$$n = -\tau_{\text{rel}} \frac{\partial}{\partial t}(\frac{W_*}{K_\text{B}T}). \quad (4)$$

To describe the initial period of condensation during the expansion of steam in the turbine flow path, it is necessary to solve the problem of determining the nucleation rate *I* under nonstationary external conditions, taking into account the release of heat in the growth of nuclei. The correctness of the obtained result is confirmed by the transition of the solution to the stationary solution if $n \to 0$. The solution of this problem for both isothermal (one-parameter) and nonisothermal nucleation was considered in [8, 9].

For us, the so-called "effect of the presence" of a new phase, which occurs only after a significant increase in the size of the nuclei formed, is of special interest. For such nuclei, the macroscopic growth equations and the change in the total number of molecules that have entered the new phase N' are valid, which are described as follows:

$$\frac{dN'}{dt} = \int_0^\infty I(t-t')g(t')\,dt', \quad (5)$$

where $I(t-t')$ is the nucleation rate, which in the general case should be determined from the Zel'dovich's equation (1); $g(t')$ is the number of molecules in the nucleating droplet that was formed at the time $(t-t')$ and is observed at time *t*.

The methods available in the literature for an approximate analytical study of equations of the type (5), together with the drop growth equation, in spite of their main advantage, which consists in obtaining closed analytic expressions for the total number of nuclei formed, have not found universal application. This is due to the use of a number of serious assumptions in their implementation, as mentioned above.

An alternative to the analytic description is the rejection of all sentences, except for the equations (1), (5) used in the derivation of the equations, and the subsequent numerical solution of these equations by a computer. This procedure was implemented by us to obtain an "exact" solution, which is then used to control the results obtained in the work and compare it with the results of other authors. However, in connection with the cumbersome numerical solution of the partial differential equation (1) in conjunction with the integral relation (5), the application of the method in problems characteristic of turbomachines, where condensation is only a part of very complex gas-dynamic processes (including multidimensional flow, its nonstationarity, turbulence and etc.) or in problems of synthesis of the optimal flow path is very difficult. In other words, in real calculation schemes, an increase in the "dimensionality" of the problem by adding an additional coordinate r_d is highly undesirable. The way out of this situation is to look at the evolution of several initial moments instead of the evolution of the distribution function

$$\Omega_\nu = \int_{r_*}^\infty r_d^\nu \cdot f(r_d)dr_d, \ \nu \geq 1.$$

Such an "intermediate", between analytical and numerical, the method has become quite widespread. In this method, while preserving the first two assumptions of the analytical approaches on the possibility of using the stationary expression for the nucleation rate and on the independence of the drop growth rate on their size, the integral equation (5) reduces to a system of differential equations for the moments of the distribution function

$$\begin{gathered}\dot{\Omega}_\nu = \nu \dot{r}_d \Omega_{\nu-1}, \ \nu = 1,2,3; \\ \dot{\Omega} = I_{\text{ST}}.\end{gathered} \quad (6)$$

The system (6) is actively used to study condensation in a variety of situations [8].

At the same time, the rejection of the assumption of stationarity of the nucleation process requires the refusal of the direct use of the system (6).

Thus, the problem of creating a sufficiently accurate and simple method for calculating the condensation process, taking into account the peculiarities of the nucleation of a new phase in the case of fast steam expansion in the turbine flow path and convenient for inclusion in gas-dynamic calculation schemes and in the synthesis of optimal constructions for wet-steam turbines, remains very relevant.

We note here that in carrying out numerical studies it is convenient to construct a general system of equations that makes it possible to perform calculations uniformly for arbitrary values of the coefficient λ, which characterizes the heat exchange between the steam and the nucleus. For the stage of moisture nucleation, the system of equations in the final form is represented as follows:

$$\begin{gathered}\dot{\Omega}_3 = 3\dot{r}_{d^\infty}\Omega_2, \ \dot{\Omega}_2 = 2\dot{r}_{d^\infty}\Omega_1 + J\delta^2, \\ \dot{\Omega}_1 = \dot{r}_{d^\infty}\Omega_0 - J\delta, \qquad \dot{\Omega}_0 = J,\end{gathered} \quad (7)$$

where

$$J = I_{\text{ST}} \frac{\mu}{\ln S} \Gamma(n+1) \cdot (6 \frac{W_*}{K_\text{B}T} \cdot e^{-\frac{25}{12}})^{-n};$$

$$\delta = \left\{\frac{\mu}{\exp(\mu - 1)} \cdot \ln\left[\frac{2}{n'} \cdot \frac{1-\exp(-\mu)}{\mu}\right] - 1\right\} r_*;$$

$$\dot{r}_{d^\infty} = \alpha_c \beta V_\text{M}' [1 - \exp(-\mu)], \ \beta = \frac{p}{\sqrt{2\pi m_\text{M} K_\text{B} T}},$$

$$n = \left(\frac{4\pi}{3}\right) r_*^4 \left(\frac{q}{K_\text{B}T}\right) \cdot \left(\frac{1}{V_\text{M}'}\right)^2 (\alpha_c \beta \mu)^{-1} \chi;$$

$$\mu = \frac{\lambda \ln S}{\lambda + \frac{K_\text{B}}{C_\text{M}} (\frac{q}{K_\text{B}T})^2};$$

$\dot{r}_{d^\infty}$ is the growth rate of a "large" droplet ($r_d \gg r_*$); β is the collision frequency with a unit surface; Γ is the gamma function; S is the degree of supersaturation; V_M' is the molecular volume; χ is the cooling rate; q and C_M' are the heat of a phase transformation and the heat capacity of a liquid per molecule; n' is the nonstationarity parameter, determined by the adiabatic expansion.

For the phase of recondensation, the analogous system of equations has the form

$$\begin{gathered}\dot{\Omega}_\nu = \nu\, \alpha_c \beta V_\text{M}' \Omega_{\nu-1} \left\{1 - \exp[\mu \cdot \frac{r_* \Omega_{\nu-2}}{\Omega_{\nu-1}} - 1)]\right\}, \ \nu = 2,3, \\ \dot{\Omega}_0 = -\frac{3}{4}\, \alpha_c \beta V_\text{M}' \mu \Omega_0 r_* R^{-2}, \\ \dot{\Omega}_1 = (\frac{8}{9}\Omega_0 \Omega_2)^{1/2}, \ R = (\frac{9}{8} \cdot \frac{\Omega_2}{\Omega_0})^{1/2}.\end{gathered} \quad (8)$$

4. Numerical studies

In the comparative analysis, the simplest case of isothermal nucleation under expansion with constant velocity Q is considered

$$V = V_0(1 + Qt),$$

so that the cooling rate equation has the form

$$\chi = (k-1)\cdot Q\frac{V_0}{V} - \frac{q}{t}\cdot\frac{1}{N_1 C_v + N' C_M'}\cdot\frac{dN'}{dt}.$$

Based on the two models presented in [9], a stationary description was made. In the first case, the system of equations for the moments of the distribution function is considered, and in the second case the initial size of the emerging nuclei is assumed to be equal to the critical one, and the growth is given by the following equation

$$\dot{r_d} = \alpha_c \beta V_M' \left\{1 - \exp[\ln S(\frac{r_*}{r_d} - 1)]\right\}.$$

In the integral equation, the nucleation rate I is replaced by the stationary value I_{ST}, this method was called the "stationary integral", in contrast to the "nonstationary integral" corresponding to the numerical experiment [9].

In Fig. 1 shows the results of the description of the initial period of the condensation process in the form of the time dependence of the quantity I_{ST} calculated in accordance with the process parameters obtained in calculations by various methods (the use of I_{ST} is related only to the clarity of comparison of various methods for describing the condensation process).

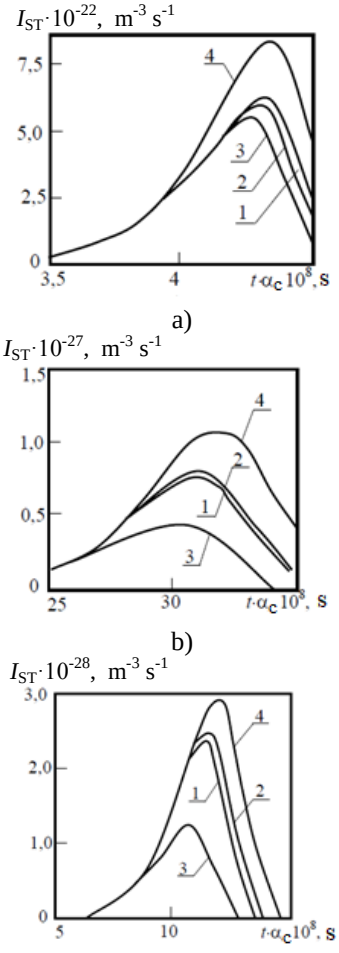


Fig. 1. Dependence of I_{ST} on time, determined on the basis of various methods:

a) $Q/\alpha_c = 1\cdot10^5$, s^{-1}; b) $Q/\alpha_c = 2{,}5\cdot10^6$, s^{-1};

c) $Q/\alpha_c = 1\cdot10^7$, s^{-1}.

In Fig. 1, curve 1 corresponds to a direct numerical solution of the system of equations, curve 2 corresponds to the proposed method, curve 3 corresponds to a stationary calculation using the method of moment equations and curve 4 corresponds to a "stationary integral" method.

Apparently, the presented method has the best agreement with the results of a numerical experiment.

In Fig. 2 shows the results of a description of the condensation process under expansion with a time-periodic velocity. The expansion rate is given by expression

$$Q = Q'(1 + A\sin\{\omega(t - t_0)\}),$$

where ω is the angular velocity of rotation.

In Fig. 2, "solid lines" correspond to the numerical experiment; "dots" correspond to the calculation by the proposed method.

Apparently, the proposed method well "follows" the changes in the flow parameters, which determines its prospects when using the calculations for the condensation process in conditions of unsteady flows.

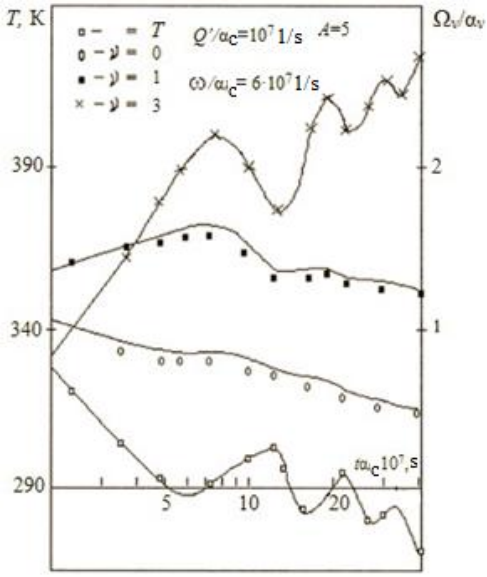


Fig. 2. Dependence of temperature and nondimensionless moments on time for the phase of recondensation at a periodic rate of expansion $Q = Q'(1 + A\sin\{\omega(t - t_0)\})$

5. Conclusion

1. An analytical solution is obtained for the nucleation rate of the nucleating droplets, which is valid practically at an arbitrary level of nonstationarity; the well-known Zel'dovich-Frenckel's expression follows from it for weak nonstationarity.

2. The developed numerical-analytical method for describing the condensation process, based on a consistent consideration of the nonstationarity of nucleation is practically accurate (within the framework of the basic assumptions of the classical theory of nucleation) both in the period of nucleation and in the period of recondensation.

3. The simplicity of the method makes it possible to significantly accelerate calculations in comparison with numerical experiment (the time of the account is greatly reduced). This circumstance determines broad possibilities for using it in problems of synthesis of the optimal flow path of a wet-steam turbine or in direct research problems, where

condensation is only a part of complex gas-dynamic processes.

6. Literature

1. Danmei, Xie. Numerical Simulation of Water Droplets Deposition on the Last-Stage Stationary Blade of Steam Turbine. – Energy and Power Eng, № 2, 2010, P. 248–253. (Danmei Xie, Yu Xinggang, Li Wangfan and etc.).

2. Ismailov, B. Mathematical Modeling, Dynamic and Mass-Transfer Calculation of Gas-Drop Mixture in the Mass-Transfer Apparatus Multistage Channels. – Appl. Math. Sci. Vol. 18, № 92, 2014, P. 4561–4570. (Ismailov B., K. Ismailov, A. Urmatova, T. Koyshieva).

3. Garmathy, G. Grundlagen einer Theorie der Naßdampfturbine. Zürich, 1962, 196 s. (Garmathy. G).

4. Кириллов, И. И. Основы теории влажнопаровых турбин. Л.: Машиностроение, 1968, 264 с. (Кириллов И. И., Р. М. Яблоник).

5. Дейч, М. Е. Газодинамика двухфазных сред. М.: Энергия, 1968, 424 с. (Дейч М. Е., Г. А. Филиппов).

6. Зельдович, Я. Б. К теории образования новой фазы. Кавитация. Журн. эксперимент. и теорет. физики, Т. 12, № 11–12, 1942, С. 525–534. (Зельдович Я. Б.).

7. Френкель, Я. И. Кинетическая теория жидкостей. Л.: Наука, 1975, 598 с. (Френкель Я. И.).

8. Шубенко, А. Л. Нестационарное неизотермическое зарождение жидкой среды при конденсации. Докл. АН УССР. Физ.-мат. и техн. науки, № 1, 1988, С. 69–72. (Шубенко А. Л., В. А. Шнейдман).

9. Шубенко, А. Л. Моделирование процесса зарождения новой фазы при расширении переохлажденного пара в проточной части турбомашин. Изв. АН СССР. Энергетика и транспорт, Т. 36, № 6, 1990, С. 90–97. (Шубенко А. Л.).